Numerical Investigation on Turbulent Non-premixed Methanol Flames Using Conditional Source-term Estimation

by

Seung Hi Lee

A thesis
presented to the University of Waterloo
in fulfillment of the
thesis requirement for the degree of
Master of Applied Science
in
Mechanical Engineering

Waterloo, Ontario, Canada, 2015

Author's Declaration

I hereby declare that I am the sole author of this thesis. This is a true copy of the thesis, including any required final revisions, as accepted by my examiners.

I understand that my thesis may be made electronically available to the public.

Abstract

Conditional Source-term Estimation (CSE) is a turbulent combustion model that uses conditional averages to close the chemical source term. Previous CSE studies have shown that the model is able to predict the flame characteristics successfully, however, these studies have only focused on simple hydrocarbon fuels mostly composed of methane. The objective of the present study is to evaluate the capabilities of CSE applied to turbulent non-premixed methanol flames, which has never been done previously.

The present study investigates two different types of methanol flames: piloted and bluff-body flames. For the piloted flame, the standard $k - \epsilon$ model is used for turbulence modelling, while the Shear Stress Transport (SST) $k - \omega$ model is used in the bluff-body case. Different values of empirical constants within the turbulence models are tested, and $C_{\epsilon 1} = 1.7$ for the piloted flame and $\gamma_2 = 0.66$ for the bluff-body flame provide the most comparable predictions of mixing field to the experimental measurements. Detailed chemistry mechanism, GRI MECH 2.11, is included in tabulated form using the Trajectory Generated Low-Dimensional Manifold (TGLDM) method.

The predictions including both the Favre averaged and conditional mass fractions of the reactive species and temperature are compared with available experimental data and previous numerical results. Overall, the predictions by CSE for both the conditional and unconditional quantities are in a good agreement with the experimental data except for H_2. Sources of discrepancies are identified such as the chemical kinetics and neglect of differential diffusion. Large Eddy Simulations may help to improve the velocity and mixing field predictions.

Acknowledgments

I would like to thank my supervisor, Professor Cècile Devaud, for providing assistance and guidance on my research throughout the duration of my MASc studies. My knowledge and understanding of CFD and combustion modelling have greatly increased thanks to her support. I would also like to thank my friends and colleagues in the Turbulent Combustion Modelling Group for their valuable support, especially Jeffrey Labahn, Daniele Dovizio, Dominic Man Ching Ma, and Duy Le. Financial support from Natural Sciences and Engineering Research Council of Canada (NSERC) and Ontario Graduate Scholarship (OGS) are gratefully acknowledged.

I would also like to thank Professor Fue-Sang Lien and Professor Zhongchao Tan for reviewing my thesis.

Table of Contents

List of Tables

List of Figures

Nomenclature

$\beta*, a_1, \beta_1, \sigma_{k1}, a_2, \gamma_2, \sigma_{k2}, \sigma_{\omega 2}$	SST $k-\omega$ model constants
χ	Scalar dissipation rate
χ_s	Scalar dissipation rate at the flame surface
δ_{ij}	Kronecker symbol
$\dot{\omega}_k$	Species chemical reaction rate
ϵ	Dissipation rate of k
η	Mixture fraction sample space variable
λ	Regularization parameter of Tikhonov regularization approach
μ	Molecular viscosity
μ_t	Turbulent viscosity
ν	Kinematic viscosity
ω	Specific dissipation rate
$\overline{f}$	Reynolds averaged value of the quantity f
ρ	Density
τ_{ij}	Viscous stress tensor
$\vec{\alpha}$	Solution of the Fredholm integral equation
$\vec{\alpha}_0$	*a priori* knowledge of the solution of the Fredholm integral equation

$\vec{b}$	Source vector representing the unconditional mass fraction in the CSE inversion problem
$\widetilde{f}$	Favre averaged value of the quantity f
ξ	Mixture fraction
ξ''^2	Mixture fraction variance
A	Kernel of the Fredholm integral equation
B	Body force
$C_\mu, \sigma_k, \sigma_\varepsilon, C_{\varepsilon 1}, C_{\varepsilon 2}$	Standard $k-\epsilon$ model constants
c_p	Constant pressure specific heat of mixture
D	Molecular diffusivity or Mixture fraction diffusivity
D_B	Diameter of bluff-body = 50 mm
D_t	Turbulent diffusivity
Da	Damköhler number
f''	Fluctuation of the quantity f
h	Total specific enthalpy of mixture
h_k	Total specific enthalpy of species k
j	Diffusive heat flux
k	Turbulent kinetic energy
Le	Lewis number
N	Number of species
p	Pressure
P_k	Production of turbulent kinetic energy
Q_r	radiation source term

r	Radial distance from centreline
Re	Reynolds number
S	Strain rate
Sc_{kt}	Turbulent Schmidt number for species k
T	Temperature
u_i	i-th component of velocity
u_{rms}	Velocity root mean square
x	Axial distance from inlet
x_i	i-th spatial coordinate
Y_k	Mass fraction of the species k
CDF	Cummulative distribution function
CFD	Computational fluid dynamics
CMC	Conditional moment closure
CSE	Conditional source-term estimation
DNS	Direct numerical simulation
LES	Large eddy simulation
LFM	Laminar flamelet model
LHS	Left hand side
MMC	Multiple mapping closure
PDF	Probability denstiy function
RANS	Reynolds averaged Navier Stokes Simulation
RHS	Right hand side
RMS	Root-mean-square

Chapter 1

Introduction

In this chapter, the motivation and objectives of the present study are provided, followed by an outline of the subsequent chapters.

1.1 Overview

With increasing energy prices and more stringent regulations to reduce environmental pollution, a range of energy sources are being investigated and developed worldwide, including wind, solar, and geothermal energy. However, these sources are not yet able to accommodate the world's ever increasing demands for energy. In Canada, rapid growth of energy usage is observed between 1990 and 2010: 38 % in transportation, 23 % in agriculture, 22 % in commercial, 19 % in industrial, and 6% in residential sectors [1]. Due to the large power demand, turbulent combustion processes are expected to remain the main energy production source. The major concerns with the combustion processes are the environmental pollution and greenhouse gas emissions, and research and development of new combustion technologies have been focused on reducing the emissions levels while improving the fuel economy.

In the research and design of combustion systems, numerical simulations using Computational Fluid Dynamics (CFD) are frequently used in conjunction with experimental investigations. One of the great advantages of using CFD is that the complex physical phenomena involved in the combustion process, which are difficult to observe in experimental studies, can be analyzed easily. Numerical combustion research, however, is very challenging since accurate modelling of the different physical processes involved in combustion is crucial. In turbulent combustion modelling, the complexity of the turbulence-chemistry

interactions, coupled with radiative and convective heat transfers and multi phases leads to many challenges. Further, the averaging of chemical reaction rates is not straightforward due to the non-linearity of chemical kinetic rates with chemical reactions that take place at the micro-flow scales. Furthermore, the tradeoff between the computational cost and accuracy of modelling is another criterion for model development. Current numerical combustion research is driven by these challenges.

Due to the environmental concerns with conventional petroleum based fuels, interest has risen in growth of using alternative fuels such as biofuels, hydrogen, and alcohols. For example, methanol is already used in many applications including automobiles. In addition to its primary source of production from coal gasification and natural gas, methanol can be synthesized from conversion of atmospheric carbon dioxide (CO_2) with hydrogen gas (H_2) [2]. The process is not quite feasible with current technology, but could be an option to reduce the atmospheric carbon dioxide level in the future. Methanol has a high octane rating and oxygen content, which is beneficial for gasoline engines. A number of studies have shown that blending methanol into gasoline improves the thermal efficiency of the engine and fuel economy while vehicle emission is reduced [2]. The development of combustion modelling techniques applicable for the viable alternative fuels including methanol can contribute to advance the state of the art.

1.2 Objectives

In an effort to reproduce the phenomena occurring during the combustion process, various numerical models have been proposed. Conditional Source-term Estimation (CSE) is a relatively new turbulent combustion model, which has shown great promise with accurate prediction of flame characteristics. For the last few years, CSE has been implemented, with good success, in non-premixed, premixed, and partially premixed flames. However, the model has only been focusing on methane (CH_4) and methane-based mixtures. The model is not proposed to only work for methane based flames; therefore, it is expected to provide good prediction of flames that burn fuels with complex chemical structures. Studying methanol (CH_3OH) flames is a good starting point in order to extend the application of CSE to fuels with more complex chemical structure than methane. Methanol contains extra oxygen atom than methane, and the reactions involved in methanol combustion are more complicated than that of methane. Moreover, the investigation of CSE in methanol flames is feasible since several experimental and numerical studies on methanol flames are available to evaluate the accuracy of the modelling. Quantitative investigations on the methanol combustion will step CSE forward to further extended application of the model.

The objectives of the present study are:

• The simulation of two turbulent methanol non-premixed flames using CSE. To the author's best knowledge, there has been no attempt to reproduce any methanol flames using the CSE approach.

• The assessment of performance of CSE by comparing the results to available experimental data and previously simulated results. This is done by examining the reactive species mass fractions and temperature of the methanol flame.

• The suggestion of future investigations for improving the CSE method.

1.3 Outline

Chapter 2 provides the general background of turbulent combustion modelling. The fundamental concepts are covered first to provide sufficient knowledge for the reader to interpret the contents of the following chapters. Starting from the governing equations of fluid flows, statistical description of turbulence, transport equations averaging techniques, turbulence modelling, and common tools for turbulent non-premixed combustion are provided. Chapter 2 concludes with a brief presentation for various methods in turbulent combustion modelling.

In Chapter 3, the detail of the turbulent combustion modelling approach applied in this study, CSE, is discussed. The principle of CSE for non-premixed combustion is explained first. Followed by the basic principle, the information regarding the techniques used in CSE is explained. The implementation of the current CSE approach integrated with CFD module is illustrated to help readers understand how the model works in computational fluid dynamics. The last section of the chapter provides information on previous studies on CSE, which addresses the needs of CSE to be applied for fuels with more complex chemical structure than methane.

Chapter 4 introduces the previous experimental and related numerical studies on turbulent non-premixed methanol flames. There are two different methanol flames investigated in the present study: piloted flame and bluff-body flame. The experimental conditions, available results from the experiments, and related previous numerical results are analyzed for each flame.

The CSE results for the piloted flame are presented in Chapter 5. The chapter begins with the summary of the corresponding experimental conditions illustrated in Chapter 4.

The details of the simulations performed in the current study on the piloted flame are investigated including boundary conditions, mesh, and variation of model constants. Finally, the CSE predictions for species concentrations and temperatures are compared with the experimental data and the previously simulated results.

In Chapter 6, the numerical results using CSE on the bluff-body flame are covered. The structure of the chapter is similar to Chapter 5. Starting from the explanation of experimental conditions, the current computational set-ups are introduced. The CSE results are then compared with the available experimental data and results from a previous numerical investigation.

Conclusions based on the current study are covered in Chapter 7. A summary of all work performed and the findings of this study is presented. Finally, some recommendations regarding the future work based on the current study are presented.

Chapter 2

Background

In this chapter, some background information on turbulent combustion modelling is provided. Starting from the governing equations for fundamental fluid and thermodynamics, a review of statistical treatment of turbulence, various turbulent flow field modelling, and turbulent combustion modelling techniques are introduced.

2.1 Governing Equations of Fluid Flow

The fluid flow is governed by three main equations: conservation of mass, momentum, and energy (or enthalpy). The intensive and extensive properties can be obtained by solving these equations.

2.1.1 Conservation of Mass

The conservation of mass is more commonly known as continuity equation, and is given by

$$\frac{\partial \rho}{\partial t} + \frac{\partial}{\partial x_i}(\rho u_i) = 0, \tag{2.1}$$

where ρ is density, t time, u velocity, and i the index for direction in Cartesian space. The first term on the Left Hand Side (LHS) is the rate of change of mass within the control volume, and the second term is the convective mass transport. The term on the Right Hand Side (RHS) indicates that there is no source or sink for mass.

2.1.2 Conservation of Linear Momentum

The surface and pressure forces acting on the control surface related to density and velocity in a control volume are governed by the conservation of linear momentum equation such as

$$\frac{\partial}{\partial t}(\rho u_i) + \frac{\partial}{\partial x_i}(\rho u_i u_j) = -\frac{\partial p}{\partial x_j} + \frac{\partial \tau_{ij}}{\partial x_i} + B, \tag{2.2}$$

where the first term on the LHS represents the local rate of change in momentum, and the second term is the convective transfer in momentum. The first term on the RHS is the pressure gradient acting on the fluid particle, the second term is the force due to symmetric shear stress tensor, and the last term represents any body forces acting on the surface including gravity and magnetic forces. The stress tensor, τ_{ij}, is given by

$$\tau_{ij} = \mu(\frac{\partial u_i}{\partial x_j} + \frac{\partial u_j}{\partial x_i}) - \mu\frac{2}{3}\frac{\partial u_k}{\partial x_k}\delta_{ij}, \tag{2.3}$$

where μ is the dynamic viscosity and δ_{ij} is the Kronecker delta which is equal to 1 when $i = j$, and 0 when $i \neq j$.

2.1.3 Conservation of Enthalpy

The fluid enthalpy can be divided into two main components: the sensible enthalpy and the enthalpy of formation. Sensible enthalpy is the energy required to change temperature from a reference state to another state. This is often calculated by integrating the specific heat capacity of species k, c_{pk}, over the given change in temperature. Meanwhile, the enthalpy of formation, $h_{k,ref}$, is the energy contained within the chemical bonds of species. The total enthalpy can be obtained by adding the sensible enthalpy and the enthalpy of formation together, such that

$$h_k = \int_{T_o}^{T} c_{pk} dT + \Delta h^o_{f,k}, \tag{2.4}$$

where h_k is the total enthalpy of species k, and the first term on the RHS represents the sensible enthalpy and the second term represents the enthalpy of formation at the reference temperature, T_o. For a flow composed of more than one species, the specific heat capacity of mixture can be calculated using a mass-weighted sum

$$c_p = \sum_{N}^{k=1} Y_k c_{pk}, \tag{2.5}$$

where Y_k is the mass fraction of species k and N the total number of species in the mixture. The total enthalpy of mixture, h, can be obtained by solving

$$h = \sum_{N}^{k=1} Y_k h_k = \Big(\int_{T_o}^{T} c_{pk} dT + \sum_{k=1}^{N} \Delta h^o_{f,k} \Big) Y_k. \tag{2.6}$$

Finally, the transport equation for the total enthalpy within the system can be written as

$$\begin{aligned} \frac{\partial}{\partial t}(\rho h) + \frac{\partial}{\partial x_i}(\rho u_i h) = \frac{\partial p}{\partial t} + \frac{\partial}{\partial x_i}(u_i p) + \frac{\partial}{\partial x_i}(u_i \tau_{ij}) \\ + \dot{Q}_{rad} + u_i B - \frac{\partial q_i}{\partial x_i}. \end{aligned} \tag{2.7}$$

The first term on the LHS in Eq. 2.7 represents the rate of change in enthalpy, and the second term corresponds to the convective enthalpy transfer. On the RHS, the first term is the change of pressure over time, the second term is the work done by pressure, and the third term represents the work done by shear stresses. The fourth term on the RHS is the heat source term due to radiation, and the fifth term is the work done by any body forces. The last term on the RHS is the diffusive term, where q_i is the heat flux. The heat flux can be further expressed as

$$q_i = -\lambda \frac{\partial T}{\partial x_i} + \sum_{k=1}^{N} h_k j_k, \tag{2.8}$$

where, λ is the thermal conductivity and j_k is the diffusive heat flux. Applying Fick's first law, the diffusive heat flux can be written as

$$j_k = -\rho D_k \frac{\partial Y_k}{\partial x_i}. \tag{2.9}$$

In Eq. 2.9, D_k represents the diffusivity of species k.

2.1.4 Transport of Species

In addition to the fundamental governing equations in Sections 2.1.1, 2.1.2, and 2.1.3, it is very important to address the transport equation of species for the use of scalars. In a reacting flow, the governing equation of species k is given by

$$\frac{\partial}{\partial t}(\rho Y_k) + \frac{\partial}{\partial x_i}(\rho u_i Y_k) = -\frac{\partial (j_{i,k})}{\partial x_i} + \dot{\omega_k}, \tag{2.10}$$

where $\dot{\omega}_k$ is the rate of production or destruction of species k due to chemical reactions. The sum of all the species mass fractions must sum to unity,

$$\sum_{k=1}^{N} Y_k = 1. \tag{2.11}$$

2.2 Statistical Description of Turbulence

The fluid flow at any Reynolds number, Re, can be described by using the instantaneous governing equations illustrated in Section 2.1. However, in a turbulent flow, the fluctuation about its mean value of quantity is random or chaotic, and the state of the system can be significantly changed even with small pertubations in the system. In general, turbulence is treated as a statistical random dynamic process, where a set of values from the probability function is used to describe the randomly fluctuating flow quantities. This section provides a brief overview of concepts in statistics.

2.2.1 Probability Density Functions

In turbulent combustion modelling, it is a common approach to view quantities including velocity as random variables which can be quantified as a probabilities in the range of sample space. The likelihood or probability of a stochastic variable ϕ in the sample space of Φ can be characterized by the use of a Probability Density Function (PDF) or Cumulative Distribution Function (CDF) [3, 4]. The statistical method does not provide the exact value of the variables, but allows the value to be stated with a level of confidence. The CDF of the random variable ϕ is the probability of the event in which ϕ takes a value less than or equal to a particular value in the sample space, such that

$$F(\Phi) = prob(\phi < \Phi), \tag{2.12}$$

where F denotes the CDF of the event. In Eq. 2.12, the resultant probabilities will be 0 in the case where Φ is sufficiently small so that $\phi < \Phi$ is never true. On the other hand, if Φ is sufficiently large so that $\phi < \Phi$ is always true, the resultant probability, $F(\Phi)$, is unity. The PDF is an alternative way of representing the probability of the event, which is defined as the derivative of the CDF

$$P(\Phi) = \frac{dF(\Phi)}{d\Phi}. \tag{2.13}$$

Figure 2.1 illustrates an example of the CDF and PDF of a Gaussian distribution.

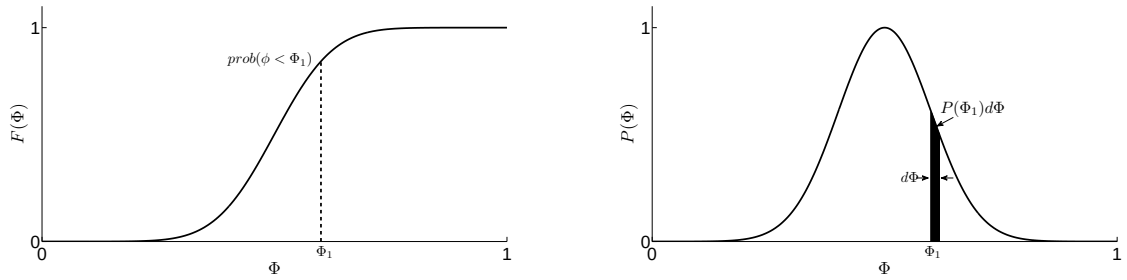

(a) CDF (b) PDF

Figure 2.1: CDF and PDF of Gaussian distribution

The probability of ϕ being within some range of $d\Phi$ is given by the product of $P(\Phi)$ and $d\Phi$;

$$prob(\Phi \leq \phi < \Phi + d\Phi) = P(\Phi)d\Phi. \tag{2.14}$$

An important property of PDF is that the sum of the probability over the entire space must be equal to 1, such that

$$\int_{-\infty}^{\infty} P(\Phi)d\Phi = 1. \tag{2.15}$$

The mean or expected value of the variable ϕ, $\langle\phi\rangle$, can be defined as

$$\langle\phi\rangle = \int_{-\infty}^{\infty} \Phi P(\Phi)d\Phi. \tag{2.16}$$

Similar to Eq. 2.16, the mean of any function of ϕ can be obtained by solving

$$\langle f(\phi)\rangle = \int_{-\infty}^{\infty} f(\Phi)P(\Phi)d\Phi. \tag{2.17}$$

The dependence of a variable on another single random variable can be extended to multivariate variables. The resultant PDF is well known as a joint PDF

$$P(\Phi_1, \Phi_2) = P(\Phi_1|\phi_2 = \Phi_2)P(\Phi_2), \tag{2.18}$$

where $P(\Phi_1|\phi_2 = \Phi_2)$ is the probability density function of variable ϕ_1 having a value of Φ_1 at the condition where $\phi_2 = \Phi_2$ is satisfied.

2.2.2 Conditional Probability Density Functions and Conditional Averages

A conditional probability is the probability of an event Φ_1 of ϕ_1 takes place, given that another event of Φ_2 of the random variable, ϕ_2, occurs, such that

$$P(\Phi_1|\Phi_2) = \frac{P(\Phi_1, \Phi_2)}{P(\Phi_2)}. \tag{2.19}$$

The conditional expectation, $\langle \phi_1 | \phi_2 = \Phi_2 \rangle$, is the average of Φ_1 over the event of occurrence Φ_2, which can by obtained by solving

$$\langle \phi_1 | \phi_2 = \Phi_2 \rangle = \int_{-\infty}^{\infty} \Phi_1 P(\Phi_1 | \phi_2 = \Phi_2) d\Phi_1. \tag{2.20}$$

Finally, the unconditional mean of ϕ_1 at all realizations of ϕ_2, $\langle \phi_1 \rangle$, can be obtained by solving

$$\langle \phi_1 \rangle = \int_{-\infty}^{\infty} \langle \phi_1 | \phi_2 = \Phi_2 \rangle \, P(\Phi_2) d\Phi_2. \tag{2.21}$$

2.3 Averaging Transport Equations

Since there is no random fluctuation about the mean scalar, the statistical description of laminar flow is simple. For a transitional flow, small instabilities within the flow start to have impact on the flow structures. The instability within the flow plays a huge role in fully turbulent flow, which makes the statistical description of turbulent flow more complicated. Turbulent flows contain irregular, random motions over a range of length scales. In a turbulent flow, the instantaneous quantities can be decomposed into mean and fluctuating components. In this section, two main averaging techniques are described: Reynolds averaging and Favre averaging.

2.3.1 Reynolds Averarging

In Reynolds averaging, a stochastic quantity, ϕ, is decomposed into a time average and fluctuation about the average

$$\phi(x_i, t) = \bar{\phi}(x_i, t) + \phi'(x_i, t), \tag{2.22}$$

where $\phi(x_i, t)$ is the instantaneous value, $\overline{\phi}(x_i, t)$ is the average value, and $\phi'(x_i, t)$ is the fluctuation about the average value. The Reynolds decomposition is illustrated in Fig 2.2.

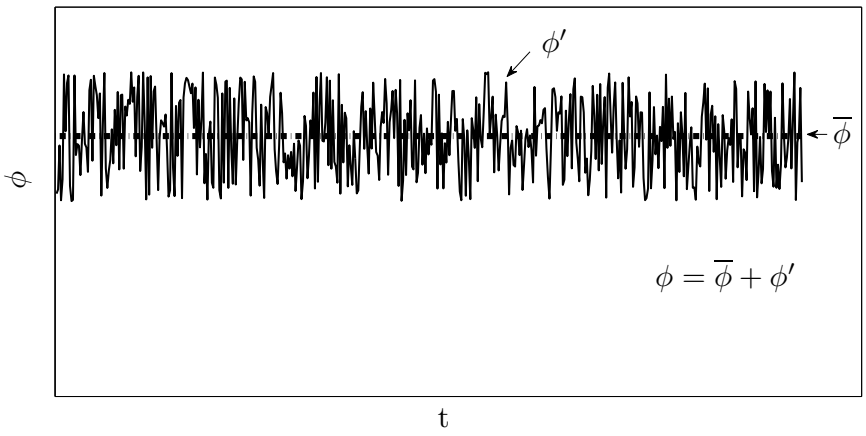

Figure 2.2: Reynolds decomposition

Applying Reynolds averaging, the conservation of mass (Eq. 2.1) and momentum (Eq. 2.2) become

Conservation of Mass:

$$\frac{\partial \overline{\rho}}{\partial t} + \frac{\partial}{\partial x_i}(\overline{\rho u_i}) = 0, \tag{2.23}$$

Conservation of Momentum:

$$\frac{\partial(\overline{\rho u_i})}{\partial t} + \frac{\partial}{\partial x_i}(\overline{\rho u_i u_j}) + \frac{\partial \overline{\rho} \overline{u_i' u_j'}}{\partial x_j} = -\frac{\partial \overline{p}}{\partial x_j} + \frac{\partial \overline{\tau_{ij}}}{\partial x_i} + \overline{B}. \tag{2.24}$$

Equations 2.23 and 2.24 are known as Reynolds Averaged Navier-Stokes (RANS) equations. In Eq. 2.24, the last term on the LHS, $\frac{\partial \overline{\rho} \overline{u_i' u_j'}}{\partial x_j}$, denotes the Reynolds stresses, which are related to the convective momentum transfer from turbulent eddies.

2.3.2 Favre Averaging

In turbulent reacting flows, the density fluctuation is significant due to large change in temperature. For these flows, the density weighted averaging, or so called Favre averaging

is preferred [5]. The Favre averaging is given by

$$\widetilde{\phi} = \frac{\overline{\rho\phi}(x_i, t)}{\overline{\rho}}. \tag{2.25}$$

Using the Favre averaging technique, the instantaneous value of the quantity ϕ can be decomposed into

$$\phi(x_i, t) = \widetilde{\phi}(x_i, t) + \phi''(x_i, t), \tag{2.26}$$

where $\phi''(x_i, t)$ represents the fluctuation about the Favre averaged quantity. The Favre averaged form of the transport equations can be written as

Conservation of Mass:

$$\frac{\partial \overline{\rho}}{\partial t} + \frac{\partial}{\partial x_i}(\overline{\rho}\widetilde{u_i}) = 0, \tag{2.27}$$

Conservation of Momentum:

$$\frac{\partial(\overline{\rho}\widetilde{u_i})}{\partial t} + \frac{\partial}{\partial x_i}(\overline{\rho}\widetilde{u_i}\widetilde{u_j}) + \frac{\partial \overline{\rho}\widetilde{u_i''u_j''}}{\partial x_j} = -\frac{\partial \overline{p}}{\partial x_j} + \frac{\partial \overline{\tau_{ij}}}{\partial x_i} + \widetilde{B}, \tag{2.28}$$

Transport of Species

$$\frac{\partial}{\partial t}(\overline{\rho}\widetilde{Y_k}) + \frac{\partial}{\partial x_i}(\overline{\rho}\widetilde{u_i}\widetilde{Y_k}) = -\frac{\partial}{\partial x_i}(\overline{\rho}\widetilde{u_k''Y_k''}) + \frac{\partial}{\partial x_i}(\rho D\frac{\partial \widetilde{Y_k}}{\partial x_i}) + \overline{\dot{\omega}_k}, \tag{2.29}$$

Conservation of Enthalpy:

$$\frac{\partial}{\partial t}(\overline{\rho}\widetilde{h}) + \frac{\partial}{\partial x_i}(\overline{\rho}\widetilde{u_i}\widetilde{h}) = \frac{\partial \overline{p}}{\partial t} + \frac{\partial}{\partial x_i}\left(\overline{\lambda}\frac{\partial \widetilde{T}}{\partial x_i} - \overline{\rho}\sum_{k=1}^{N}\widetilde{h}_k D_k \frac{\partial \widetilde{Y_k}}{\partial x_i} - \overline{\rho}\widetilde{u_i''h''}\right) + \overline{\tau_{ij}\frac{\partial u_i}{\partial x_j}} + \widetilde{\dot{Q}}_{rad} + \overline{\rho}\widetilde{B}. \tag{2.30}$$

The Reynolds stress term in Eq. 2.28, $(\overline{\rho}\widetilde{u_i''u_j''})$, and Reynolds flux terms $(\overline{\rho}\widetilde{u_i''Y_k''})$ and $(\overline{\rho}\widetilde{u_i''h''})$ in 2.29 and 2.30, respectively, are unclosed terms. The closure for these terms can

be achieved by modelling. A common way of closing the Reynolds fluxes is using a gradient diffusion assumption;

$$\overline{\rho}\widetilde{u_i^{"}Y_k^{"}} = -\frac{\mu_t}{Sc_{kt}}\frac{\partial \widetilde{Y}_k}{\partial x_i}, \tag{2.31}$$

$$\overline{\rho}\widetilde{u_i^{"}h^{"}} = -\frac{\mu_t}{Pr}\frac{\partial \widetilde{h}}{\partial x_i}, \tag{2.32}$$

where μ_t is the turbulent viscosity which can be obtained from the turbulence model, Pr is the Prandtl number, and Sc_{kt} is the turbulent Schmidt number for species k. In case of high Reynolds number, the $\frac{\partial}{\partial x_i}(\rho D\frac{\partial \widetilde{Y_k}}{\partial x_i})$ term in 2.29 can be neglected. The same argument may be applied to Eq. 2.30, such that the term $\overline{\lambda}\frac{\partial \widetilde{T}}{\partial x_i}$ can be neglected since the magnitude of the term is much smaller than $\frac{\mu_t}{Pr}\frac{\partial \widetilde{h}}{\partial x_i}$ at high Reynolds number.

2.4 Turbulence Modelling

In order to predict the effects due to turbulence, substantial amount of research effort has been spent. There are mainly three methods in simulating turbulent flow field: Direct Numerical Simulation (DNS), Reynolds Average Navier Stokes (RANS) simulation, and Large Eddy Simulation (LES). The following section gives an overview of each method.

2.4.1 Direct Numerical Simulation

In Direct Numerical Simulation (DNS), the state of the system is completely resolved instead of being determined based on a probability function. The unsteady Navier-Stokes equations are solved on spatial grids which are adequately fine enough so that small length scales are resolved. In addition, time steps in DNS are sufficiently small to accommodate the fastest fluctuation. As a result, the method requires huge computational resources. Due to its high computational expense, the use of DNS in industrial application is not feasible. A limited number of turbulent flames has been analyzed using DNS [6, 7, 8, 9, 10].

2.4.2 Reynolds Averaged Navier Stokes Simulations

Reynolds Averaged Navier Stokes (RANS) simulations involve solving the averaged Navier-Stokes equations presented in Section 2.3. RANS mainly focuses on the mean flow as well

as the effects of turbulence on mean properties, closing the Reynolds stress term in the averaged equations by modelling. For most of the RANS models, the turbulent viscosity hypothesis proposed by Boussinesq is used, where the Reynolds stresses are assumed to be proportional to the mean rates of deformation of fluid elements. Applying the hypothesis, the Reynolds stresses are determined by the mean velocity gradients. In Favre averaged form, the Reynolds stress can be expressed as

$$\overline{\rho}\widetilde{u_i"u_j"} = -\mu_t(\frac{\partial\widetilde{u}_i}{\partial x_j} + \frac{\partial\widetilde{u}_j}{\partial x_i}) + \frac{2}{3}\overline{\rho}\widetilde{k}\delta_{ij}, \tag{2.33}$$

where k is the turbulent kinetic energy. The assumption is poor in complex flows, however, reasonable predictions can be obtained for simple shear flows using the turbulent viscosity hypothesis.

Mixing Length Model

Prandtl suggested the mixing length model in 1925, which does not require the solution of any additional transport equations [11]. The mixing length model assumes that the kinematic turbulent viscosity, $\nu_t = \frac{\mu_t}{\rho}$, is the product of a turbulent velocity scale, v_t, and an assumed mixing length scale, l_t, such that

$$\nu_t = Cv_t l_t. \tag{2.34}$$

In Eq. 2.34, C is a dimensionless constant of proportionality. In simple two-dimensional turbulent flows, the only significant Reynolds stress is $\overline{\rho}\widetilde{u_i"u_j"}$ and the only significant mean velocity gradient is $\frac{\partial\widetilde{u}_i}{\partial x_j}$. Therefore, the velocity scale can be described as

$$v_t = cl_t\left|\frac{\partial\widetilde{u}_i}{\partial x_j}\right|, \tag{2.35}$$

where c is a dimensionless constant. The absolute value on the RHS is taken to make sure that the velocity scale is always positive irrespective to the sign of the velocity gradient. Combining Eq. 2.34 and Eq. 2.35, the kinematic turbulent viscosity becomes

$$\nu_t = l_t^2\left|\frac{\partial\widetilde{u}_i}{\partial x_j}\right|. \tag{2.36}$$

Finally, using Eq. 2.36, the Reynolds stress term can be expressed as

$$\overline{\rho}\widetilde{u_i"u_j"} = -\overline{\rho}l_t^2\left|\frac{\partial\widetilde{u}_i}{\partial x_j}\right|\frac{\partial\widetilde{u}_i}{\partial x_j}. \tag{2.37}$$

The mixing length model is easy to implement and inexpensive in terms of computational cost. However, the accuracy of the modelling depends on the selection of length scale [3, 11].

Standard k-ϵ Model

The standard $k-\epsilon$ model is one of the most well known RANS models, which focuses on the mechanisms that affect the turbulent kinetic energy [3, 11, 12]. In the model, the turbulent kinetic energy, k, is determined by (in Favre averaged form)

$$\widetilde{k} = \frac{1}{2}\sum_{k=1}^{3} \widetilde{u_i" u_j"}. \tag{2.38}$$

In addition to the turbulent kinetic energy, the $k-\epsilon$ model also focuses on the rate of viscous dissipation, ϵ [13]. In the model, k and ϵ are used to define velocity scale, v, and length scale, l, as follows

$$v = k^{\frac{1}{2}} \qquad l = \frac{k^{\frac{3}{2}}}{\epsilon}. \tag{2.39}$$

Using Eq. 2.34 and Eq. 2.39, the turbulent eddy viscosity is expressed as

$$\mu_t = \rho\nu_t = \rho C v l = \overline{\rho} C_\mu \frac{k^2}{\epsilon}, \tag{2.40}$$

where C_μ is a dimensionless constant. The transport equation for k and ϵ are

$$\frac{\partial(\overline{\rho}\widetilde{k})}{\partial t} + \frac{\partial(\overline{\rho}\widetilde{u_i}\widetilde{k})}{\partial x_i} = \frac{\partial}{\partial x_i}\left[(\mu + \frac{\mu_t}{\sigma_k})\frac{\partial \widetilde{k}}{\partial x_i}\right] + P_k - \overline{\rho}\widetilde{\epsilon}, \tag{2.41}$$

and

$$\frac{\partial(\overline{\rho}\widetilde{\epsilon})}{\partial t} + \frac{\partial(\overline{\rho}\widetilde{u_i}\widetilde{\epsilon})}{\partial x_i} = \frac{\partial}{\partial x_i}\left[(\mu + \frac{\mu_t}{\sigma_k})\frac{\partial \widetilde{\epsilon}}{\partial x_i}\right] + C_{\epsilon 1}\frac{\widetilde{\epsilon}}{k}P_k - C_{\epsilon 2}\overline{\rho}\frac{\widetilde{\epsilon}^2}{k}, \tag{2.42}$$

where P_k is the production term for turbulent kinetic energy,

$$P_k = -\overline{\rho}\widetilde{u_i" u_j"}\frac{\partial \widetilde{u_i}}{\partial x_j}. \tag{2.43}$$

The standard values for the constants in Eqs. 2.41 and 2.42 are

$$C_\mu = 0.09, \quad C_{\epsilon 1} = 1.44, \quad C_{\epsilon 2} = 1.92, \quad \sigma_k = 1.0, \quad \text{and} \quad \sigma_\epsilon = 1.3. \tag{2.44}$$

The standard $k-\epsilon$ model is well known for its over prediction of spread rate around the main jet [11]. The overprediction of the spread rate can be resolved by tuning either one of the empirical constants, $C_{\epsilon 1}$ and $C_{\epsilon 2}$.

Wilcox k-ω model

Another commonly used RANS model is Wilcox $k-\omega$ [14] proposed by Wilcox in 1988. The basic idea of the model is similar to the $k-\epsilon$ model, but it introduces the turbulence frequency $\omega = \frac{\epsilon}{k}$. In the model, the transport equation for ω is solved instead of ϵ. The resulting transport equations for k and ω are

$$\frac{\partial(\overline{\rho}\widetilde{k})}{\partial t} + \frac{\partial(\overline{\rho}\widetilde{u_i}\widetilde{k})}{\partial x_i} = \frac{\partial}{\partial x_i}\left[(\mu + \mu_t\sigma_{k_1})\frac{\partial \widetilde{k}}{\partial x_i}\right] + \overline{\rho}P_k - \beta^*\overline{\rho}\widetilde{\omega}\widetilde{k}, \tag{2.45}$$

$$\frac{\partial(\overline{\rho}\widetilde{\omega})}{\partial t} + \frac{\partial(\overline{\rho}\widetilde{u_i}\widetilde{\omega})}{\partial x_i} = \frac{\partial}{\partial x_i}\left[(\mu + \mu_t\sigma_{\omega_1})\frac{\partial \widetilde{\omega}}{\partial x_i}\right] + \overline{\rho}\gamma_1 S^2 - \beta_1\overline{\rho}\widetilde{\omega}^2, \tag{2.46}$$

where S is the invariant measure of the strain rate. In Eqs. 2.45 and 2.46, the default values for model constants are

$$\begin{gathered}\beta^* = 0.09, \quad \beta_1 = 3/40, \quad \sigma_k = 0.85, \quad \sigma_{\omega 1} = 0.5, \\ \gamma_1 = \beta_1/\beta^* - \sigma_{\omega 1}\kappa^2/\sqrt{\beta^*}, \quad \text{and} \quad \kappa = 0.41.\end{gathered} \tag{2.47}$$

SST k-ω Model

The Shear Stress Transport (SST) $k-\omega$ approach [15] combines Wilcox $k-\omega$ formulation in the inner parts of the boundary layer and $k-\epsilon$ in the free stream. The governing equations for Wilcox $k-\omega$ model are combined with the governing equations for the standard $k-\epsilon$ model. The governing equations for the $k-\epsilon$ model (Eqs. 2.41 and 2.42) can be transformed into $k-\omega$ form, such that

$$\frac{\partial(\overline{\rho}\widetilde{k})}{\partial t} + \frac{\partial(\overline{\rho}\widetilde{u_i}\widetilde{k})}{\partial x_i} = \frac{\partial}{\partial x_i}\left[(\mu + \mu_t\sigma_{k_2})\frac{\partial \widetilde{k}}{\partial x_i}\right] + P_k - \beta^*\overline{\rho}\widetilde{\omega}\widetilde{k}, \tag{2.48}$$

$$\frac{\partial(\overline{\rho}\widetilde{\omega})}{\partial t} + \frac{\partial(\overline{\rho}\widetilde{u_i}\widetilde{\omega})}{\partial x_i} = \frac{\partial}{\partial x_i}\left[(\mu + \mu_t\sigma_{\omega_2})\frac{\partial \widetilde{\omega}}{\partial x_i}\right] + \overline{\rho}\gamma_2 S^2 - \beta_2\overline{\rho}\widetilde{\omega}^2 + 2\frac{\overline{\rho}\sigma_{\omega 2}}{\omega}\frac{\partial \widetilde{k}}{\partial x_i}\frac{\partial \widetilde{\omega}}{\partial x_i}, \tag{2.49}$$

where

$$\begin{gathered}\beta^* = 0.09, \quad \beta_2 = 0.0828, \quad \sigma_{k2} = 1.0, \quad \sigma_{\omega 2} = 0.856, \\ \gamma_1 = \beta_2/\beta^* - \sigma_{\omega 2}\kappa^2/\sqrt{\beta^*}, \quad \text{and} \quad \kappa = 0.41.\end{gathered} \tag{2.50}$$

Combining Eqs. 2.45, 2.46, 2.48, and 2.49, the governing equations for SST $k-\omega$ model can be obtained

$$\frac{\partial(\overline{\rho}\widetilde{k})}{\partial t}+\frac{\partial(\overline{\rho}\widetilde{u_i}\widetilde{k})}{\partial x_i}=\frac{\partial}{\partial x_i}\left[(\mu+\mu_t\sigma_k)\frac{\partial\widetilde{k}}{\partial x_i}\right]+P_k-\beta^*\overline{\rho}\widetilde{\omega}\widetilde{k}, \tag{2.51}$$

$$\frac{\partial(\overline{\rho}\widetilde{\omega})}{\partial t}+\frac{\partial(\overline{\rho}\widetilde{u_i}\widetilde{\omega})}{\partial x_i}=\frac{\partial}{\partial x_i}\left[(\mu+\mu_t\sigma_\omega)\frac{\partial\widetilde{\omega}}{\partial x_i}\right]+\overline{\rho}\gamma S^2-\beta\overline{\rho}\widetilde{\omega}^2+2(1-F_1)\frac{\overline{\rho}\sigma_{\omega 2}}{\omega}\frac{\partial\widetilde{k}}{\partial x_i}\frac{\partial\widetilde{\omega}}{\partial x_i}, \tag{2.52}$$

where, F_1 is the primary blending function

$$F_1=\tanh\left\{\left\{\min\left[\max\left(\frac{\sqrt{\widetilde{k}}}{\beta^*\widetilde{\omega}y},\frac{500\nu}{y^2\widetilde{\omega}}\right),\frac{4\overline{\rho}\sigma_{\omega 2}\widetilde{k}}{CD_{k\omega}y^2}\right]^4\right\}\right\}, \tag{2.53}$$

with

$$CD_{k\omega}=\max\left(2\overline{\rho}\sigma_{\omega 2}\frac{1}{\omega}\frac{\partial\widetilde{k}}{\partial x_i}\frac{\partial\widetilde{\omega}}{\partial x_i},10^{-10}\right), \tag{2.54}$$

and the production term,

$$P_k=min(\mu_t\frac{\partial\widetilde{u_i}}{\partial x_j}(\frac{\partial\widetilde{u_i}}{\partial x_j}+\frac{\partial\widetilde{u_j}}{\partial x_i}),10\beta^*\widetilde{k}\widetilde{\omega}). \tag{2.55}$$

The turbulent eddy viscosity, μ_t is calculated using

$$\mu_t=\frac{\overline{\rho}a_1\widetilde{k}}{\max(a_1\widetilde{\omega},SF_2)}, \tag{2.56}$$

where $a_1=0.31$ and F_2 is the secondary blending function, which is expressed as

$$F_2=\tanh\left\{\left[\max\left(\frac{2\sqrt{\widetilde{k}}}{\beta^*\widetilde{\omega}y},\frac{500\nu}{y^2\widetilde{\omega}}\right)\right]^2\right\}. \tag{2.57}$$

The variable, y, in the blending functions (Eq. 2.53 and 2.57) corresponds to distance of the first node of the computational domain from the wall.

Reynolds Stress Model

The Reynolds stress model does not use the eddy viscosity hypothesis to determine the Reynolds stresses. Instead, the model solves the following equations to determine the Reynolds stresses,

$$\frac{\partial}{\partial t}(\overline{\rho}\widetilde{u_i^{"}u_j^{"}}) + \frac{\partial}{\partial x_i}(\overline{\rho}\widetilde{u}_i\widetilde{u_i^{"}u_j^{"}}) = P_{ij} + D_{ij} - \epsilon_{ij} + \pi_{ij} + \Omega_{ij}, \tag{2.58}$$

where P_{ij} is the production, D_{ij} is the diffusion, ϵ_{ij} is the dissipation, π_{ij} is the transport due to turbulent pressure-strain interaction, and Ω_{ij} is the transport due to rotation of the Reynolds stresses. The details of the exact forms of the terms in Eq. 2.58 are available in [11]. The Reynolds stress model is fairly more accurate than other models, however, the model has problems in flow field prediction if ϵ is poorly predicted by its transport equation [11]. Another disadvantage of this model is that it requires additional computational cost than other RANS modelling approaches due to the additional transport equations to be solved.

2.4.3 Large Eddy Simulation

Large Eddy Simulation (LES) is another simulation method for turbulent flow, which can be placed between the RANS and DNS techniques. The technique is widely used for non-reacting flows [16, 17]. LES uses a spatial filtering operation, which separates larger and smaller eddies based on the filter size. The spatial filtering separates the larger and smaller eddies, where the larger eddies are resolved from the filtered Navier-Stokes equations, whereas the smaller eddies are modelled. The effect of the resolved eddies on smaller eddies are represented by Sub-Grid-Scale (SGS) stresses.

LES requires significantly higher computing resources than most of the RANS techniques. In LES, the grid spacing in the simulation domain is proportional to the filtering width, which must be fine enough to accommodate the range of inertial subrange of the flow [3]. In addition, LES must take the mean and fluctuation into account in three dimension, which means that the computations cannot be performed in two-dimensional space. LES has been gaining its popularity over the past years with advances in parallel computing, however, it is still at the stage of its development.

2.5 Turbulent Reacting Flows and Non-premixed Combustion

Turbulent combustion is frequently observed in many applications such as gas furnace and internal combustion engine. During the process, turbulent flow undergoes chemical reaction, which is complicated to be analyzed. In addition to the Navier-Stokes equations, the effects of reactions occuring in the flow field must be considered in turbulent combustion modelling. In this section, some important concepts in the modelling of turbulent non-premixed combustion are briefly described.

2.5.1 Damköhler Number

In turbulent combustion process, there are two main key parameters: turbulence and chemistry. The interactions between turbulence and chemistry have a significant impact on both the species concentration and temperature. The species concentrations are enhanced by turbulent mixing, which in turn the chemical reaction rates to be changed. Conversely, the chemical reactions play a huge role in changing temperature and density, which in result, changes the structure of the turbulent flow field. The ratio between the chemical and turbulent timescales, therefore, is a very crucial in terms of analyzing reacting flows. Damköhler number, Da, is a dimensionless number, which represents the ratio between the chemical and turbulent timescales [18]

$$Da = \frac{\text{Diffusive time scale}}{\text{Chemical time scale}} = \frac{\tau_t}{\tau_c}. \tag{2.59}$$

If $Da >> 1$, reactions occur faster than the turbulent mixing, which implies that the reaction rates are greater than the turbulent mixing. Conversely, if $Da << 1$, turbulent mixing occurs faster than the chemical reaction. The Damköhler number is very useful for modelling non-premixed reacting flows: if Da is relatively large, a 1-step infinite rate reaction can be assumed with little impact on the overall results [19].

2.5.2 Mixture Fraction

In non-premixed flame, the structure of the flame depends on the mixing field between the fuel and oxidizer. The concept of mixture fraction is one of the main key concepts required for successful analysis of non-premixed flames. One of the great advantages of

mixture fraction is that the mixing of all the reactive scalars are allowed to be described by a single variable. The mixture fraction, ξ, is a normalized scalar, which represents the ratio of fuel stream and oxidizer stream in a given location within the flow regime. The mixture fraction is defined as

$$\xi = \frac{\text{mass originating from fuel}}{\text{total mass of mixture}}. \tag{2.60}$$

In a simple two stream mixing, where fuel and oxidizer are supplied from separate inlets, mixture fraction can be expressed as

$$\xi = \frac{\dot{m}_f}{\dot{m}_f + \dot{m}_o}, \tag{2.61}$$

where $\dot{m}_f$ is the mass flow of the fuel stream and $\dot{m}_o$ the mass flow of the oxidizer stream. In non-reacting multi-component flows, the species mass fractions are linearly proportional to the mixture fraction. If the diffusivities for all species are assumed to be equal, the mixture fraction can be assumed to be a conserved scalar. The governing transport equation for mixture fraction can be written as

$$\frac{\partial(\rho\xi)}{\partial t} + \frac{\partial(\rho u_i \xi)}{\partial x} = \frac{\partial}{\partial x_i}\left(\rho D \frac{\partial \xi}{\partial x_i}\right), \tag{2.62}$$

where D is the mixture fraction diffusivity. As shown in Eq. 2.62, the transport equation of mixture fraction does not include any source or sink terms, which means that ξ is conserved. Applying the Favre averaging technique, Eq. 2.62 becomes

$$\frac{\partial(\overline{\rho}\widetilde{\xi})}{\partial t} + \frac{\partial(\overline{\rho}\widetilde{u}_i\widetilde{\xi})}{\partial x} = \frac{\partial}{\partial x_i}\left(\overline{\rho} D \frac{\partial \widetilde{\xi}}{\partial x_i} - \overline{\rho}\widetilde{u"_i \xi"}\right), \tag{2.63}$$

where the turbulent flux, $\widetilde{u"_i \xi"}$, can be modelled by the gradient diffusion assumption

$$\widetilde{u"_i \xi"} = -D_t \frac{\partial \widetilde{\xi}}{\partial x_i}, \tag{2.64}$$

where D_t is turbulent diffusivity. The transport equation for the mean mixture fraction variance, $\widetilde{\xi"^2}$, is given by

$$\frac{\partial(\overline{\rho}\widetilde{\xi"^2})}{\partial t} + \frac{\partial(\overline{\rho}\widetilde{u}_i\widetilde{\xi"^2})}{\partial x} + \frac{\partial(\overline{\rho}\widetilde{u_i \xi"^2})}{\partial x} = 2\overline{\rho} D_t \left(\frac{\partial \widetilde{\xi"}}{\partial x}\right)^2 - \overline{\rho}\widetilde{\chi}, \tag{2.65}$$

where the turbulent flux term, $\widetilde{u"\xi"^2}$, is modelled using the gradient diffusion hypothesis. The mean scalar dissipation rate, $\widetilde{\chi}$, on the RHS of Eq. 2.65 will be discussed in Section 2.5.3.

2.5.3 Mean Scalar Dissipation Rate

The mean scalar dissipation rate, $\widetilde{\chi}$, is an important parameter which connects the mixing and combustion fields. The dissipation rate of variance of scalar in small scales due to turbulent micromixing is described by the mean scalar dissipation rate, which is proportional to the inverse of the diffusive time

$$\chi \sim \tau_t^{-1}. \tag{2.66}$$

Equation 2.66 can be further expanded using the definition of Damköhler Number,

$$\chi \sim (\tau_c Da)^{-1}. \tag{2.67}$$

A very small value of $\widetilde{\chi}$ implies that the combustion process occurs at the condition close to the equilibrium or the fast chemistry limit. Increase in $\widetilde{\chi}$ indicates that diffusive time decreases and the reaction zone is strained, resulting more heat being removed from the reaction zone, thus lowering reacting rates and temperature [11].

2.6 Models for Turbulent Non-premixed Combustion

Accurate modelling of the different physical process involved in combustion is crucial in order to improve thermal efficiency of combustion devices and reduce atmospheric emissions. In most industrial applications such as furnaces, gas turbines, and internal combustion engines, combustion occurs in turbulent flow conditions. Several models have been developed to model the turbulent combustion process. In this section, an overview of some of existing turbulent non-premixed combustion models is presented.

2.6.1 Infinitely Fast Chemistry

In non-premixed turbulent combustion, it is commonly assumed that the time scales of chemical reactions are infinitely smaller than the convection and diffusion time scales. This allows the use of infinitely fast chemistry to be appropriate. A popular model for non-premixed combustion used in the industry is Eddy Dissipation Concept (EDC) [20]. The main assumption in the EDC model is that the reaction rate is proportional to the rate of mixing between reactants and products for fast chemistry, such that the mean reaction rate of fuel, $\overline{\dot{\omega}_F}$, can be obtained by solving

$$\overline{\dot{\omega}_F} = C_{mag}\overline{\rho}\frac{\epsilon}{k}\min\left(\widetilde{Y}_F, \frac{\widetilde{Y}_O}{r}, \beta\frac{\widetilde{Y}_P}{(1+r)}\right), \tag{2.68}$$

where C_{mag} and β are empirical constants which can be adjusted, and r is the oxygen-fuel stoichiometric mass ratio. Subscripts F, O, and P in Eq. 2.68 are fuel, oxidizer, and products, respectively. The advantage of EDC model is that it is simple and requires lower computational cost compared to other combustion models. However, the model has difficulties in prediction with the existence of ignition, quenching or stabilization mechanism.

2.6.2 Laminar Flamelet Model

Laminar Flamelet Models (LFM) is a relatively simple combustion model which takes account for detailed chemistry [21]. The model assumes the turbulent flame consists of an ensemble of stretched laminar flamelets. In LFM, turbulent flames are described as a set of flamelets, where the major chemical reactions and heat release occur. The model assumes that the fuel and oxidant react in locally thin zones in a condition that the chemical time scales are much shorter than that of the characteristic turbulence (i.e. high Da). The laminar flamelet equation is given by

$$\frac{\partial Y_i}{\partial t} = \frac{\chi}{Le_i}\frac{\partial^2 Y_i}{\partial \xi^2} + \dot{\omega}_i, \tag{2.69}$$

where Le_i is the Lewis number of specie i, which describes the ratio between the thermal diffusivity and mass diffusivity of the specie. The properties such as species mass fractions depending on the mixture fraction, ξ, are evaluated and stored in a tabulated form (flamelet libraries). The scalar dissipation rate, χ, determines the effect of flame stretching of the actual turbulent flame. The Favre averaged species mass fraction can be obtained by

$$\widetilde{Y}_i(x_i, t) = \int_0^1 \int_0^\infty Y_i(\eta, \chi_s, t)\widetilde{P}(\eta, \chi_s, x_i, t)d\chi_s d\eta, \tag{2.70}$$

where χ_s is the scalar dissipation rate at the flame surface and η is the sampling mixture fraction.

The main advantage of the laminar flamelet method is that detailed chemistry can be adapted within the calculations at low cost since the library contains information of temperature, density, and species. However, the main limitation of the model is related to the assumption that all chemical time and length scales remain smaller than the length scale of the characterized smallest eddy, which is not verified for practical combustion cases in often. This limitation also makes the laminar flamelet model unsuitable for prediction of autoignition or flames with large chemical timescales.

2.6.3 Transported PDF Model

Transported PDF method was first proposed by Pope [22]. The method is not restricted by the flamelet assumption, and it solves the joint PDF of velocity, scalar dissipation, and composition instead of assuming the shape of the PDF. One of the advantages of the model is that the chemical source term is closed, and can be used for both premixed and non-premixed flames while providing an accurate representation of the joint PDF of several scalar variables [23]. Since the PDF transport equation has high dimensionality, Pope [24, 25] proposed solving the PDF equation stochastically using Monte-Carlo simulation techniques. By doing this, the evolution of joint PDF is estimated by a large number of stochastic particles. Overall, the model has been shown to perform well for various flames [26]. However, several issues must be addressed in the method. The transported PDF method still requires modelling for the mixing term closure, and the overall performance of the PDF method is dependent on the submodel chosen for the unclosed term. The modelling of the mixing term presents one of the most challenging issues in PDF methods. Another limitation of the transported PDF method is that the method requires substantial computational resources compared to other combustion models such as LFM.

2.6.4 Conditional Moment Closure

Conditional Moment Closure (CMC) was developed independently by Klimenko [27] and Bilger [28]. The model is also not restricted by the flamelet assumption. In CMC, conditional averages of species and temperature are considered by selecting a conditioning variable and assuming that the fluctuations about the temperature and mass fraction of species are associated with the selected variable. The assumption is so called the first order closure for CMC. In non-premixed flames, the scalar fluctuations mostly depend on the mixture fraction, which makes the mixture fraction a good candidate for the conditioning variable. Using the CMC approach, the mean value of the scalar field f is obtained by

$$\widetilde{f} = \int_0^1 \langle f|\eta\rangle \, \widetilde{P}(\eta) d\eta, \tag{2.71}$$

where $\langle f|\eta\rangle$ is the conditional average of $\widetilde{f}$. The conditional average is conditioned on the mixture fraction space ranging from 0 to 1. The mixture fraction dimension is discretized into a determined number of bins and the conditional average corresponds to the average value at each bin. The conditional averages are obtained by solving the conditional transport equation in the mixture fraction sample space. The first order closure is often used

to close the chemical source term, allowing

$$\langle \dot{\omega}_k|\eta\rangle = \dot{\omega}(\langle T|\eta\rangle\,, \langle Y_k|\eta\rangle\,, \langle \rho|\eta\rangle), \tag{2.72}$$

where $\langle \dot{\omega}_k|\eta\rangle$ is the conditional averaged chemical source term of species k, $\langle T|\eta\rangle$ the conditional averaged temperature, $\langle Y_k|\eta\rangle$ the conditionally averaged species mass fraction of specie k, and $\langle \rho|\eta\rangle$ the conditionally averaged density of mixture.

CMC has been successful for various turbulent non-premixed configurations and a good review of these studies may be found in [4, 29]. Although in principle, CMC is applicable to any combustion regime, some assumptions need to be made for the closure of some terms in the CMC transport equations. These additional unclosed terms can be difficult to model, in particular to the cases close to ignition or extinction due to huge fluctuations in species and temperature [30, 31, 32]. CMC method may be computationally expensive since the method solves additional CMC equations for species in space, time, and sample space.

2.6.5 Multiple Mapping Conditioning

Multiple Mapping Conditioning (MMC) has been recently proposed by Klimenko and Pope [33]. The basic idea of the MMC model is to combine the PDF and CMC methods in a way that the non-premixed combustion is modelled as expectations of all scalars conditioned on a set of random reference variables with a joint PDF. MMC has been developed as a general formulation of mapping closure methods using deterministic and stochastic frameworks. It has been found that the model is able to reproduce non-premixed flames accurately [34, 35]. The model is still at the early stage of development.

2.6.6 Conditional Source-term Estimation

Conditional Source-term Estimation (CSE) was first proposed by Bushe and Steiner [36]. Similar to the idea of CMC, CSE uses conditional averages for the chemical source term closure. In CSE, the conditional average of the chemical source term is determined by first order averages, which is also used in CMC. The conditional averages in CSE are obtained by inverting an integral unlike transport equation is solved to obtain the averages in CMC. Further details of this model are discussed in Chapter 3.

2.7 Summary

The background information required for understanding of the general modelling techniques is introduced in this chapter. Details on the governing equations for fluid flow, averaging techniques, statistical description of turbulent flow, and turbulence modelling are covered in this chapter as well as an overview of the existing turbulent combustion modelling methods. The following chapter provides more detail of the CSE method including its principle and relevant submodels.

Chapter 3

Conditional Source-term Estimation (CSE) for Non-premixed Turbulent Combustion

In this chapter, Conditional Source-term Estimation (CSE) along with the required submodels are introduced. Starting from the basic principle of CSE, the details on submodels are presented. Followed by the details of submodels, the methodology of CSE implemented in Computational Fluid Dynamics (CFD) is described. Finally, an overview of the previous studies on the application of CSE are covered which leads to the objective of the current study.

3.1 Principle

The basic idea of CSE is similar to CMC, where the closure for chemical source term is achieved in the conditional space. For N chemically reactive species in a turbulent flame, $(N - 1)$ Favre-averaged species transport equations are solved with the last species mass fraction being determined by conservation of mass, in addition to the flow and enthalpy equations. In each species transport equation, the mean chemical source term needs to be calculated. The present description is focused on the CSE implementation in RANS, but the concept would be similar in LES [37]. In non-premixed combustion, the mixture fraction is a conserved quantity and the common choice of the conditioning variable in non-premixed combustion. The mixture fraction varies between 0 for pure air and unity

for pure fuel. Using conditional averages, the mean chemical source term is found by

$$\overline{\dot{\omega}_k}(x_j,t) = \int_0^1 \langle \dot{\omega}_k|\eta\rangle(\eta,x_j,t)\bar{P}(\eta,x_j,t)d\eta. \tag{3.1}$$

In Eq. 3.1, $\overline{\dot{\omega}_k}$ is the mean chemical source term for species k, $\langle\dot{\omega}_k|\eta\rangle$ the chemical reaction rate for species k conditionally averaged on a value η of the mixture fraction sample space, ξ, $P(\eta,x_j,t)$ the PDF of η, x_j the spatial coordinate, and t the time. The PDF of mixture fraction are obtained from the mean and variance of the mixture fraction, which will be discussed in Section 3.4. Thus, in Eq. 3.1, the only unknown is the conditional chemical reaction rate of species k. Applying the first order closure for the reaction rates, the conditional chemical source term may be assumed to follow,

$$\langle\dot{\omega}_k|\eta\rangle \quad \simeq \quad \dot{\omega}_k(\langle Y_i|\eta\rangle\,,\langle T|\eta\rangle), \tag{3.2}$$

where $\langle Y_i|\eta\rangle$ is the conditional mass fraction of species i, and $\langle T|\eta\rangle$ the conditional temperature. First order closure for the conditional chemical source term is applied, which implies that the fluctuations about the conditional averages are assumed to be negligible, and is commonly used in CMC as well [4]. This approximation is valid for flames far from extinction conditions and without ignition.

In Eq. 3.2, in order to determine $\langle\dot{\omega}_k|\eta\rangle$, the conditional species mass fractions and conditional temperature, which are initially unknown, need to be calculated. In CSE, these conditional scalars are obtained by inverting the following integral,

$$\widetilde{f}(x_j,t) = \int_0^1 \langle f|\eta\rangle(\eta,x_j,t)\tilde{P}(\eta,x_j,t)d\eta, \tag{3.3}$$

where f may be the mass fraction of species k, temperature, or enthalpy. It is important to note that the Favre averaged species mass fraction, temperature, or enthalpy are known at a given time or iteration as transport equations for these quantities are solved during CFD simulation. Once all conditional scalars are found by inversion, the unconditional chemical source term, $\overline{\dot{\omega}_k}$, may be retrieved by using Eq. 3.1 and returned as a source term to the species transport equations.

In practice, due to the large number of species, N, that are considered, it is not possible to invert Eq. 3.3 for all the species present in the chemical mechanism. Instead, only two inversions will be performed assuming that the chemistry can fully characterized by two species mass fractions at a given η. Consequently, the quality of CSE implementation strongly depends on (i) the inversion method needed to invert Eq. 3.3 and (ii) the chemistry tabulation technique. These two aspects are examined in the following sections.

3.2 Inversion Method

In order to invert Eq. 3.3, CSE takes advantage of the fact that the conditional averages vary less in space compared to the unconditional averages [4]. Instead of defining a coarse grid for the conditional averages like in CMC, the computational domain is divided into ensembles, and the conditional averages within the CSE ensembles are assumed to be homogeneous. The homogeneity of the conditional averages allows spatial independence of the conditional averages within an ensemble. Further detail on the definition of the ensemble will be provided in Section 3.5. Thus, Eq. 3.3 can be re-written as

$$\widetilde{Y}_k(x_j,t) = \int_0^1 \langle Y_k|\eta\rangle(\eta,t)\tilde{P}(\eta,x_j,t)d\eta. \tag{3.4}$$

Notice that the spatial dependence of the conditional mass fraction of species k is now removed in Eq. 3.4 compared to Eq. 3.3 due to the homogeneity assumption. Equation 3.4 is a Fredholm integral of the first kind and can be written in matrix form such as

$$\vec{b} = A \;.\; \vec{\alpha}, \qquad A = A_{j,m} = \int_{\eta_m}^{\eta_{m+1}} \tilde{P}(\eta,x_j,t)d\eta, \tag{3.5}$$

where $\vec{b}$ is the vector including all values of $\widetilde{Y}_k(x_j,t)$, A the matrix of integrated PDF over a discretized mixture fraction interval, $\vec{\alpha}$ corresponds to the vector containing $\langle Y_k|\eta\rangle$, j the spatial coordinate index, and m the mixture fraction bin index. In CSE, the solution of interest is expressed as

$$\vec{\alpha} = A^{-1}\vec{b}. \tag{3.6}$$

Equation 3.6 is typically ill-posed meaning that the solution is sensitive to small perturbations in the system [38]. The ill-posedness of the problem can be resolved by using regularization method, which yields a stable, smooth, and unique solution of the inverse problem. There are several regularization methods available including Truncated Singular Value Decomposition (TSVD) [39] and Tikhonov regularization technique [40]. In the present work, zeroth order Tikhonov regularization is selected. First order (spatial) Tikhonov regularization methods could be used to obtain a smooth and unique solution with advantage of not depending on the accuracy of the solution from the previous time step [41]. However, first order Tikhonov methods add significant complexity and is not considered in the present work. Further, zeroth order Tikhonov regularization has been shown to work well in CSE [42, 43, 44]. Zeroth order Tikhonov is applied to Eq. 3.6 and results in

$$\vec{\alpha} = \arg\min \left\| \begin{bmatrix} A \\ \lambda I \end{bmatrix} \vec{\alpha} - \begin{bmatrix} \vec{b} \\ \lambda\vec{\alpha}^0 \end{bmatrix} \right\|_2^2, \tag{3.7}$$

where $||.||_2^2$ is the L2-norm of a vector, I the identity matrix, $\vec{\alpha}^0$ some $a-priori$ knowledge of the solution, and λ the regularization parameter. Several initial solutions for $a-priori$ knowledge are possible. In the present study, the strategy proposed by Grout *et al.* [41] is implemented: the solution from previous time step is taken as $a-priori$ and the regularization parameter can be obtained by solving

$$\lambda^2 = \frac{Tr(A^T A)}{Tr(I)}, \tag{3.8}$$

where Tr is the trace of the matrix. Finally, Eq. 3.8 is solved by Lower Upper (LU) decomposition method.

The conditional averages are obtained by solving Eq. 3.6. By solving the inversion of integral equation, the constraining assumptions of the fast chemistry is not required. In addition, solving the transport equations to obtain the conditional averages in CMC are no more required in CSE.

3.3 Chemistry Tabulation

The inclusion of detailed chemistry into the simulation can result in large computational cost due to the large number of species that need to be considered and solved for. The cost for solving detailed chemistry during the simulation can be avoided using a tabulated chemistry, where the species reaction rates and mass fractions can be simply retrieved from a pre-built chemistry table. In the present work, tabulated chemistry via Trajectory Generated Low Dimensional Manifold (TGLDM) approach is applied [45]. This chemistry tabulation has been successfully incorporated into previous CSE calculations for methane-air combustion. Thus, this appears to be the logical choice for the present simulations of methanol combustion. The principle is briefly summarized.

Using the conservation of chemical elements at specified mixture fraction values, a bounded manifold is formed in a composition space. The boundary points of the manifold is set as the initial point of trajectories. From each initial points, the chemistry trajectories evolve towards the equilibrium point by solving the governing ordinary differential equation for each species,

$$\rho \frac{\partial Y_k}{\partial t} = \dot{\omega}_k, \tag{3.9}$$

ρ being density of the mixture. The manifold produced by all of the trajectories simulated are stored as a function of the mass fraction of carbon dioxide (Y_{CO_2}) and water (Y_{H_2O}) due

to their long formation times [46]. Figure 3.1 illustrates the evolved trajectories represented by the mass fractions of (Y_{CO_2}) and water (Y_{H_2O}). In Fig. 3.1, the solid blue line represents the imaginary boundaries at the given mixture fraction. Within the boundary lines, the initial points or trajectory seeding points are set. A single trajectory evolves from the specified seeding point towards the equilibrium point, which is shown as the red star in Fig. 3.1. After all the trajectories are simulated at each starting point, any redundant points within the manifold are removed.

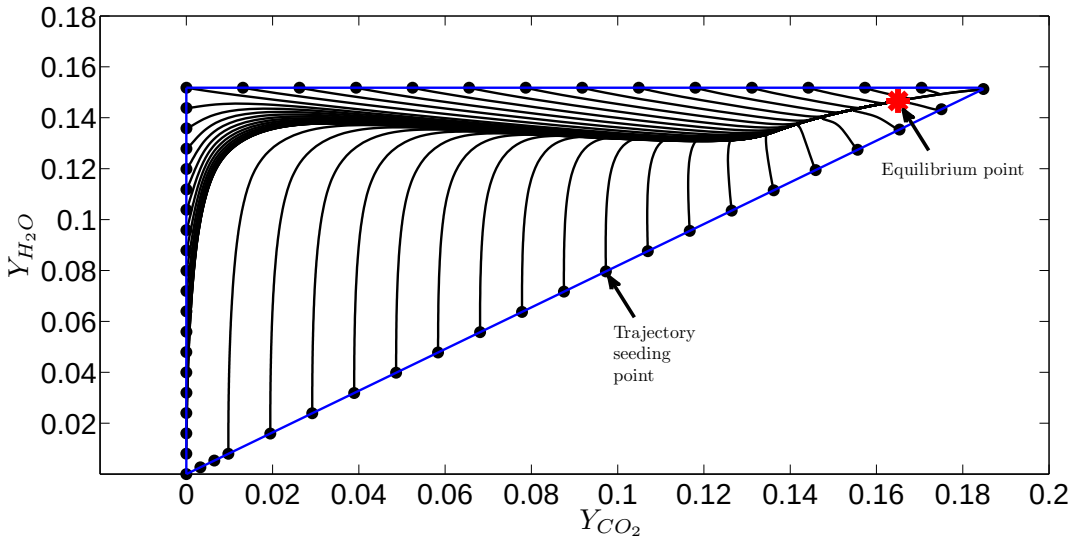

Figure 3.1: Illustration of chemistry trajectories in Y_{CO_2} and Y_{H_2O} space (for $\eta = 0.135$ in methanol-air combustion)

Finally, Delaunay triangulation method is applied to extract required species conditional chemical source term at particular Y_{CO_2} and Y_{H_2O} values from the inversion process. The manifold after the triangulation process is illustrated in Fig. 3.2, and Fig. 3.3 shows the reaction rate of CO_2 mapped with the triangulation. In Fig. 3.3, the unit for the reaction rate is per second.

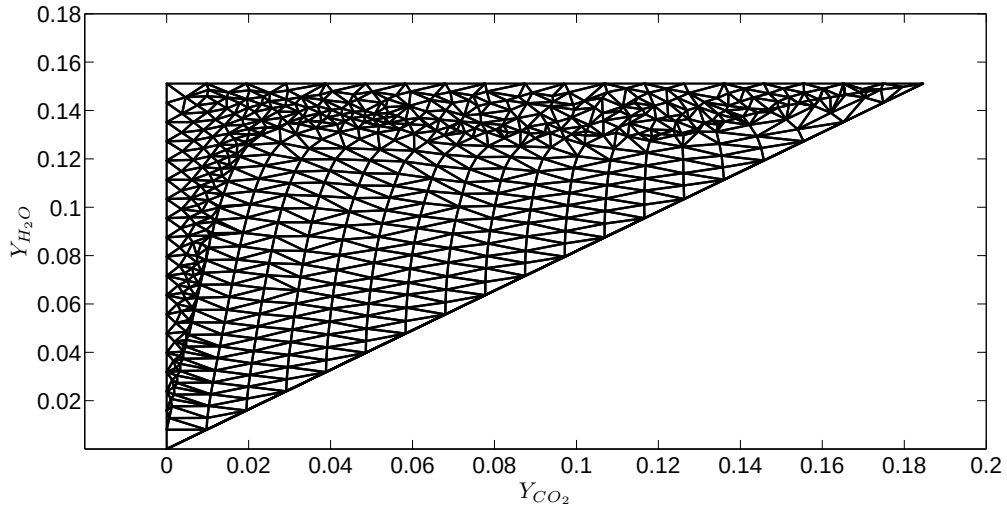

Figure 3.2: TGLDM manifold with Delaunay triangulation at $\eta = 0.135$

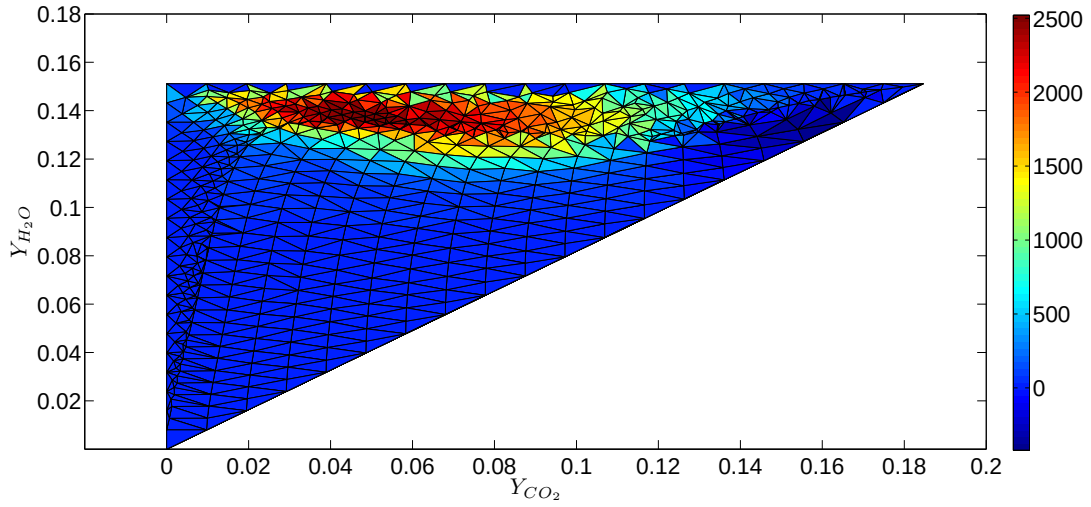

Figure 3.3: Reaction rate of CO_2 (per second) plotted on the TGLDM manifold with Delaunay triangulation at $\eta = 0.135$

3.4 Presumed Probability Density Function

In CSE, the role of the PDF is crucial. The PDF is used in both the inversion process to obtain the conditional averages as well as for the calculation of the unconditional chemical source term of species. Therefore, a good approximation of PDF is required for CSE to provide accurate results. In combustion applications, a presumed shape of PDF based on one or two parameters can be adopted [47]. For non-premixed combustion, the mean and variance of the mixture fraction from their transport equations are used for the shape of the presumed PDFs. There are several presumed PDFs that are commonly used in turbulent combustion such as clipped Gaussian PDF and $\beta-$PDF. In the current CSE method, a $\beta-$PDF is employed as the presumed PDF of the mixture fraction. In this section, a brief introduction of $\beta-$PDF is introduced.

The β-PDF of mixture fraction in Favre averaged form [48] is defined as

$$\widetilde{P}(\eta) = \frac{\eta^{\alpha-1}(1-\eta)^{\beta-1}}{I_b}, \tag{3.10}$$

where I_b is given by

$$I_b = \int_0^1 \eta^{\alpha-1}(1-\eta)^{\beta-1} d\eta. \tag{3.11}$$

In Eq. 3.10, and Eq. 3.11, α and β are the parameters defined as following

$$\alpha = \widetilde{\xi}\left(\frac{\widetilde{\xi}(1-\widetilde{\xi})}{\widetilde{\xi''^2}} - 1\right), \tag{3.12}$$

$$\beta = \left(1-\widetilde{\xi}\right)\left(\frac{\widetilde{\xi}(1-\widetilde{\xi})}{\widetilde{\xi''^2}} - 1\right). \tag{3.13}$$

The β distribution is a smooth PDF where the shape of it varies with $\widetilde{\xi}$ and $\widetilde{\xi''^2}$, which is illustrated in Fig. 3.4. The β distribution is defined only in the range of $0 \leq \eta \leq 1$, and it is either zero or asymptotic to infinity at the boundaries. In the flow field, the distribution of mixture fraction is not uniform over the flow region: the well-mixed zone has Gaussian distribution while the unmixed zone has single or double-delta distributions. The β function is able to change continuously from the PDF shapes with one or multiple peaks to uniform Gaussian shapes [49]. Girimaji [48] shows that the β distribution is

capable of providing an accurate results of $\widetilde{P}(\eta)$, which is supported by the DNS results [48, 50, 51]. The β distribution has been included in a wide range of studies and flow types [52, 53, 54].

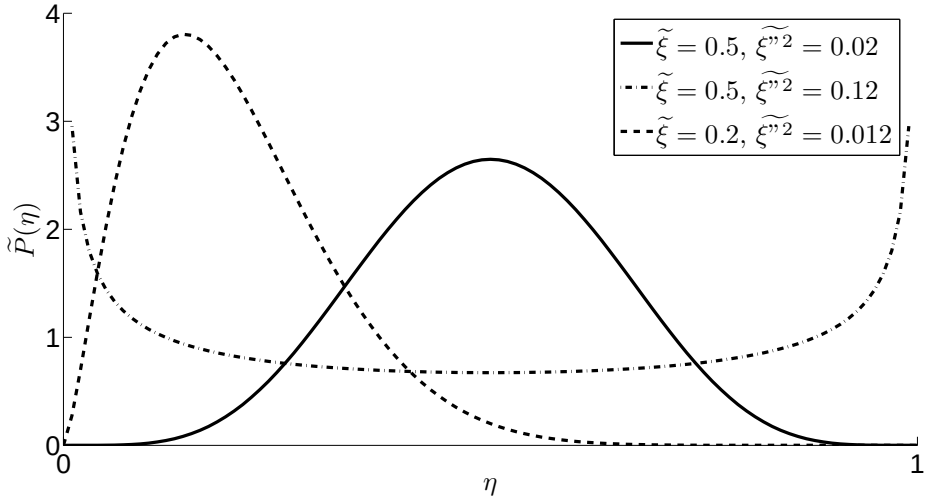

Figure 3.4: $\beta-$PDF of mixture fraction for different value of $\widetilde{\xi}$ and $\widetilde{\xi''^2}$

3.5 Current Implementation of CSE in CFD

In the CFD spatial domain, the CSE ensembles are defined as a set of planes at several axial locations, normal to the centreline axis keeping the entire radial length of the computational domain, as shown in Fig. 3.5. In Fig. 3.5, the thin lines are the computational mesh within the domain, the thick solid lined box represents the first CSE ensemble within the computational domain, and the thick broken lined box represents the second CSE ensemble. Notice that there is a slight overlap between each CSE ensemble. The overlap exists to prevent possible sharp changes in the conditional averages between ensembles.

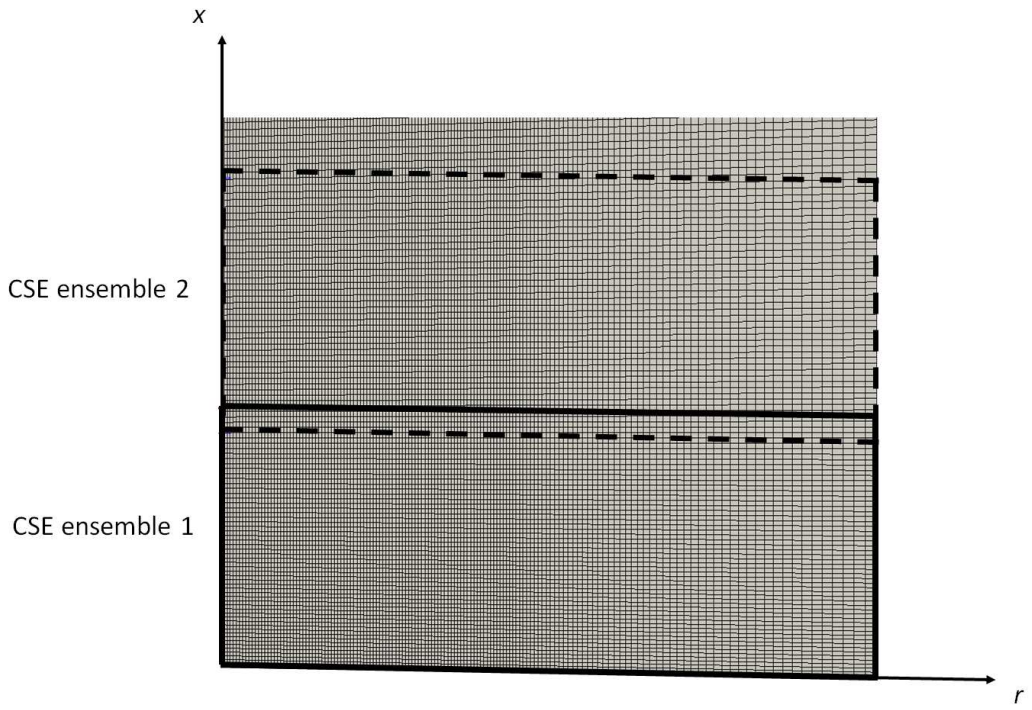

Figure 3.5: Illustration of CSE ensembles within CFD domain (thin solid line : computational mesh, thick solid lined box : first CSE ensemble, thick broken lined box : second CSE ensemble)

In the present study, the CSE routines and TGLDM tables are integrated with the OpenFoam [55] CFD solver . The interactions between the CSE method coupled with the tabulated chemistry via TGLDM and the CFD code are illustrated in Fig. 3.6. From the CFD module, the governing transport equations such as continuity, momentum, enthalpy, species, mixture fraction, and variance of mixture fraction are solved. The mixture fraction space is discretized into a selected number of sampling mixture fraction values. The mixture fraction PDF is calculated by the mean and variance of the mixture fraction from the CFD module using the presumed β function described in Section 3.4. The PDF and the Favre averaged mass fractions of carbon dioxide ($\widetilde{Y}_{CO_2}$) and water ($\widetilde{Y}_{H_2O}$) within a given ensemble are needed to perform the inversion, as shown by Eq. 3.3. An inversion is performed for each ensemble using the inversion method introduced in Section 3.2. As a result, the conditional mass fractions of CO_2 and H_2O are obtained for each ensemble.

Following the fundamental principle of CSE, the conditional reaction rates of all the

reactive species at each sampling mixture fraction have to be retrieved from the chemistry table to obtain the unconditional species reaction rate, which is used as source term in corresponding species transport equations as shown in Eq. 3.15. From the previous CSE study by Wang *et al.* [56], however, it is found that significant computational savings could be achieved by interpolating for minor species conditional mass fractions directly from the TGLDM table rather than solving the transport equations for those species. The interpolated mass fraction of the minor species are then fed back to the CFD physical space, where the results are still in good agreement with the experimental data. The current implementation of CSE extends the method used in Wang *et al.* [56]: the conditional reaction rates are obtained for CO_2 and H_2O only, while the conditional mass fractions of the remaining species are directly retrieved from the TGLDM tables (Section 3.3). As a result, the unconditional species reaction rates of CO_2 and H_2O are calculated by solving the integral

$$\overline{\dot{\omega}}_k(x_j,t) = \int_0^1 \langle \dot{\omega}_k|\eta\rangle(\eta,t)\bar{P}(x_j,\eta,t)d\eta, \tag{3.14}$$

which are then fed back to the CFD module to solve for the corresponding species transport equation,

$$\frac{\partial}{\partial t}(\overline{\rho}\widetilde{Y}_k) + \frac{\partial}{\partial x_i}(\overline{\rho}\widetilde{u}_i\widetilde{Y}_k) = \frac{\partial}{\partial x_i}(\frac{\mu_t}{Sc_{kt}}\frac{\partial \widetilde{Y}_k}{\partial x_i}) + \overline{\dot{\omega}}_k. \tag{3.15}$$

Meanwhile, the Favre-averaged mass fractions of the remaining species are directly obtained by solving

$$\widetilde{Y}_k(x_j,t) = \int_0^1 \langle Y_k|\eta\rangle(\eta,t)\widetilde{P}(x_j,\eta,t)d\eta. \tag{3.16}$$

The inversion and integration processes occur for all CSE ensembles within the computational domain. The entire process is repeated every CFD time step until the simulation converges.

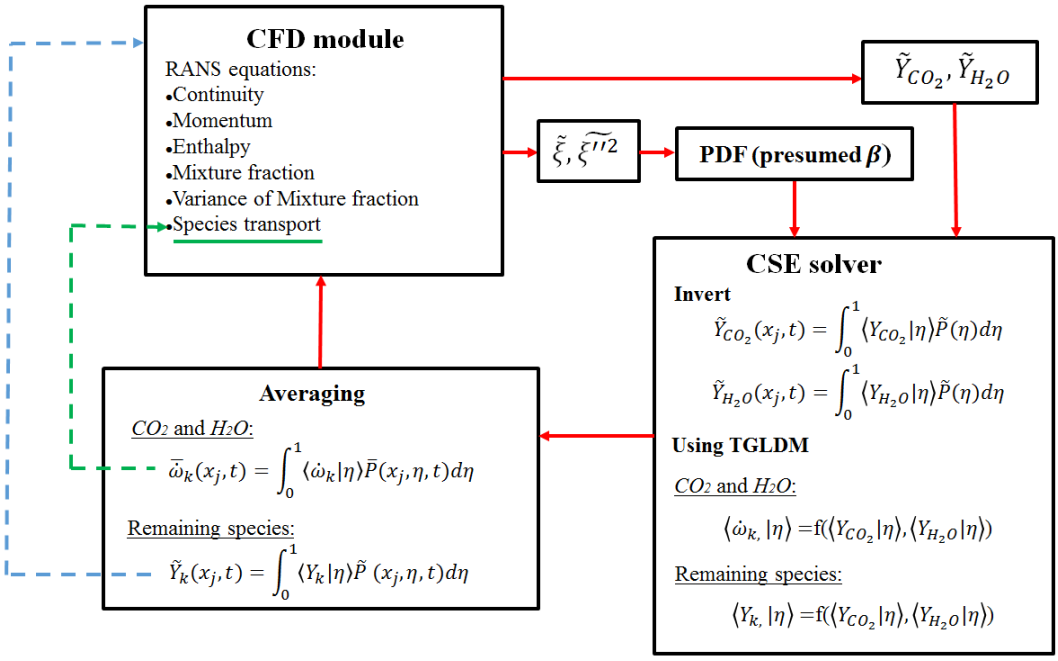

Figure 3.6: Integration of CSE with TGLDM tables in CFD

3.6 Previous Studies on CSE

CSE has been applied to simulate a range of flames, and previous CSE studies have shown that the model is able to predict the flame characteristics successfully. In this section, a brief overview of previous CSE studies are provided.

Non-premixed

Labahn and Devaud [42] investigate the confined methane-air flame at atmospheric conditions using CSE in RANS simulation. In their work, the sensitivity analysis on the size of the CSE ensembles are investigated, and it is found that the size of the ensembles has a significant impact on the simulation results. After selecting the proper size of the CSE ensemble, the temperature field computed from the CSE simulation is compared with the

available experimental data [57] and previously simulated results using CMC [58, 59] and flamelet method [60]. Overall, the CSE results agree well with the experimental data. Some discrepancies with the experimental data are believed to be due to the lack of a soot modelling in the simulation [42].

The Moderate and Intense Low Oxygen Dilution (MILD) combustion mode is investigated using CSE in RANS by Labahn *et al* [61]. In their work, the non-premixed CSE method is extended by adding a second mixture fraction. Two flames at different Reynolds numbers are investigated. The fuel is Dutch natural gas which can be approximated by 15 % N_2 and 85 % CH_4 by volume. In their study, the CSE results for temperature and mixing field are compared with the experimental data [62, 63]. Overall, the CSE results represent the experimental data accurately. The investigation of MILD combustion with CSE are extended to LES framework in Labahn and Devaud [64]. The same two flames in [61] are simulated in LES using the two mixture fraction CSE, and the instantaneous results of flow and temperature field are found to be accurate compared to the experimental data [62, 63].

Wang *et al*. simulate the Sandia D-flame using CSE in LES [56]. They test two different chemical kinetics, GRI-Mech 2.11 [65] and GRI-Mech 3.0 [66], and both of them are capable of obtaining accurate predictions of the temperature and major species. In their work, the conditional mass fractions of species as well as the Favre averaged species mass fraction are examined to evaluate the accuracy of CSE. For both quantities, the CSE results agree well with the experimental data [67] for the major reactive species. For the prediction of Nitric oxide, NO, it is observed that the prediction by CSE using GRI-Mech 2.11 provides more accurate predictions than the case using GRI-Mech 3.0.

There have been studies on applicability of CSE to predict the ignition delay of turbulent jet. Huang and Bushe [68] and Grout *et al*. [41] examine the ignition and combustion processes of transient turbulent methane jets under engine-relevant conditions using CSE method. From both studies, CSE predicts the experimental ignition delay accurately as well as the ignition kernel locations [69, 70, 71] .

Premixed

In addition to non-premixed combustion, CSE has been also applied to simulate premixed flames. Jin *et al*. [72] reproduce a turbulent premixed methane jet in LES and compare their CSE results to the available DNS result [73]. In their work, different types of presumed PDF models are tested including $\beta-$PDF and laminar flame-based PDF model by Bray *et al* [74]. From their investigation, it is found that the CSE results of species reaction rates with the PDF model by Bray *et al* [74]. match the DNS results most accurately

among the other presumed shapes tested, while the β PDF still captures the distribution with satisfying precision.

Salehi *et al.* [75] investigate premixed methane Bunsen burner using CSE, and the results show that CSE can predict the mean velocity and temperature field with reasonable accuracy compared to the experimental measurements [76]. Major species mass fractions are also captured well in their CSE results while some discrepancies from the experimental values are observed for OH and CO radicals.

Dovizio *et al.* [77] reproduce the turbulent premixed bluff-body methane flame using CSE. Two regularization methods for inverting integral are tested including Tikhonov regularization technique and Truncated Singular Value Decomposition (TSVD) [39]. Small differences in conditional and unconditional averages are noticed between the two regularization methods. The turbulent flow field is solved in RANS with the standard $k-\epsilon$ and SST $k-\omega$ method, and the case with SST $k-\omega$ with modified model constant provides better agreements with the experimental data [78] than the case with the standard $k-\epsilon$. Overall, good agreement is achieved between the CSE predictions and the experimental data.

In LES, Shabazian *et al.* [79] simulate two axisymmetric Bunsen-type premixed turbulent methane-air flames, corresponding to lean and stoichiometric conditions with both lying within the thin reaction zones. The LES-CSE results are compared with a traditional flamelet-based approach called the Presumed Conditional Moment (PCM) with Flame Prolongation of Intrinsic Low Dimensional Manifolds (FPI) tabulated chemistry [80, 81, 82]. The experimental measurement on the flame height [83] is reasonably well predicted by CSE.

Partially premixed

CSE has been extended to partially premixed combustion. In RANS, Dovizio *et al.* [84] investigate a range of lifted flame using Doubly CSE, which takes into account for premixed and non-premixed combustion modes. In their work, a joint PDF based on the statistical independence between mixture fraction and progress variable is used to reproduce lifted flames at three different Reynolds numbers. The CSE results of the lift-off height and flammable width for the three different conditions agree well with the experimental data [85, 86].

Table 3.1 summarizes the previous studies on CSE.

Table 3.1: Summary of previous studies on CSE

Authors	**Type**	**Flow Modelling**	**Flame**	**Fuel**
Huang and Bushe[68]	Non-premixed	RANS	Engine	Methane
Grout *et al.* [41]	Non-premixed	RANS	Engine	Methane
Wang *et al.* [56]	Non-premixed	LES	Sandia D	Methane
Labahn and Devaud [42]	Non-premixed	RANS	confined jet	Methane
Labahn *et al.*[61]	Non-premixed	RANS	MILD	Dutch natural gas
Labahn and Devaud [64]	Non-premixed	LES	MILD	Dutch natural gas
Jin *et al.* [72]	Premixed	RANS	Jet	Methane-air
Salehi *et al.* [75]	Premixed	RANS	Bunsen	Methane-air
Dovizio *et al.*[77]	Premixed	RANS	Bluff-body	Methane-air
Shabazian *et al.*[79]	Premixed	LES	Bunsen type	Methane-air
Dovizio *et al.* [84]	Partially premixed	RANS	Lifted jet	Methane-air

As listed, the previous studies show good agreement in terms of predicting the experimental data in non-premixed, premixed, and partially premixed flames. However, these previous CSE studies have been only focusing on methane and methane-based mixtures with small amounts of additives like H_2 and nitrogen gas (N_2). At this stage, there is a clear need to examine the model performance for turbulent flames that burn fuels with more complex chemical structure than that of methane.

3.7 Summary

This chapter includes an overview of the CSE model for non-premixed combustion in particular. The basic idea of achieving closure for the chemical source term in transport of

species using CSE is explained. The submodels within CSE such as the inversion, chemistry tabulation, and presumed β-PDF methods are presented. The current implementation of the CSE method in computational fluid dynamics is also discussed. Finally, this chapter provides an overview of the previous applications of CSE to simulate flames.

The following chapter provides previous studies on turbulent non-premixed methanol flames, which are reproduced using the CSE method in the present study.

Chapter 4

Previous Studies on Turbulent Non-premixed Methanol Flames

Methanol (CH_3OH) is an alternative energy source, which is already used in many applications including automobiles, space heating, and electric power generation [87]. There has been limited number of investigations on methanol flames while numerous works have been done for methane flames. In this chapter, a summary of the two experimental and related numerical studies on turbulent non-premixed methanol flames are provided: piloted flame and bluff-body flame. Followed by the experimental studies on the methanol flames, the available previous numerical works relating to these flames are covered.

4.1 Piloted Flame

The piloted burner in the University of Sydney is used to study the characteristics of turbulent methanol non-premixed flame by Masri *et al* [88]. The main focus of their investigation is to study the methanol diffusion flames near extinction. Detailed results of both conditional and unconditional temperature and reactive species concentrations are presented. In addition to the experimental measurements, Masri *et al*. [88] provide predictions of the conditional quantities yielded by the flamelet approach.

4.1.1 Experimental Method

The pilot burner consists of an axisymmetric jet with nozzle diameter, D, of 7.2 mm. The pilot is concentric to the main jet with outer diameter of 18 mm. Surrounding the main jet and the pilot, a stream of air co-flow is present. From the pilot inlet, hot gas flows into the burner, which stabilize the main flame to the nozzle. The configuration of the piloted burner is shown in Fig. 4.1. The unburnt pilot gases are composed of C_2H_2, H_2, CO_2, and undergo the following reaction

$$0.25C_2H_2 + 1.75H_2 + 0.5CO_2 + 1.5(O_2 + 3.76N_2) \rightarrow 2H_2O + CO_2 + 5.64N_2. \quad (4.1)$$

The burnt pilot gas has the same atomic composition as that of stoichiometric mixture fraction of methanol, $\xi_{st} = 0.135$ [89]. The temperature of the burnt pilot gas is around 2327 K assuming the adiabatic condition for the gas, which is about 9% higher than that of a pure methanol at the same mass flow rate.

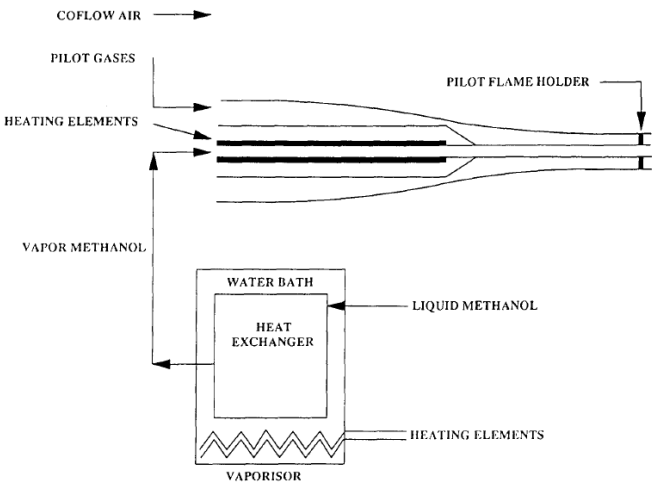

Figure 4.1: Configuration of the pilot burner in the University of Sydney, reproduced from [88]

Through the main jet, a pure methanol at 373 K enters the pilot burner. The flame is studied at a range of Reynolds numbers based on the fuel jet velocity in the experimental study. The different experimental conditions are described in Table 4.1. The mean velocity for pilot gas is kept to 21 m/s and 15 m/s for the air co-flow for the five different cases.

Table 4.1: Summary of flame turbulent pilot methanol flames condition [88]

Flame	Mean velocity of the fuel jet (m/s)	Corresponding Re
M1	66	39,200
M2	90	53,500
M3	104	62,100
M4	115	69,600
M5	127	75,600

Measurements are reported to be made using the Raman/Rayleigh/LIF technique to give instantaneous and simultaneous temperature and the concentration of many species at a single point in the flame [88]. Data files of the post-processed measurements and boundary conditions are available at the University of Sydney website [90].

4.1.2 Experimental Results

Masri *et al.* [88] report that among the five flames investigated, flame M1 is only stable. For M2 and M3, the flames are visibly unstable with extinction occurring in the intense mixing zone, and the flames are reignited intermittently further downstream. Flames M4 and M5 exhibit less re-ignition than that of M2 and M3 flames, and both M4 and M5 flames blow off after 5 fuel jet diameters from the nozzle.

From the experimental investigation of the piloted flame, a variety of results for both conditional and Favre averaged quantities are published. For the Favre averaged quantities, the mean mixture fraction, temperature, and reactive species mass fractions including CH_3OH, $O2$, CO_2, H_2O, OH, CO, and H_2 are available in [90]. The temperature and species mass fractions conditioned in mixture fractions at corresponding axial locations are included for the conditional results [88]. The conditional averages are obtained based on 50 bins in the mixture fraction grid, where the distribution of the bin is not specified. The mixture fraction for each data point is calculated using Bilger's formula [91]

$$\xi = \frac{\frac{2(Z_C - Z_{C,O})}{M_C} + \frac{2(Z_H - Z_{H,O})}{2M_H} - \frac{2(Z_O - Z_{O,O})}{M_O}}{\frac{2(Z_{C,F} - Z_{C,O})}{M_C} + \frac{(Z_{H,F} - Z_{H,O})}{2M_H} - \frac{2(Z_{O,F} - Z_{O,O})}{M_O}}, \tag{4.2}$$

where Z_i is a conserved scalar given by the total mass fraction of element i, and M_i is the atomic mass mass of element i. Subscripts 'F' and 'O' correspond to the fuel and air

streams, separately. The locations available for the experimental data of the stable case, flame M1, are summarized in Table 4.2. In Table 4.2, x denotes the axial displacement from the nozzle and D notates the diameter of the nozzle, which is equal to 7.2 mm. The experimental data for the other flames are available in [90].

Table 4.2: Available experimental data positions for flame M1 [90]

Flame	Axial locations (x/D)	Radial locations (mm)
M1	20	8, 10, 12
	40	13

Several possible sources of experimental error are reported in [90] and [92]. The possible sources of error include random error from single-point measurement on temperature and species, systematic error during calibration, interference error within the Raman Rayleigh LIF technique, and spatial resolution [90, 92].

4.1.3 Review of Previous Numerical Studies on the Piloted Flame

In this section, a review of previous numerical studies on the piloted methanol flame investigated by Masri *et al.* [88] are presented.

CMC Method

The primary focus of the numerical work by Roomina and Bilger [93] is to predict the conditional mass fractions of species including CO_2, H_2O, CH_3OH, O_2, OH, CO, and H_2, and temperature using the CMC method. In their work, flame M1 and M2 are reproduced using three different chemistry kinetics: GRI-Mech 2.11 [65], SKELETAL [94], and SUB-GRI. For the reference, GRI-Mech 2.11 contains 279 reactions for 49 species including a full set of nitrogen chemistry. The SKELETAL mechanism by Chen *et al.* [94] includes 15 species and 23 reactions, which provides good results in laminar flames of methane [93]. Finally, SUBGRI model is a subset of GRI-Mech 2.11 where the same number of species in SKELETAL mechanism (15 species) are considered with 34 reactions. In SUBGRI, the nitrogen chemistry is excluded.

The CMC investigation uses the standard $k-\epsilon$ model to predict the turbulent flow. The CMC calculations are done with unevenly distributed 68 grid points in the mixture

fraction space. The grid is concentrated on the stoichiometric mixture fraction, $\xi_{st} = 0.135$. In their work, the conditional results for the species mass fractions and temperature are compared with the experimental data [88] at $x/D = 20$ and $x/D = 40$ for flame M1, and $x/D = 40$ for flame M2. However, there is no comparison on the unconditional species mass fractions and temperature in their work.

Roomina and Bilger obtain accurate predictions for flame M1 at the two axial locations. All of the three chemistry mechanisms used in their CMC calculations yield accurate predictions of the conditional temperature and species mass fractions of CO_2, H_2O, O_2, and OH at both axial locations. However, they report that GRI-Mech2.11 and SUBRI models provide a significant overpredictions for H_2 up to 400 %, whereas the mass fraction of H_2 agree well with the experimental data in the SKELETAL case. Meanwhile, the mass fraction of CO from the SKELETAL case is underpredicted in the fuel rich side significantly compared to the cases with GRI-Mech 2.11 and SUBGRI. The more accurate prediction of $\widetilde{Y}_{H_2}$ by the SKELETAL mechanism than GRI-Mech 2.11 is reported to be due to the different reaction rate constants for one of the reactions they share, $CH_3OH + H => CH_2OH + H_2$ [93]; the reaction rate constants of this reaction in GRI-Mech 2.11 are significantly larger than those of the SKELETAL mechanism.

For flame M2, the CMC results using the SKELETAL mechanism are only provided. For this flame, however, the conditional mass fraction of H_2 is overpredicted more than 400% by the SKELETAL mechanism. The predictions of the other species mass fractions and temperature are reasonably accurate compared to the experimental data.

Roomina and Bilger [93] mention that the small discrepancies between the CMC results and the experimental measurements are believed due to large fluctuations about the conditional means. The measured fluctuations about the conditional averages at $x/D = 40$ location are presented in Figure 4.2 to illustrate the significant fluctuations about the conditional averages. The level of fluctuations about the mean at $x/D = 20$ location is similar to those of $x/D = 40$ location. Another main possible source of discrepancy is reported to be the exclusion of differential diffusion effect within their CMC simulation.

In their work, there is no rigorous examination of the mixing field for both M1 and M2 flames. They report that no attempt has been done to tune the turbulence model constants in the $k - \epsilon$ model to capture the accurate predictions of the mixing field.

Transported PDF method

The numerical study performed by Lindstedt and Louloudi [95] simulates flames M1, M2, M3, and M4 using a transported joint probability density function approach. This study focuses on the assessment of the ability of the transported PDF approach to model the de-

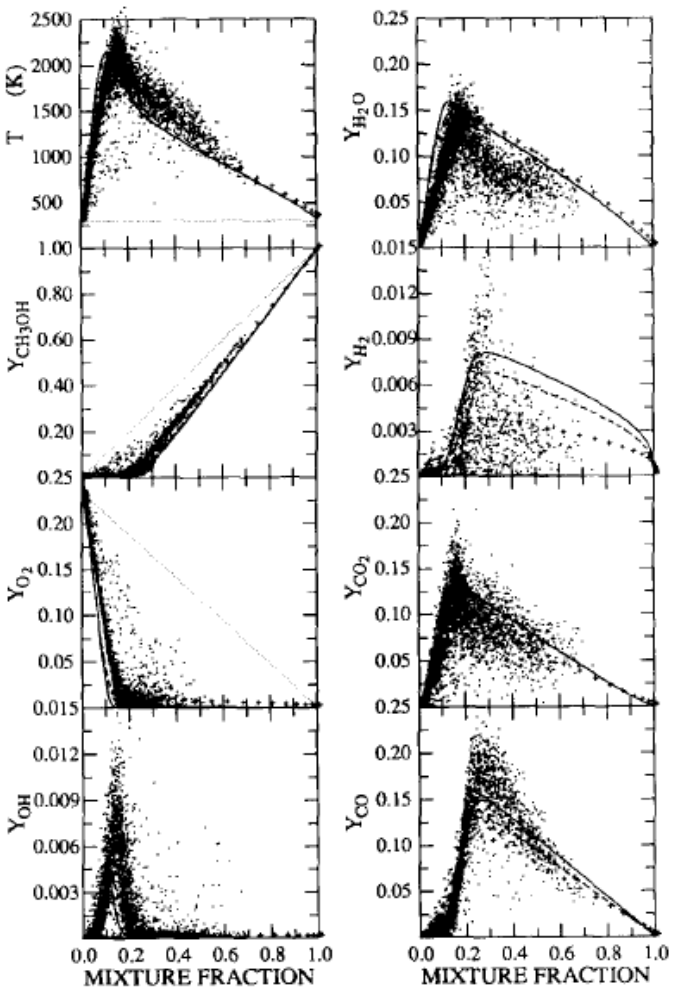

Figure 4.2: Experimental measurements on conditional reactive species mass fractions at $x/D = 40$ for flame M1, reproduced from [88]

tailed chemical structure of flames and phenomena such as flame extinction and re-ignition. The C/H/O chemistry mechanism [96] which has 32 species and 167 reactions is adapted in the numerical study. The conditional temperature and species mass fractions are compared with the experimental data, and the joint PDF results are similar to the experimental data except for H_2, which is significantly overpredicted. Lindstedt and Louloudi manage to predict the local extinction and re-ignition in flame M4 at the reasonable level of accuracy. However, the results of the mixing field as well as the Favre averaged species mass fractions

and temperature are not available in their study.

4.2 Bluff-body Flame

Dally *et al.* [97] investigate the instantaneous and mean compositional structure of the bluff-body stabilized non-premixed methanol flame using the bluff-body burner in the University of Sydney [97]. In this study, the structure of bluff-body stabilized flames are investigated with three different fuels at different main inlet conditions. The examined fuels are pure methanol, H_2/CO mixture, and CH_4/CO mixture. Similar to the experimental study on the piloted flame in Section 4.1, the experimental measurements on the mixing field as well as both the conditional and Favre averaged temperature and species mass fractions are available at several axial locations in [90, 97].

4.2.1 Experimental Method

The bluff-body burner is composed of main jet, bluff-body, and air co-flow. The main jet has the diameter of 3.6 mm. The bluff-body is concentric to the main jet with an outer diameter, D_B, of 50 mm. The face of the bluff-body is coated with a heat-resistant ceramic. Stream of air co-flow is present surrounding the main jet and the bluff-body. The presence of the bluff-body creates flow recirculation zone behind the bluff-body, which acts as a flame holder as well as favors the mixing between the fuel and air. Figure 4.3 illustrates the configuration of the bluff-body burner. The methanol flames are investigated at three different fuel inlet velocities, as displayed in Table 4.3. In the three cases, pure methanol at 373 K enters the burner. The mean velocity of the air is kept at 40 m/s. Similar to the experimental study on the piloted flame in Section 4.1, the Raman/Rayleigh/LIF technique is employed to collect instantaneous and simultaneous temperature and the concentration of many species at a single point in the flame [97]. The boundary conditions and collected experimental data are available at the University of Sydney website [90].

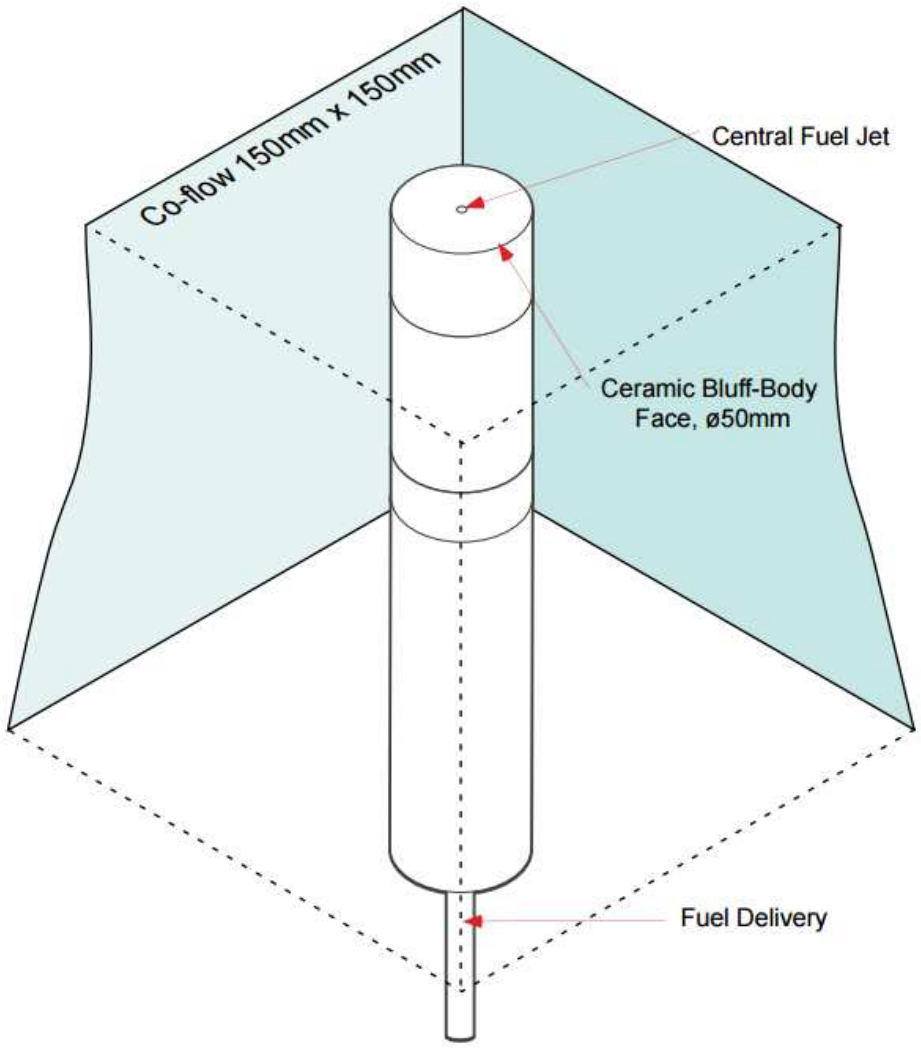

Figure 4.3: Configuration of the bluff-body burner in the University of Sydney, reproduced from [90]

Table 4.3: Summary of conditions for investigated methanol flames [88]

Flame	Mean velocity of the fuel jet (m/s)	Corresponding Re
ML1	80	23,700
ML2	121	35,900
ML3	134	39,700

4.2.2 Experimental Results

Dally *et al*. report that the fuel jet speed for ML1 corresponds to 55 % of the flame blow-off speed. Meanwhile, ML2 and ML3 corresponds to 84 % and 93% of the flame extinction, respectively. The experimental measurements on the Favre averaged mean and variance of the mixture fraction, temperature, and reactive species mass fractions are available in [90] for ML1, ML2, and ML3. The database on the conditional temperature and reactive species mass fractions at the corresponding axial locations are also available in [90] and [97]. The mixture fraction for the conditional averages is calculated using Bilger's formula, which is introduced in Eq. 4.2. Table 4.4 provides the location of the available experimental measurements for flame ML1. In Table 4.4, x represents the axial displacement from the main nozzle and D_B is the diameter of the bluff-body, which is equal to 50 mm. The radial location 0 corresponds to the centre of the main nozzle.

Table 4.4: Available experimental data positions for flame ML1 [90]

Flame	Axial locations (x/D_B)	Radial locations (mm)
ML1	0.26	0 to 26
	0.6	0 to 26
	0.9	0 to 26
	1.3	0 to 24
	4.5	0 to 24
	9.0	0 to 27
	13.5	0 to 30

The reported possible sources of experimental uncertainties in the bluff-body case are

similar to the piloted flame in Section 4.1.2 [92]. For the estimate of error associated to the precision of single-point measurements of species, Dally *et al.* provide the sample estimates from methane/hydrogen flame [97].

4.2.3 Review of Previous Numerical Study

Kim *et al.* [98] simulate flame M1 using the CMC method. The corrected standard $k-\epsilon$ model by Morse [99] yields a reasonable prediction for the mixing field. In their work, the detailed chemical reaction mechanism for methanol by Peters [100], which involves 33 reactions with 15 species, is used for the chemistry. The detailed mechanism by Peters is shown in Table 4.5. In Table 4.5, **A** denotes the the pre-exponential factor, **b** is the temperature exponent, and **E** represents the activation energy. The units are in KJ, mol, K, cm, and s. In their work, the number of grid points in mixture fraction space is set to 40, concentrated around the stoichiometric mixture fraction [98]. The CMC results for both unconditional and conditional species mass fractions including CH_3OH, O_2, CO_2, H_2O, CO, H_2, and OH as well as temperature are examined at $x/D_B = 0.9$, $x/D_B = 1.3$, $x/D_B = 1.8$, and $x/D_B = 4.5$. In general, the results agree well with the experimental data except for OH, CO, and H_2. Kim *et al.* mention that the exclusion of differential diffusion effect in their work could have impacted the discrepancy in their results [98].

Table 4.5: Detailed methanol chemistry by Peters [100]

No.	**Reaction**	**A**	**b**	**E**
1.	$CH_3OH + H \rightarrow CH_2OH + H_2$	4.00E + 13	0.0	25.5
2.	$CH_3OH + OH \rightarrow CH_2OH + H_2O$	1.00E + 13	0.0	7.1
3.	$CH_3OH + O \rightarrow CH_2OH + OH$	1.00E + 13	0.0	19.6
4f.	$CH_3OH + HO_2 \rightarrow CH_2OH + H_2O_2$	6.20E + 12	0.0	81.1
4b.	$CH_2OH + H_2O_2 \rightarrow CH_3OH + HO_2$	1.00E + 7	1.7	47.9
5.	$CH_2OH + H \rightarrow CH_2O + H_2$	3.00E + 13	0.0	0.0
6.	$CH_2OH + O_2 \rightarrow CH_2O + HO_2$	1.00E + 13	0.0	30.1
7.	$CH_2OH + M \rightarrow CH_2O + H + M$	1.00E + 14	0.0	105.1
8.	$CH_2O + H \rightarrow HCO + H_2$	2.50E + 13	0.0	16.7
9.	$CH_2O + O \rightarrow HCO + OH$	3.50E + 13	0.0	14.6
10.	$CH_2O + OH \rightarrow HCO + H_2O$	3.00E + 13	0.0	5.0
11.	$CH_2O + M \rightarrow HCO + H + M$	1.40E + 17	0.0	320.0
12f.	$O_2 + H \rightarrow OH + O$	2.00E + 14	0.0	70.3

Table 4.5 – continue

No.	Reaction	A	b	E
12b.	$OH + O \rightarrow O_2 + H$	1.57E + 13	0.0	3.52
13f.	$H_2 + O \rightarrow OH + H$	5.06E + 04	2.7	26.3
13b.	$OH + H \rightarrow H_2 + O$	2.22E + 02	2.7	18.29
14f.	$H_2 + OH \rightarrow H_2O + H$	1.00E + 08	1.6	13.8
14b.	$H_2O + H \rightarrow H_2 + OH$	4.31E + 08	1.6	76.46
15f.	$OH + OH \rightarrow H_2O + O$	1.50E + 09	1.1	0.42
15b.	$H_2O + O \rightarrow OH + OH$	1.47E + 10	1.1	71.09
16f.	$O_2 + H + M \rightarrow HO_2 + M$	2.30E + 18	-0.8	0.0
16b.	$HO_2 + M \rightarrow O_2 + H + M$	3.19E + 18	-0.8	195.39
17.	$HO_2 + H \rightarrow OH + OH$	1.50E + 14	0.0	4.2
18.	$HO_2 + H \rightarrow H_2 + O_2$	2.50E + 13	0.0	2.9
19.	$HO_2 + OH \rightarrow H_2O + O_2$	6.00E + 13	0.0	0.0
20.	$HO_2 + H \rightarrow H_2O + O$	3.00E + 13	0.0	7.2
21.	$HO_2 + O \rightarrow OH + O_2$	1.80E + 13	0.0	-1.7
22.	$HO_2 + HO_2 \rightarrow H_2O_2 + O_2$	2.50E + 13	0.0	-5.2
23f.	$OH + OH + M \rightarrow H_2O_2 + M$	3.25E + 22	-2.0	0.0
23b.	$H_2O_2 + M \rightarrow OH + OH + M$	1.69E + 24	-2.0	202.29
24.	$H_2O_2 + H \rightarrow H_2O + OH$	1.00E + 13	0.0	15.0
25f.	$H_2O_2 + OH \rightarrow H_2O + HO_2$	5.40E + 12	0.0	4.20
25b.	$H_2O + HO_2 \rightarrow H_2O_2 + OH$	1.80E + 13	0.0	134.75
26.	$H + H \rightarrow H_2 + M$	1.80E + 18	-1.0	0.0
27.	$OH + H \rightarrow H_2O + M$	2.20E + 22	-2.0	0.0
28.	$O + O \rightarrow O_2 + M$	2.90E + 17	-1.0	0.0
29f.	$CO + OH \rightarrow CO_2 + H$	4.40E + 06	1.5	-3.1
29b.	$CO_2 + H \rightarrow CO + OH$	4.96E + 08	1.5	89.76
30.	$HCO + H \rightarrow CO + H_2$	2.00E + 14	0.0	0.0
31.	$HCO + OH \rightarrow CO + H_2O$	1.00E + 14	0.0	0.0
32.	$HCO + O_2 \rightarrow CO + HO_2$	3.00E + 12	0.0	0.0
33f.	$HCO + M \rightarrow CO + H + M$	7.00E + 14	0.0	70.3
33b.	$CO + H \rightarrow HCO + M$	1.14E + 15	0.0	9.97

4.3 Summary

In this chapter, the previous experimental and numerical studies used as a basis for the current study are provided. Two types of turbulent non-premixed methanol flames are introduced in this chapter: piloted flame and bluff-body flame. Starting from the description of the experimental set-up, the experimental results, and previous numerical investigations of the corresponding experimental flame are provided in this chapter.

The following two chapters provide the CSE calculations on the two methanol flames, and the results are compared with the experimental data and the previously simulated results. Chapter 5 corresponds to the piloted flame calculations, and the bluff-body calculations are covered in Chapter 6.

Chapter 5

Non-premixed Piloted Methanol Flame CSE Calculations

This chapter provides an analysis of the current CSE method with the non-premixed piloted methanol flame. The experimental conditions and numerical set-ups for the chosen flame is described, followed by the results obtained using the current CSE method. The CSE results of the conditional and unconditional species mass fractions and temperatures are presented. The CSE results are compared with both the experimental data [88] and the previously CMC simulated results [93].

5.1 Experimental Study Description

The present study focuses on flame M1, which is reported to be the only stable case and far from blow-off among the five cases illustrated in Section 4.1 [88]. The experimental conditions for flame M1 are summarized in Table 5.1.

Table 5.1: Summary of flame condition M1 [88]

Jet diameter, D (mm)	7.2
Reynolds number of the jet, Re_{jet}	39,200
Mean velocity of jet (m/s)	66.2
Mean velocity of pilot gas (m/s)	21
Mean velocity of co-flow (m/s)	15
Stoichiometric mixture fraction, η_{st}	0.135

5.2 Computational Set-up

This section provides the details of the computational set-up used for the modelling of flame M1 based on the experimental condition. The simulation details are configured to match the experimental condition as closely as possible. The computational grid, boundary, and initial conditions are described.

5.2.1 Computational Domain, Boundary Conditions, and Initial Conditions

The computational domain, boundary conditions, and initial conditions are established to replicate the experimental condition as closely as possible with the known conditions. The domain is created as a wedge of small degree ($\theta = 10°$) with one cell in the θ direction, meaning that the simulation is conducted in two dimensional space. The domain is 1.4 m long in the axial direction (x), which is about 1.4 times longer than the reported visible flame length [88]. The radius of the domain is set to 0.15 m. At the base of the domain, the fuel jet inlet extends over a radial distance (r) of 3.6 mm starting from the centreline. Starting from $r = 3.6$ mm to $r = 9$ mm, the inlet for the hot pilot gas is present at the base of the domain. The inlet for air co-flow covers the rest of the radial width. An outlet is placed along the top boundary far downstream of the flame length which allows fluid to flow out of the domain without restriction. The side boundary is also set as outlet and specified as an opening for fluid moving out of the domain.

The experimental measurements on the mean velocity and its root-mean-square (rms) fluctuation are implemented for the boundary conditions at the inlets as shown in Fig. 5.1.

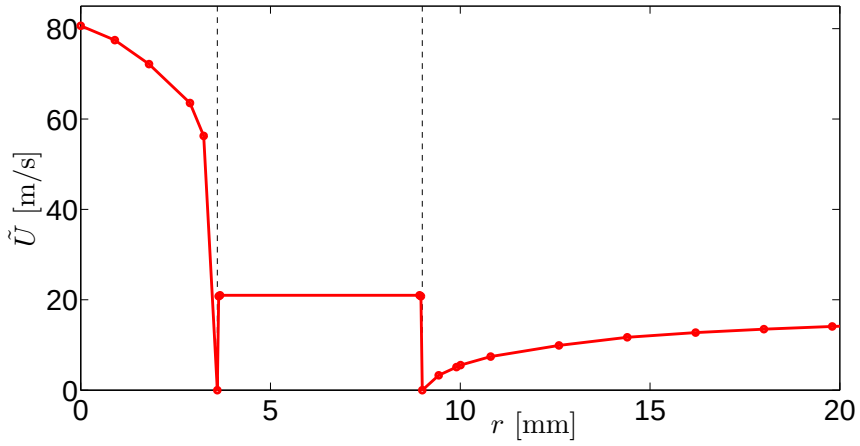

(a) Mean velocity

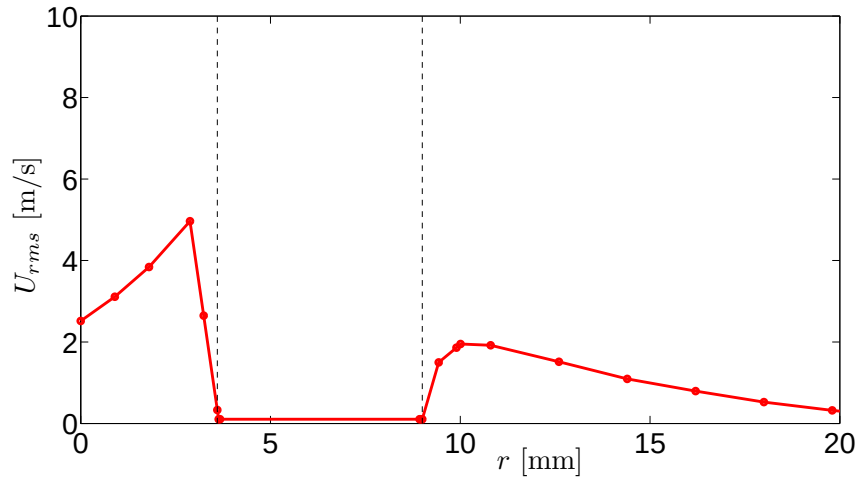

(b) RMS fluctuation of mean velocity

Figure 5.1: Experimental measurements on velocity profile at inlets

The composition of the hot pilot gas is specified as $Y_{CO_2} = 0.165$, $Y_{H_2O} = 0.241$, and $Y_{N_2} = 0.594$ based on its chemical composition from Eq. 4.1. The composition of the air co-flow is set to $Y_{O_2} = 0.233$ and $Y_{N_2} = 0.677$. The temperature at the fuel inlet is set to 373 K, 2327 K for the pilot gas, and 300 K at the air co-flow. For all the inlets, the atmospheric pressure condition is imposed. The computational domain is discretized into 85 cells and 300 cells in the axial and radial direction, respectively. The grid is non-

uniform with a high concentration of nodes in the region where the flame is expected to be developed: near the main jet. Away from the flame development region, the grid is less dense in both axial and radial directions. The distribution of the spatial grid in the radial direction is summarized in Table 5.2. The mesh is 1 cell thick along the plane of symmetry, implying that the simulation is conducted in two dimensional space.

Table 5.2: Radial distribution of spatial mesh

Range (mm)	Corresponding inlet	Number of Cells
$0 - 3.6$	Fuel	6
$3.6 - 9$	Pilot	9
$9 - 150$	Air co-flow	70

The computational domain with mesh is displayed in Fig. 5.2.

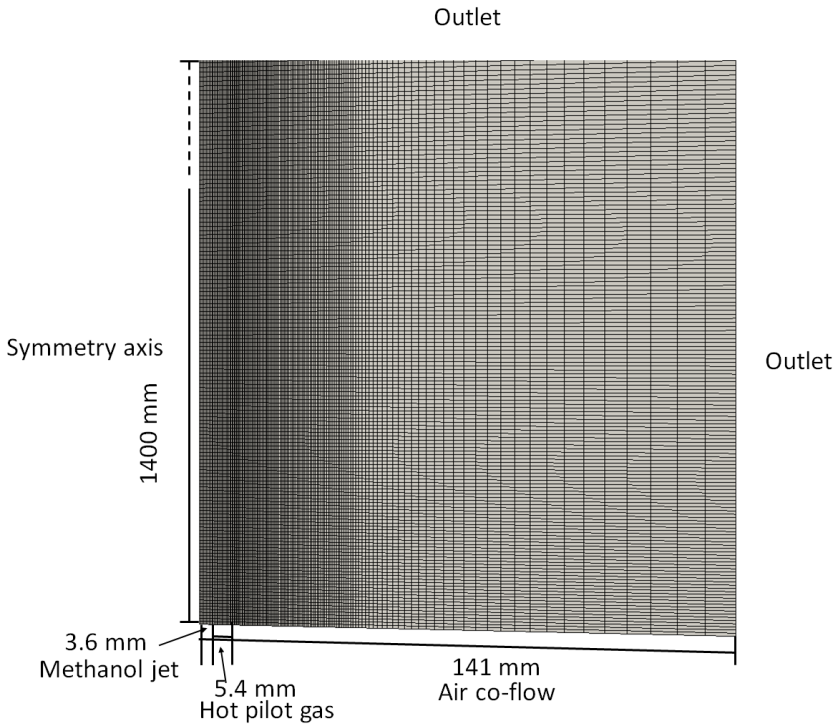

Figure 5.2: Computational mesh for the piloted flame

5.2.2 CSE Set-up

The mixture fraction sample space is discretized into 70 nodes with highly concentrated between the values of 0.07 and 0.37, which are the Lower Flammability Limit (LFL) and Upper Flammability Limit (UFL) of pure methanol, respectively [89]. The distribution of nodes is shown in Fig. 5.3.

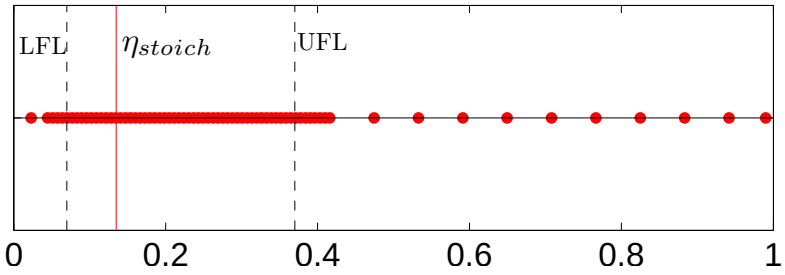

Figure 5.3: Distribution of sampling mixture fraction grid η

The discretized governing equations including conservation of mass, momentum, and enthalpy are solved for each cell. In addition, the PDF of mixture fraction is obtained for each cell. The current implementation of CSE is explained in Section 3.5. In the present study, CSE is implemented in a way that the transport equations of species CO_2 and H_2O only are solved, whereas the mass fraction from TGLDM tables are integrated and used as the species mass fractions at given computational cell for the remaining species including CH_3OH, O_2, OH, CO, and H_2. Thus, for CO_2 and H_2O, the chemical source terms are obtained based on their conditional source-term using the principle of CSE . The conditional reaction rates of these two species are then used to calculate their unconditional counterparts by solving Eq. 3.14. The unconditional reaction rates of the species are used to solve Eq. 3.15 in the CFD module. Meanwhile, Eq. 3.16 is used to solve for the species mass fraction of CH_3OH, O_2, OH, CO, and H_2 since their mass fractions are determined directly from the TGLDM tables. The mass fraction of N_2 is determined by subtracting sum of all the species from unity. The constant molecular diffusivity of all the species is assumed as well as the mixing of the species are considered to be described by the mixture fraction only.

5.2.3 Turbulence Model

The turbulent flow field is solved using the standard $k-\epsilon$ approach, which is described in Section 2.4. It has been observed that the standard values in the model provide huge overprediction of radial spreading rate. In the present study, several values of C_{ϵ_1} in Eq. 2.42 are tested to find the value that produces the most accurate mixing field compared to the experimental Favre averaged mixture fraction. The sensitivity analysis of C_{ϵ_1} is presented in Section 5.3.2.

5.2.4 Chemistry

The chemistry mechanism employed in the current CSE study is GRI-Mech2.11, which includes 49 species and 277 reactions [65]. The TGLDM chemistry tables are generated following Eq. 3.9 using a stiff ODE system solver. The number of mixture fraction grid selected in the present work is 70, therefore, total 70 chemistry tables are made prior to the simulation.

5.2.5 Radiative Heat Loss

The radiation loss due to the reactive species is taken account using RADCAL method with consideration of heat loss due to CO_2 and H_2O only. In RADCAL, the Planck coefficients of species, $a_{p,k}$ is determined using curve fitting and the curve fitting parameters for CO_2 and H_2O are obtained from the Sandia website (http://www.sandia.gov/TNF/radiation.html). Using the parameters, the heat loss due to radiation, Q_R, can be calculated by

$$Q_R = 4\sigma(\sum_{n_r}^{1} p_k a_{p,k})(T^4 - T_\infty^4), \tag{5.1}$$

where σ is the Stefan-Boltzmann constant, p_k is the partial pressure of the specie k, T is the local flame temperature, and T_∞ is the surrounding temperature.

5.3 Sensitivity Analysis

In order to minimize error and uncertainty in the numerical investigation, it is very important to examine the sensitivity of modelling parameters. In this section, the effect of varying the spatial grid, $C_{\epsilon 1}$ of the standard $k-\epsilon$ model, and the size of CSE ensembles are discussed.

5.3.1 Spatial Grid Sensitivity

The grid independence of the calculations are tested by examining three grid resolutions summarized in Table 5.3.

Table 5.3: Radial distribution of spatial mesh

Grid	Radial range (mm)	Number of cells (radial)	Number of cells (axial)
1	$0-3.6$	3	200
	$3.6-9$	4	
	$9-150$	54	
2	$0-3.6$	6	300
	$3.6-9$	9	
	$9-150$	70	
3	$0-3.6$	9	400
	$3.6-9$	15	
	$9-150$	115	

As shown in Table 5.3, Grid 3 has the highest number of cells while Grid 1 has the lowest. For the three different grids, the distribution factor in radial direction is kept the same. In order to check the grid independency of the current grid (Grid 2 in Table 5.3), the axial profile of the mean mixture fraction at the centreline, and radial profiles of the mean mixture fraction at $x/D = 20$ and $x/D = 40$ are examined. The axial locations of the sampling positions are shown in Fig. 5.4 mapped with the temperature contour of the simulated flame. Notice that Fig. 5.4 is obtained from the Grid 2 case and the figure does not show the entire flame.

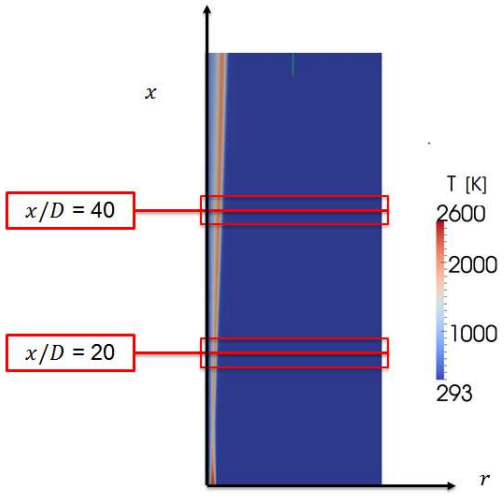

Figure 5.4: Temperature contour of the piloted flame from the CSE simulation with the indication of the examined axial locations

Figure 5.5 shows the radial profiles of mean mixture fraction predicted by the three spatial grids at the $x/D = 20$ location. As shown in Fig. 5.5, the difference between the results of Grid 2 and Grid 3 are small, less than 1 %. Similar observation can be made for the axial profile at the centreline and the radial profile at $x/D = 40$. Therefore, Grid 2 is selected for performing subsequent investigations.

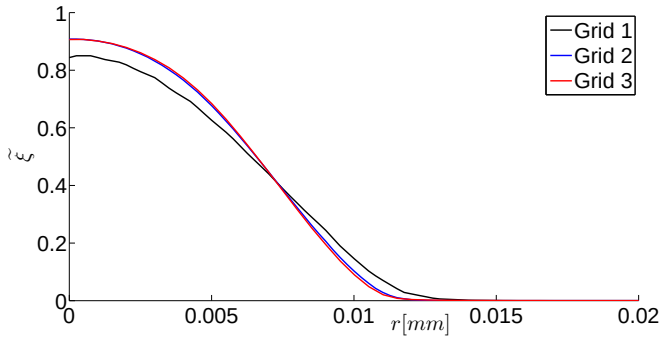

Figure 5.5: Radial profile of the mean mixture fraction with three different spatial grid at $x/D = 20$

5.3.2 C_{ϵ_1} Sensitivity

A range of $C_{\epsilon 1}$ values from 1.44 to 1.7 are tested, and the radial profiles of the mean mixture fraction predicted by CSE simulations at $x/D = 20$ and $x/D = 40$ are compared with the experimental data [90]. Figure 5.6 illustrates the results compared with the experimental data at $x/D = 20$. Increasing the value of $C_{\epsilon 1}$ reduces the overprediction of the mean mixture fraction in the region between $r = 8$ mm and $r = 12$ mm. For the case with $C_{\epsilon 1} = 1.44$, the mean mixture fraction is overpredicted by more than 200 % compared to the experimental data at the three radial locations. The overprediction by the simulation is reduced as the value of $C_{\epsilon 1}$ increases, in fact, the case with $C_{\epsilon 1} = 1.7$ reproduces the mixing field similar to the experimental data. The radial profile of the mean mixture fraction at $x/D = 40$ is also examined, and still the case with $C_{\epsilon 1} = 1.7$ provides the best agreement with the experimental data. Thus, the value of 1.7 for $C_{\epsilon 1}$ is kept and the following results of species mass fractions and temperature are shown with this case.

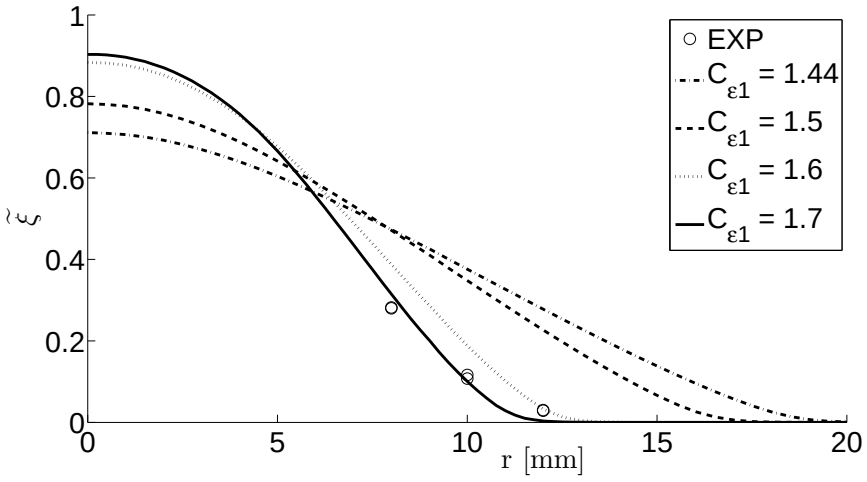

Figure 5.6: Radial profile of mean mixture fraction predicted by different $C_{\epsilon 1}$ values at $x/D = 20$ compared with the experimental data [90]

5.3.3 Size of CSE Ensemble Sensitivity

The conditional averages are assumed to be homogeneous for a given ensemble of points, as described in Section 3.2. Using this assumption, the computational grid may be divided into subdomains to represent these ensembles. The size of CSE ensembles may have an

impact on the final species and temperature predictions. Thus, a sensitivity analysis of the size of CSE ensemble is performed by reducing the size of the ensembles until no significant change in the Favre averaged species mass fractions and temperature are observed.

Four different sizes are investigated including 120 mm, 80 mm, 40 mm, and 20 mm in the flow direction, covering the entire radial distance with a slight overlap between each ensemble. The Favre averaged temperature profiles are examined in the present paper, but similar conclusions would be reached using the Favre averaged species mass fractions. The predicted radial profiles of Favre averaged temperature by the four different sizes of CSE ensembles are presented in Fig. 5.7. As can be seen in Fig. 5.7, the predictions converge to a single temperature profile as the size of CSE ensembles is reduced. The deviation between the case with 20 mm and 120 mm is significant. The peak temperature from the case with 120 mm is around 1700 K, while the cases with 80 mm, 40 mm, and 20 mm reach up to 2000 K. After reducing the size of CSE ensemble from 40 mm to 20 mm, a very slight difference is observed (within 1 %). Thus, the CSE ensemble with the size of 40 mm in the axial direction is kept for performing subsequent calculations.

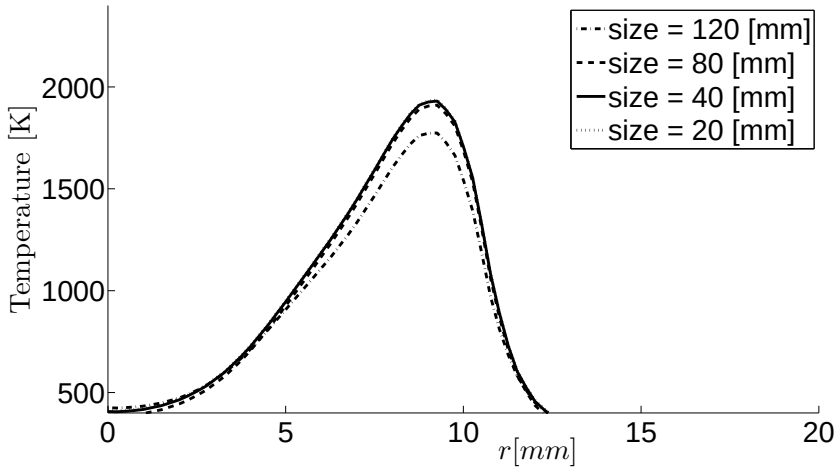

Figure 5.7: Radial profile of Favre-averaged temperature at $x/D = 20$ with different sizes of CSE ensemble

5.4 Conditional Species Mass Fractions and Temperature

Figure 5.8 shows the conditional species mass fractions of CO_2, H_2O, O_2 , CO , H_2, CH_3OH and temperature at the $x/D = 20$ location compared with the experimental data [88, 90] and the previously simulated results using the CMC approach [93]. It should be reminded that, in the current CSE-TGLDM approach, the conditional mass fractions of CO_2 and H_2O are directly obtained from the inversion process, and the conditional mass fractions of the remaining species and conditional temperature are retrieved from the TGLDM tables. As can be seen in Fig. 5.8(a), the conditional mass fractions of CO_2 are well predicted by the current CSE calculations, in close agreement with the experimental data. This demonstrates that the regularization technique works well and provides accurate results. There is a slight overprediction when compared to the experimental values, on the order of 10 % at most. In the CSE results, the peak of $\langle Y_{CO_2}|\eta\rangle$ occurs around $\eta = 0.135$, which is the stoichiometric mixture fraction value, consistent with what would be expected. In the region between $\eta = 0.2$ and $\eta = 0.36$, CSE is able to reproduce the sharp gradient displayed by $\langle Y_{CO_2}|\eta\rangle$ profile, which is not observed in the CMC predictions. This improvement may be due to the fact the CMC equations are radially averaged and only solved in the axial direction, whereas in CSE, the transport equation for CO_2 is solved in two physical dimensions. Otherwise, the two profiles obtained by CSE and CMC are very close. As shown in Fig. 5.8 (b), it is interesting to note that the conditional mass fractions of H_2O are well predicted for lean mixtures, but for mixtures around stoichiometry and richer than stoichiometry, $\langle Y_{H_2O}|\eta\rangle$ are significantly overpredicted by up to 40% when compared to the experiments, and this large overprediction is also observed in the CMC results using a different method to obtain the conditional averages. Thus, this similarity in the CSE and CMC predictions points towards sources of discrepancies common to both approaches like chemistry, differential diffusion and neglect of the conditional fluctuations. These will be discussed further in the light of the additional predictions and comparison with the experimental data.

As can be seen in Figs. 5.8 (c) and (d), the predicted conditional mass fractions of O_2 and OH are in good agreement with the experimental data, for shape and magnitude, with differences smaller than 7%. Again, the CSE and CMC profiles are close to each other.

For clarity, Figs. 5.8 (e) - (h) only include the region between $\eta \simeq 0.07$ and $\eta \simeq 0.39$, corresponding to the upper flammability limit of pure methanol [89]. As can be seen in Fig. 5.8 (e), the conditional mass fractions of CO obtained from CSE are comparable to those found in CMC between $0 < \eta \leq 0.25$ and slightly underpredict the experimental data by 10-15%. The CSE profile displays a CO mass fraction peak at $\eta \simeq 0.3$, which is slightly

beyond the location of the peak in the experiments ($\eta \simeq 0.27$). The CSE predictions remain larger than the experimental values until $\eta \simeq 0.33$, then become lower than the experimental data.

The largest discrepancies in the numerical results with the experimental values are seen in the profiles of $\langle Y_{H_2}|\eta\rangle$ in Fig. 5.8 (f). Both CMC and CSE significantly overpredict the experimental data for H_2, in particular for fuel rich mixtures. As shown in Fig. 5.8 (g), the agreement between the CSE methanol concentration predictions and the experimental measurements is very good for fuel lean mixtures for $\eta < 0.15$. However, for $\eta \geq 0.15$, the methanol mass fractions are significantly underpredicted by CSE and CMC. As can be seen in Fig. 5.8 (h), CSE slightly overpredicts the experimental temperatures between $\eta \simeq 0.05$ and $\eta \simeq 0.1$, and the predicted temperature peak is located close to the stoichiometric mixture fraction, whereas the experimental profile shows a peak slightly on the rich side of stoichiometry. CSE and CMC temperature predictions are comparable with the experimental data, while CSE predictions are slightly closer to the experimental values than those predicted by CMC.

The conditional mass fractions of species and temperature at x/D = 40 are shown in Fig. 5.9 . The results at this location share many similarities with those displayed at $x/D = 20$ in Fig. 5.8. Good agreement is found for the conditional averages for fuel lean side. The largest discrepancies with the experimental data are observed for the fuel rich side, in particular for CO_2, H_2O, CO, H_2, and CH_3OH.

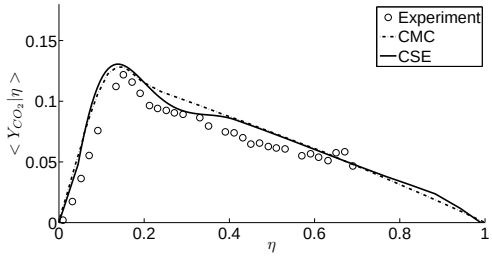

(a) Conditional mass fraction of CO_2

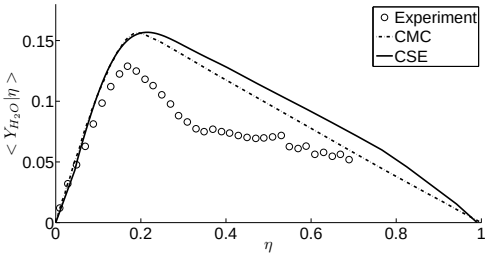

(b) Conditional mass fraction of H_2O

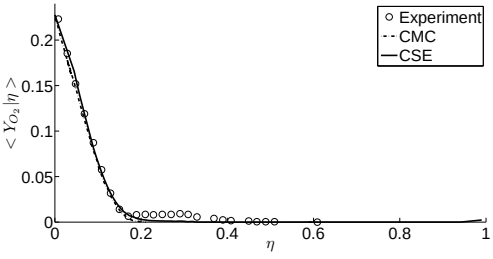

(c) Conditional mass fraction of O_2

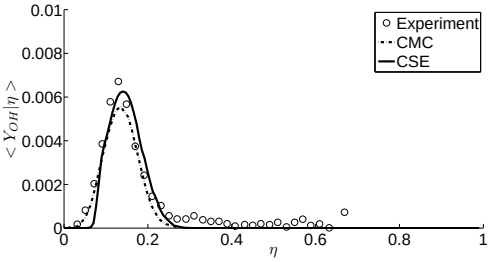

(d) Conditional mass fraction of OH

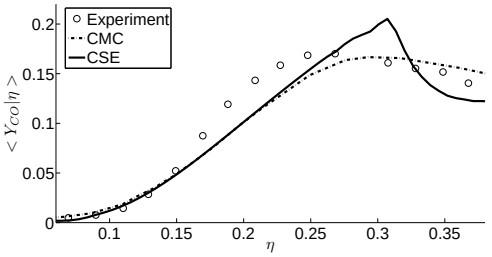

(e) Conditional mass fraction of CO

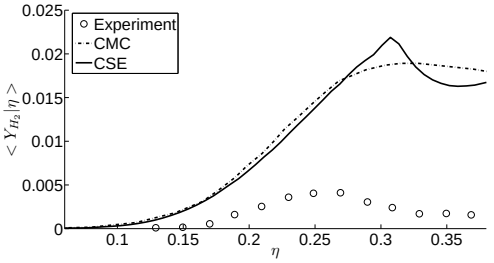

(f) Conditional mass fraction of H_2

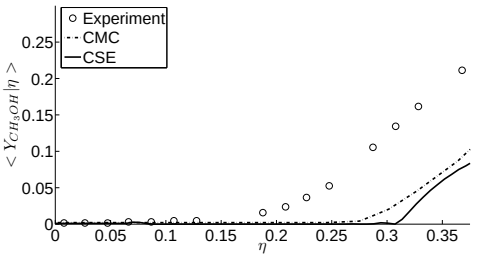

(g) Conditional mass fraction of CH_3OH

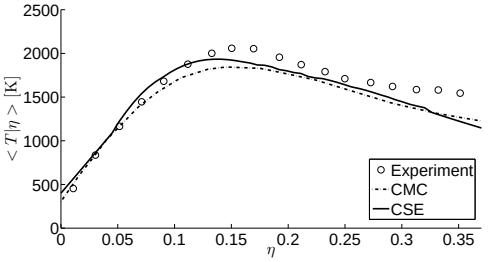

(h) Conditional temperature

Figure 5.8: Conditional species mass fractions and temperature at $x/D = 20$ predicted by CSE compared with experimental data [88, 90] and previous simulation with CMC approach [93]

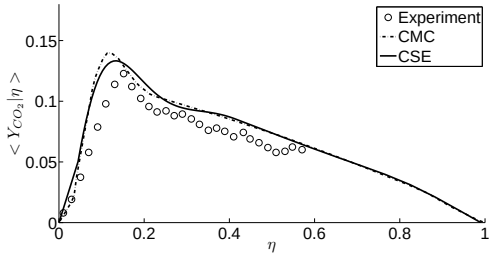

(a) Conditional mass fraction of CO_2

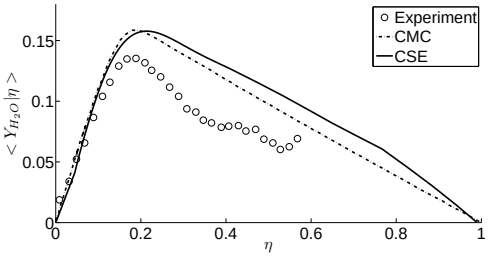

(b) Conditional mass fraction of H_2O

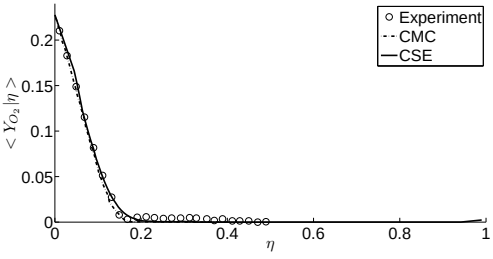

(c) Conditional mass fraction of O_2

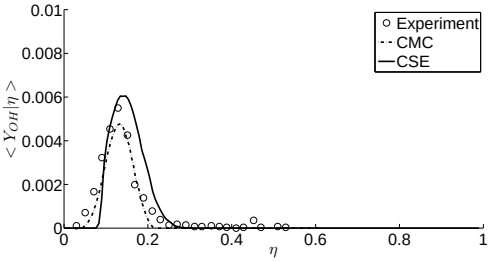

(d) Conditional mass fraction of OH

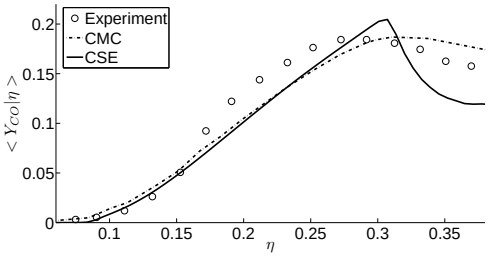

(e) Conditional mass fraction of CO

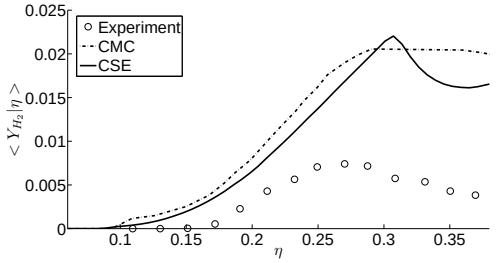

(f) Conditional mass fraction of H_2

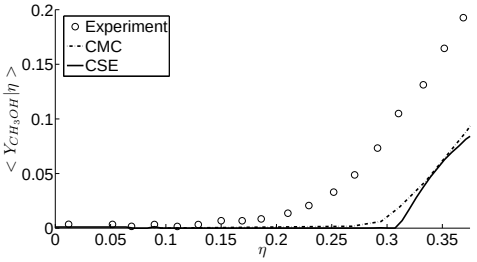

(g) Conditional mass fraction of CH_3OH

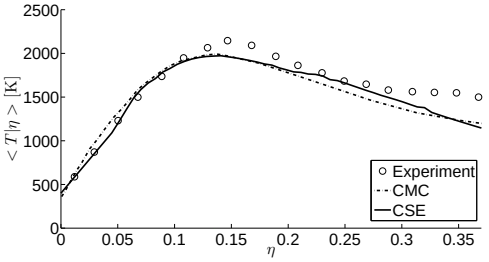

(h) Conditional temperature

Figure 5.9: Conditional species mass fractions and temperature at $x/D = 40$ predicted by CSE compared with experimental data [88, 90] and previous simulation with CMC approach [93]

The predicted conditional averages obtained in the present CSE simulations are close to the predictions reported by Roomina and Bilger in their CMC work [93]. The small differences between the CSE and CMC values are believed to be due to the different methods of obtaining the conditional averages in CSE and CMC. Further, CSE is implemented in two physical dimensions, whereas the CMC equations are cross-stream averaged and solved in one physical dimension. The small differences between the predictions by CSE and CMC on the conditional mass fraction of CO_2 and H_2O are observed for mixture fraction values greater than 0.2 (see Figs. 5.8 (a) and (b), Figs. 5.9 (a) and (b)), and this leads to small deviations in conditional mass fractions of the remaining species and temperature. For example, CSE overpredicts the conditional mass fraction of H_2O slightly higher than the CMC results in the fuel rich side, which causes the additional underprediction of the mass fraction of methanol. Since more products are formed in the fuel rich side, more reactants are consumed.

5.5 Unconditional Species Mass Fractions and Temperature

The experimental data is collected at three different radial locations at $x/D = 20$, while only one location at $x/D = 40$ [88, 90]. Consequently, only the radial profiles at $x/D = 20$ are shown due to the lack of available experimental data at x/D = 40, as can be seen in Fig. 5.10. Overall, CSE predicts the general trends of the experimental data well and the predictions are consistent with what is observed in the profiles for the conditional scalars, as can be seen in Fig. 5.10. For the mass fraction of H_2 illustrated in Fig. 5.10 (f), the discrepancy between the experimental data and the CSE predictions is large corresponding to what is seen in the conditional profile, as shown in Fig. 5.8 (f). At the given three radial positions from the experiment, the relative difference between the experimental values and the CSE results for temperature is smaller than 20% as can been seen Fig. 5.10 (h).

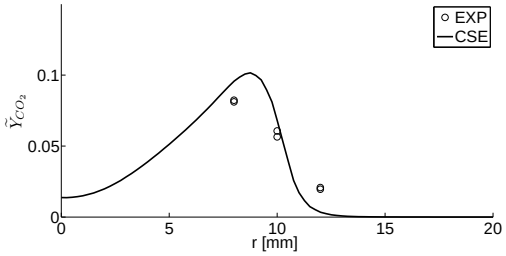

(a) Favre averaged mass fraction of CO_2

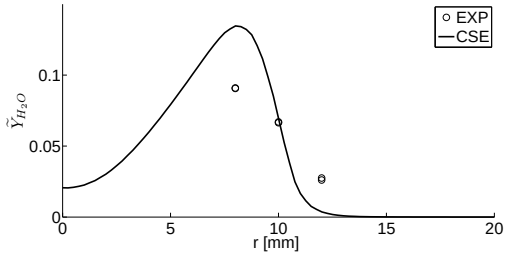

(b) Favre averaged mass fraction of H_2O

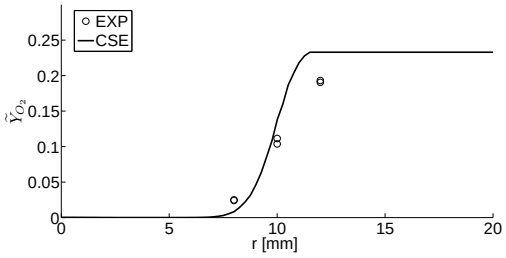

(c) Favre averaged mass fraction of O_2

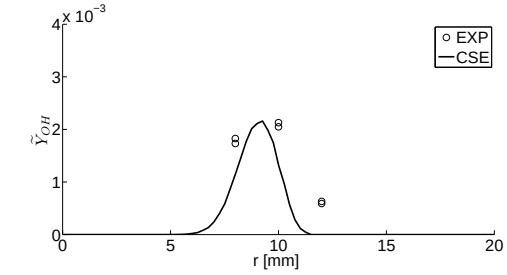

(d) Favre averaged mass fraction of OH

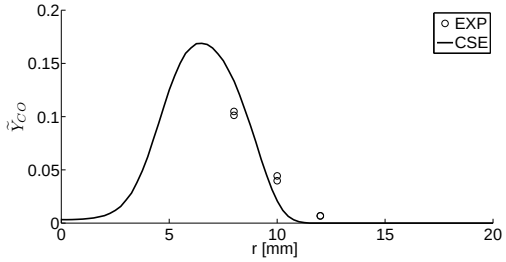

(e) Favre averaged mass fraction of CO

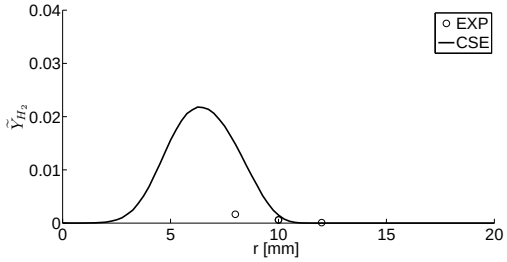

(f) Favre averaged mass fraction of H_2

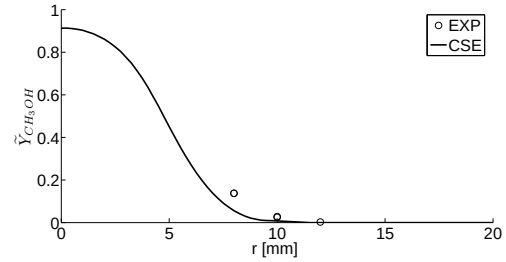

(g) Favre averaged mass fraction of CH_3OH

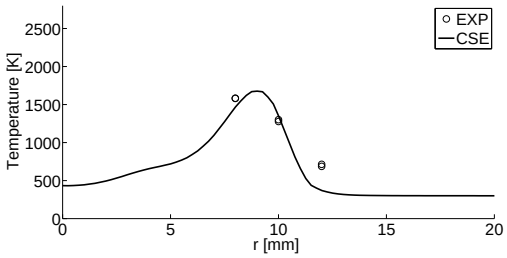

(h) Favre averaged temperature

Figure 5.10: Radial profile of unconditional species mass fractions of CO_2, H_2O, O_2, and H_2 predicted by the CSE compared with the experimental data [90] at $x/D = 20$

Several sources may be identified to explain the discrepancies between the CSE predictions and the experimental data. In CSE, the differential diffusion is neglected assuming constant and equal molecular diffusivity for all species. The fact that the largest discrepancies are observed for H_2 and H_2O (on the rich side) strongly suggest that differential diffusion is an important parameter for more accurate predictions of these species. This is also supported with what is observed in laminar methanol flame calculations. For example, in flamelet profiles, the peak of H_2 mass fraction for equal diffusivity is found to be twice as large as the peak value when differential diffusion is included [97]. In this work, the impact of differential diffusion is found to be much smaller for the other species such as CO and OH. Similar results are illustrated in the study of Roomina and Bilger for the same turbulent methanol flame [93]. Differential diffusion has never been considered in the context of CSE. Several modifications would be expected in the CSE formulation. The chemistry tables would have to reconfigured to include the species diffusion coefficients. In the present formulation, this cannot be done easily as no species diffusion is considered in the species transport equations. The transport equation of mixture fraction may also include a source term to represent the effect of differential diffusion. All these modifications are not beyond reach, but need further thought and care for best implementation. Differential diffusion has been implemented in RANS-CMC with some success but significant complexity is added [101].

Another possible source of discrepancy between the CSE predictions and the experimental data is the chemistry mechanism used in the simulation. In the previous CMC study of the same piloted flame [93], different chemical mechanisms are tested and reaction rate constants for one of the reactions in GRI-Mech 2.11, $CH_3OH + H => CH_2OH + H_2$, are found to be significantly larger compared to the kinetics developed by Chen [94] that shows much better agreement for H_2 and CH_3OH concentrations with the experimental values.

Other factors may have an impact on the quality of the present calculations. Due to limited number of experimental data for the mean mixture fraction and unconditional means across the flame, only detailed comparisons with the experimental data could be undertaken at one axial location. Thus, there may be some inaccuracies in the predicted turbulent flow and mixing fields which will affect the PDF and in turn, the inversion process. The flame selected is shown to have low levels of extinction [88] and the level of rms fluctuation in the conditional data is on the same order of magnitude as the estimated experimental error [88, 90], approximately 10-15%. At this stage, it is not possible to clearly establish the significance of the conditional fluctuation.

5.6 Summary

This chapter describes the numerical investigation of a turbulent non-premixed piloted methanol flame using CSE. The conditional and unconditional reactive species mass fractions and temperatures are examined to evaluate the performance of CSE to simulate non-premixed methanol flame. Based on the investigation, the current CSE implementation with the TGLDM tabulated chemistry may be applicable to reproduce the non-premixed methanol flame. Some discrepancies between the CSE results and the experimental are suspected to be due to the chosen chemistry mechanism and exclusion of the differential diffusion effect within the simulation. At this stage, it is not possible to evaluate the level of accuracy of the model in terms of predicting the Favre averaged results due to the lack of experimental data on these quantities.

Chapter 6

Non-premixed Turbulent Methanol Bluff-Body Flame CSE Calculations

The focus of this chapter is to provide an analysis of the current CSE method with non-premixed bluff-body methanol flame. Starting from the information of the experimental and numerical set-ups for the selected flame, the results obtained using the current CSE method are provided. Similar to what has been done for Chapter 5, the CSE results for the conditional and unconditional species mass fractions and temperature are compared with the experimental data and the previously simulated results using CMC.

6.1 Experimental Study Description

The present investigation on the bluff-body flame focuses on flame ML1, which is reported to be the condition far from extinction described in Section 4.2.2. The experimental condition for flame ML1 is summarized in Table 6.1.

Table 6.1: Summary of flame condition ML1 [90]

Jet diameter, D_j (mm)	3.6
Bluff-body outer diameter, D_B (mm)	50
Mean Jet velocity (m/s)	80
Re_{jet}	23700
Mean Coflow velocity (m/s)	15
Stoichiometric mixture fraction, η_{st}	0.135

6.2 Computational Set-up

This section provides the details of the computational set-up used for the modelling of the bluff-body flame based on the experimental condition. The computational grid, boundary, and initial conditions are described.

6.2.1 Computational Domain, Boundary Conditions, and Initial Conditions

The computational domain is shown in Fig. 6.1. The domain is created as a wedge of small degree ($\theta = 10°$). The total length of the domain is 750 mm in the axial direction (x), which is slightly longer than the last location of measurement in the experimental work [97]. The radius of the domain is set to 0.06 m in the radial direction (r). At the base of the domain, the fuel inlet extends over a radial distance of 1.8 mm starting from the centreline. The base of the domain starting from $r = 1.8$ mm to $r = 25$ mm takes account for the bluff-body. The rest of the radial width is set as inlet for the air co-flow. The axial end and the side boundary are set as outlet and specified as openings for fluid moving out of the domain. The computational domain is discretized into 145 cells in the radial direction and 350 cells in the axial direction. The grid is non-uniform with highly concentrated number of grids are presented near the main jet and the bluff-body, where the flame is expected to be developed. The grid is less dense in both axial and radial directions away from the flame development region. The detail of the spatial mesh is summarized in Table 6.2. The spatial mesh has 1 cell along the plane of symmetry, thus the simulation is conducted in two dimensional space. The grid independence is examined with rougher and

finer meshes than the current grid. The axial mean mixture fraction profile at the centreline and radial mean mixture fraction profiles at several axial locations are examined. Based on the investigation, it is observed that the grid independence is achieved with the current mesh.

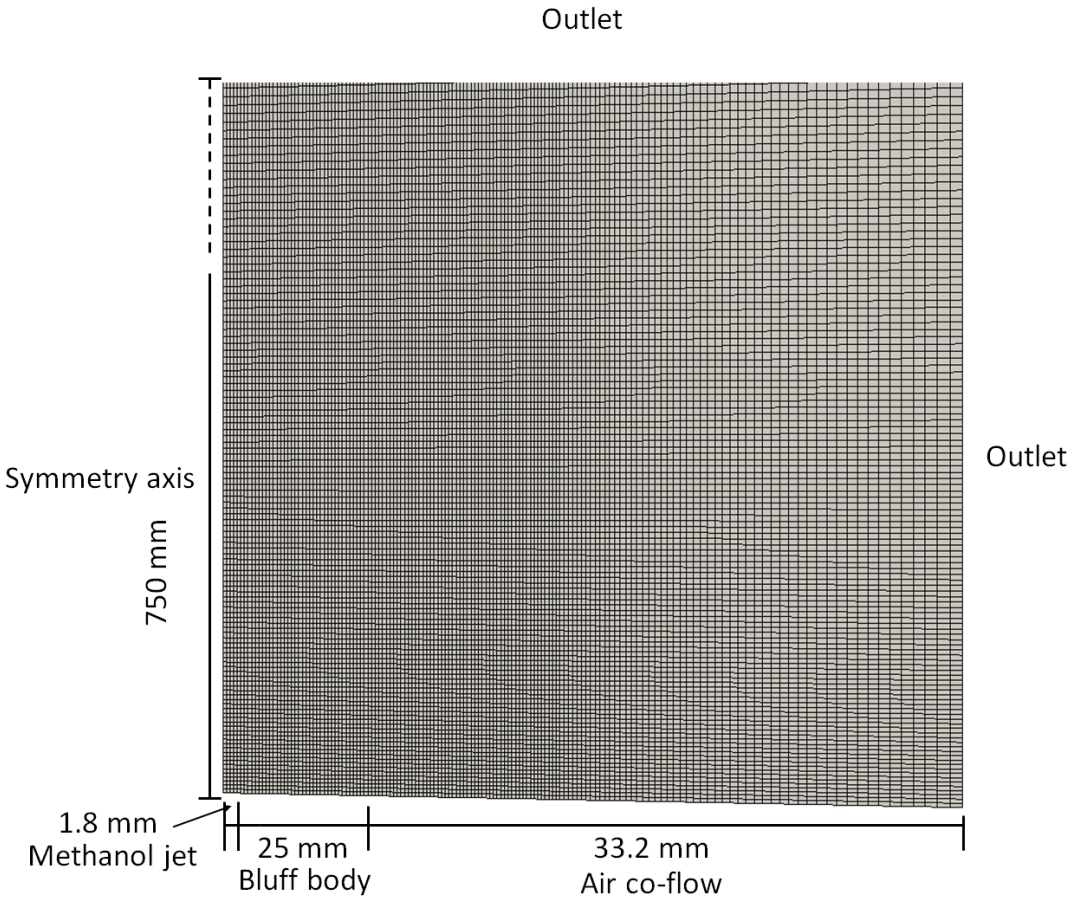

Figure 6.1: Computational mesh for bluff-body flame

The experimental profiles of the mean velocity and its rms fluctuation are implemented at the inlets, as shown in Figure 6.2. The composition of air co-flow is set to $Y_{O_2} = 0.233$ and $Y_{N_2} = 0.677$. The temperature of the air co-flow is set to 373 K. The atmospheric pressure condition is imposed for the fuel and air co-flow inlets.

Table 6.2: Radial distribution of computational mesh for the bluff-body case

Range (mm)	Corresponding boundary at inlet	Number of cells in radial direction	Number of cells in axial direction
$0 - 1.8$	Fuel	6	
$1.8 - 26.8$	Bluff-body	76	350
$26.8 - 60$	Air co-flow	63	

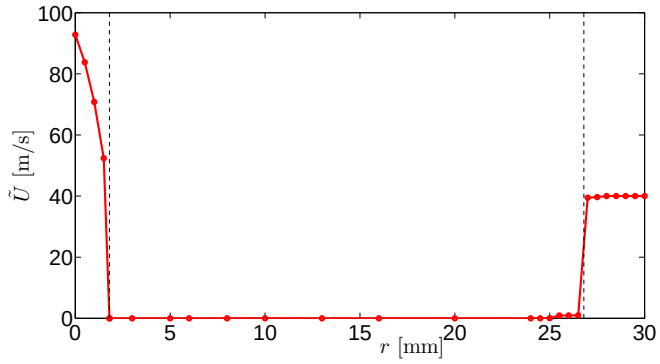

(a) Mean velocity

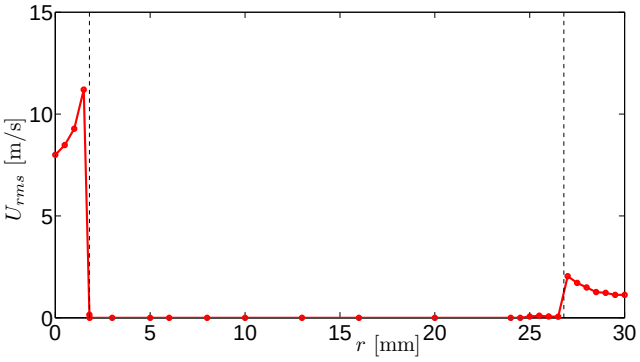

(b) RMS fluctuation of mean velocity

Figure 6.2: Experimental velocity profile and rms profile at fuel inlet, bluff-body, and co-flow inlet

6.2.2 CSE Set-up

Similar to the CSE set-up for the piloted case in Chapter 5, the PDF of mixture fraction is calculated at each computational cell. The number and distribution of sampling mixture fraction are identical to what it is used in the piloted flame case, as shown in Fig. 5.3.

The sensitivity analysis on the size of CSE ensembles is conducted with several different sizes of the ensembles in axial direction: 80 mm, 40 mm, 20 mm, and 10 mm. The difference in Favre averaged species mass fractions and temperature predictions is observed to be negligible from the case with the ensemble size of 20 mm and that of 10 mm. Thus, the ensemble size of 20 mm in the axial direction is kept for the bluff-body flame leading to number of 40 ensembles.

6.2.3 Turbulence Model

The turbulent flow field is solved using the SST $k-\omega$ approach, which is described in Section 2.4.2. Following the same idea of tuning the value of $C_{\epsilon 1}$ in the standard $k-\epsilon$ model in Section 5.3.2, several different values of the empirical constant in the SST $k-\omega$ model is tested to obtain the mixing field as close to the experimental data. This is done by changing value of γ_2 ranging from 0.6 to 0.66. Among the different values of γ_2 tested, the case with $\gamma_2 = 0.66$ provides the most accurate representation of the experimental mixing field.

6.2.4 Chemistry and Radiative Heat Loss

GRI-Mech 2.11 is used for the chemistry kinetics in the simulation. The TGLDM tables for GRI-Mech 2.11 are identical to the ones used in the piloted flame case in Section 5. For the radiative heat loss, the RADCAL model considering the losses due to CO_2 and H_2O only is used.

6.3 Mixing Field

Several values for the empirical constant of SST $k-\omega$ model, γ_2, found in Eq. 2.52, ranging from 0.6 to 0.66 are tested to obtain the value that yields best agreement with experimental data at $x/D_B = 0.9$, $x/D_B = 1.3$, $x/D_B = 1.8$, and $x/D_B = 4.5$. The axial locations of the sampling positions are displayed in Fig. 6.3 mapped with the temperature contour of

the simulated flame. Notice that Fig. 6.3 shows around the first one third of the flame and the $x/D_B = 4.5$ location is not illustrated.

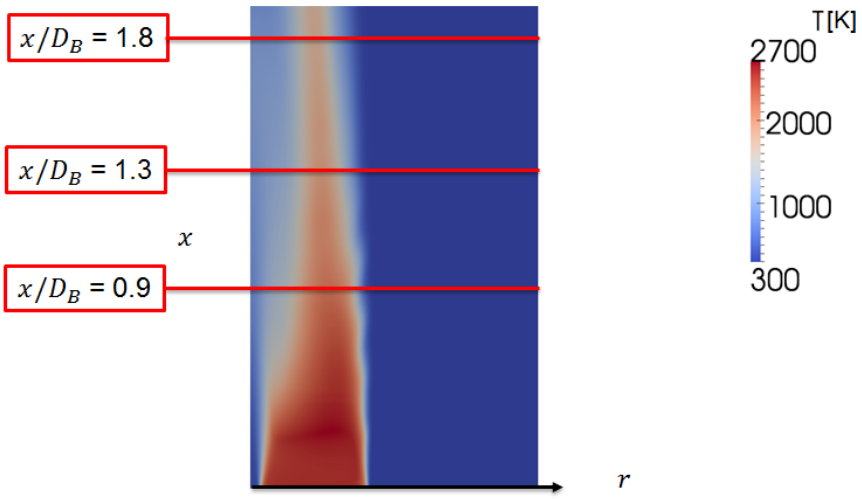

Figure 6.3: Temperature contour of the bluff-body flame from the CSE simulation (first one third of the flame) with the indication of the examined axial locations

It is found that the case with $\gamma_2 = 0.66$ provides the closest agreement for the mean and rms fluctuation of the mixture fraction at the examined locations. Figures 6.4, 6.5, 6.6 and 6.7 show the Favre averaged and the rms fluctuation of the mixture fraction from the CSE simulation with $\gamma_2 = 0.66$ compared with the experimental data [97] and the CMC results [98] at the four axial locations. Overall, the mixing field predicted by CSE is in good agreement with the experimental data. At $x/D_B = 0.9$, CSE overpredicts the Favre averaged mixture fraction between $r = 0$ and $r = 2$ mm with less than 6% difference, as seen in Fig. 6.4 (a). For larger radial distances, the CSE predictions are in better agreement with the experimental data than those obtained in CMC. In CMC, the mixture fraction rms is overpredicted at $x/D_B = 0.9$, as displayed in Fig. 6.4 (b). The mean mixture fraction and mixture fraction rms profiles at $x/D_B = 1.3$ are shown in Fig. 6.5 (a) and (b), respectively. At this location, the mean mixture fraction prediction is similar to what is observed at $x/D_B = 0.9$, where a slight overprediction is observed from $r = 0$ to

$r \simeq 3\ mm$, and accurately represents the experimental data farther radially. For the mean mixture fraction prediction at $x/D_B = 1.8$, the CSE simulation captures the general trend of the experimental data from $r = 0$ to $r \simeq 13\ mm$, while some overprediction is observed in the CMC results within this range, as can bee seen in Fig. 6.6 (a). In contrast, the mixture fraction fluctuation in CSE represents the experimental data within 25% difference along the examined radial locations.

For the last axial location, $x/D_B = 4.5$, both the Favre mean and rms fluctuation of the mean mixture are in good agreement with the experimental data as shown in Fig. 6.7. In terms of predicting the mixture fraction rms, the current predictions are close to the experimental values, in particular in the region between $r = 0$ and $r \simeq 10\ mm$.

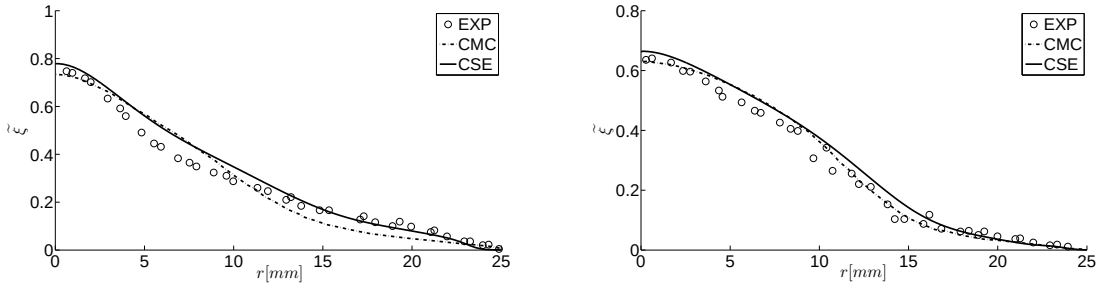

(a) Favre averaged mixture fraction

(b) rms of the mixture fraction

Figure 6.4: Radial profile of mean and rms fluctuation of the mixture fraction predicted by CSE compared with experimental data [90, 97] and previous simulation with CMC approach [98] at $x/D_B = 0.9$

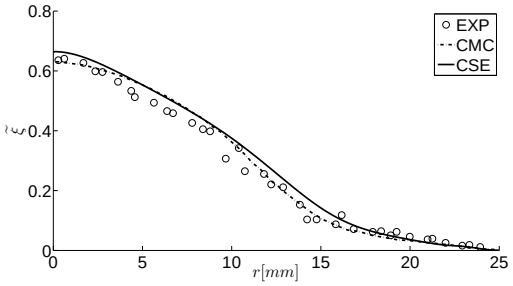

(a) Favre averaged mixture fraction

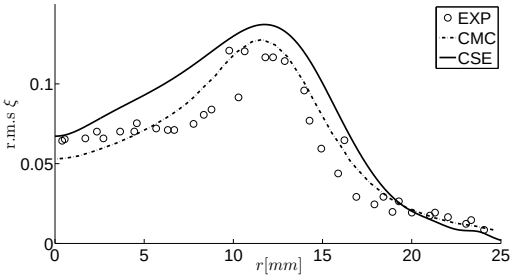

(b) rms of the mixture fraction

Figure 6.5: Radial profile of mean and rms fluctuation of the mixture fraction predicted by CSE compared with experimental data [90, 97] and previous simulation with CMC approach [98] at $x/D_B = 1.3$

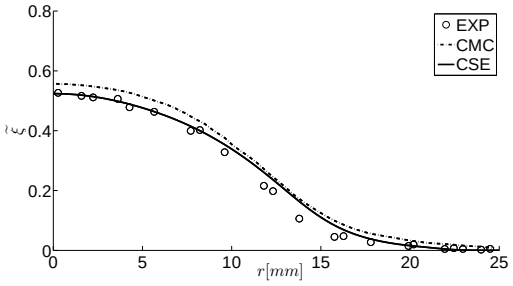

(a) Favre averaged mixture fraction

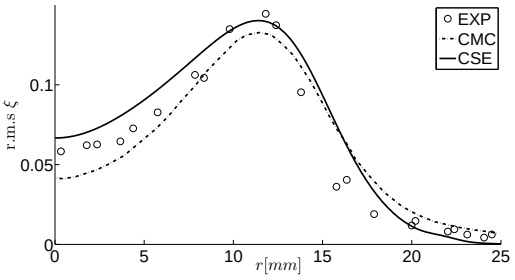

(b) rms of the mixture fraction

Figure 6.6: Radial profile of mean and rms fluctuation of the mixture fraction predicted by CSE compared with experimental data [90, 97] and previous simulation with CMC approach [98] at $x/D_B = 1.8$

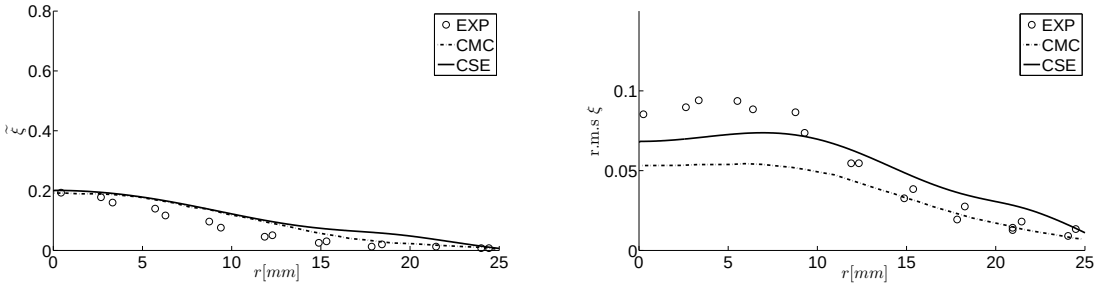

(a) Favre averaged mixture fraction

(b) rms of the mixture fraction

Figure 6.7: Radial profile of mean and rms fluctuation of the mixture fraction predicted by CSE compared with experimental data [90, 97] and previous simulation with CMC approach [98] at $x/D_B = 4.5$

6.4 Conditional Species Mass Fraction and Temperature

Figures 6.8 - 6.11 compare the conditional species mass fractions and temperature obtained from the current CSE simulations to the experimental data and the CMC results at the four axial locations: $x/D_B = 0.9$, $x/D_B = 1.3$, $x/D_B = 1.8$, and $x/D_B = 4.5$. Notice that for each plot, both experimental data and the CMC results of conditional species mass fractions and temperature at two different radial locations are shown: at r = $0.5D_j$ and r = $3D_j$, where D_j is the diameter of the fuel jet in the bluff-body burner. Similar to the piloted flame study, the conditional mass fraction of CO_2, H_2O, O_2, OH, CO, H_2 and CH_3OH, and conditional temperature at each axial location are examined. Figure 6.8 (a) shows the conditional mass fraction of CO_2 at $x/D_B = 0.9$. The CSE predictions are in good agreement with both the experimental data and the CMC results in general. CSE predicts the peak value around 0.147, which is about 10% different from the experimental peak value. Also, the peak occurs around $\eta \simeq 0.12$ in CSE, while near the stoichiometric value of pure methanol, 0.135, is observed in the experiment. The conditional mass fraction of H_2O at the same location predicted by CSE is close to the experimental data, which is also observed in the CMC results. Starting from $\eta \simeq 0.35$, some overprediction in the CSE results can be seen, but remains small, less than 7% difference from the experiment. The conditional mass fraction of O_2 predicted by CSE is comparable to the experimental data. Figure 6.8 (d) shows the conditional mass fraction of OH. Notice that there is a region with sudden reduction of OH mass fraction, between $\eta \simeq 0.08$ and $\eta \simeq 0.1$, which

is believed to be caused by numerical error from the overprediction of CO_2 mass fraction in the same region, as shown in Fig. 6.8 (a). The conditional mass fraction of CO at the same location within the flammability limit of pure methanol is shown in Fig. 6.8 (e). In the region between $\eta \simeq 0.18$ and $\eta \simeq 0.24$, CSE provides the CO mass fractions close to the experimental data, while CMC underpredicts the experimental data significantly. The conditional mass fraction of H_2 predicted by CSE accurately represents the experimental data until $\eta \simeq 0.22$ and for $\eta \geq 0.22$ an overprediction is noticed. For methanol, the CSE predictions are lower than the experimental data in the fuel rich side, as can be seen in Fig. 6.8 (g). Finally, CSE is able to reproduce the profile of the conditional temperature close to the experimental data with small overprediction in the fuel rich side, as shown in Fig. 6.8 (h).

The conditional species mass fractions and temperature at $x/D_B = 1.3$ are shown in Fig. 6.9. Starting with the conditional mass fraction of CO_2 first, the present CSE is found to capture the location and magnitude of the experimental peak accurately, as shown in Fig. 6.9 (a): the peak occurs near the stoichiometric mixture fraction in both CSE and the experimental data. For the mass fraction of water, both CSE and CMC predict the experimental data accurately with slight overprediction after $\eta \simeq 0.2$, as displayed in Fig. 6.9 (b). The predicted conditional mass fractions of OH are close to the experimental data, except in the region between $\eta \simeq 0.14$ and $\eta \simeq 0.27$, where slight overprediction in the CSE values is observed, as presented in Fig. 6.9 (d). The CSE profile is, in fact, closer to the CMC predictions at $r = 3D_j$. The conditional mass fraction of CO and H_2 between $\eta = 0$ and the upper flammability limit of pure methanol at the same location are shown in Fig. 6.9 (e) and Fig. 6.9 (f), respectively. Both the experimental data and CMC results show that the conditional mass fraction of CO from $\eta \simeq 0.25$ varies from the radial locations. CSE reproduces the experimental data for the mass fraction of CO at $r = 3D_j$ very well until $\eta \simeq 0.25$. For H_2, the prediction by CSE is comparable to the experimental data until $\eta \simeq 0.24$. For larger mixture fraction values, an overprediction occurs which is also observed in the CMC results. However, the overprediction seen in the CSE results is larger than that in the CMC results. The conditional mass fraction of methanol is shown in Fig. 6.9 (g). At this location, the CSE predictions are similar to what it is observed at $x/D_B = 0.9$, where the methanol mass fraction is underpredicted in fuel-rich mixtures. As displayed in Fig. 6.9 (h), the predicted conditional temperature closely follows the experimental profiles. Figure 6.10 shows the conditional species mass fractions as well as temperature at $x/D_B = 1.8$. The predictions at this location are very similar to observations made in the other locations. Likewise, at $x/D_B = 4.5$, as can be seen in Fig. 6.11, the conditional averages follow the same shape and trend as what is observed at the previous locations. The only exception is the significant overprediction of H_2O observed in the fuel rich side. The peak value is around 0.2.

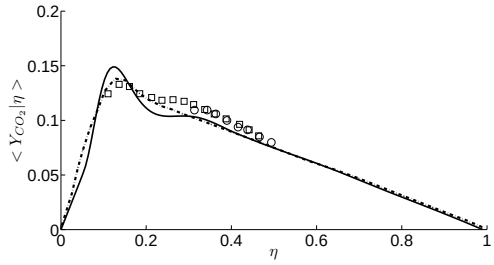

(a) Conditional mass fraction of CO_2

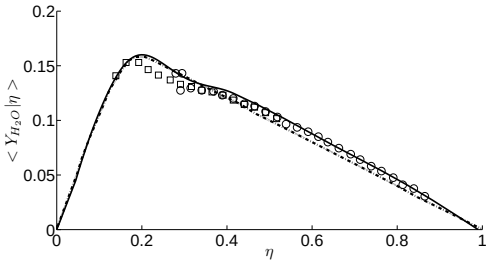

(b) Conditional mass fraction of H_2O

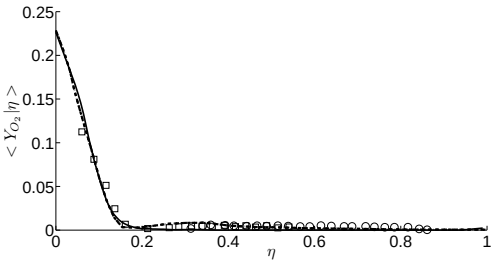

(c) Conditional mass fraction of O_2

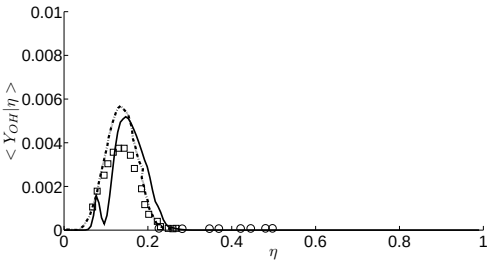

(d) Conditional mass fraction of OH

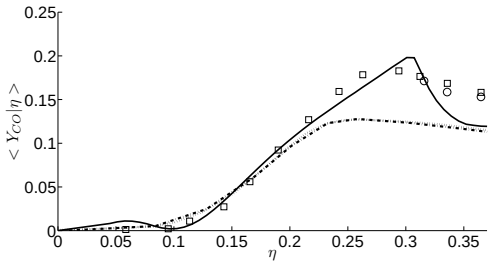

(e) Conditional mass fraction of CO

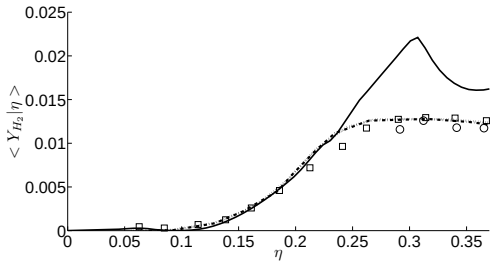

(f) Conditional mass fraction of H_2

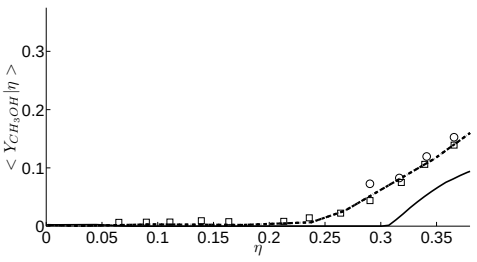

(g) Conditional mass fraction of CH_3OH

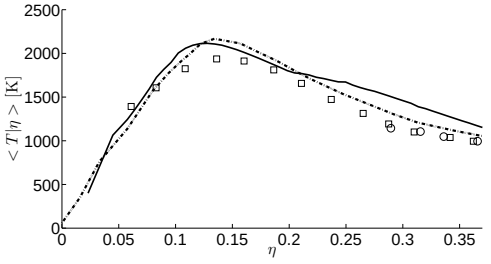

(h) Conditional temperature

Figure 6.8: Conditional species mass fraction and temperature predicted by CSE (-) compared with experimental data ($\circ$ at r $= 0.5D_j$ and $\square$ at r $= 3D_j$) [90, 97] and previous simulation with CMC approach (-·- at r $= 0.5D_j$ and $\cdots$ at r $= 3D_j$) [98] at $x/D_B = 0.9$

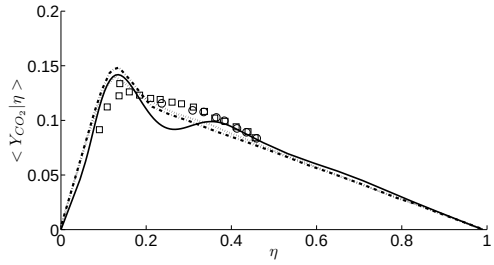

(a) Conditional mass fraction of CO_2

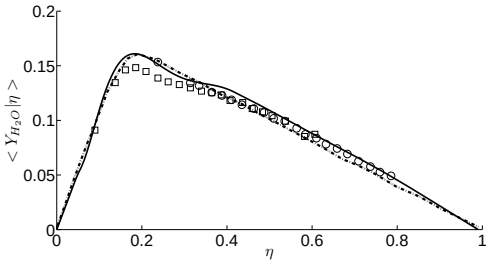

(b) Conditional mass fraction of H_2O

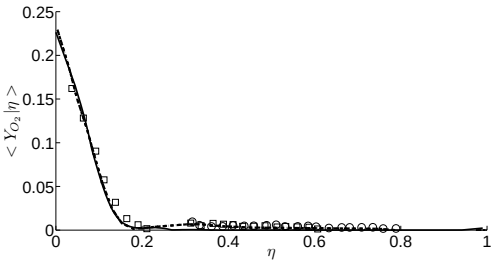

(c) Conditional mass fraction of O_2

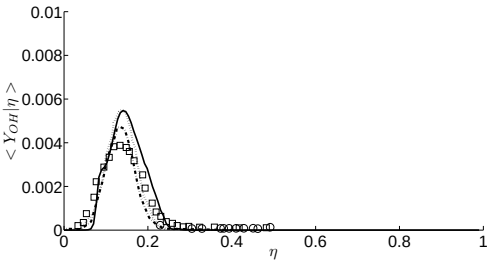

(d) Conditional mass fraction of OH

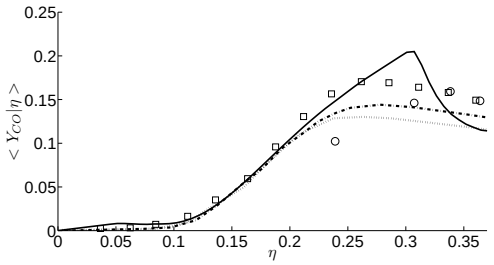

(e) Conditional mass fraction of CO

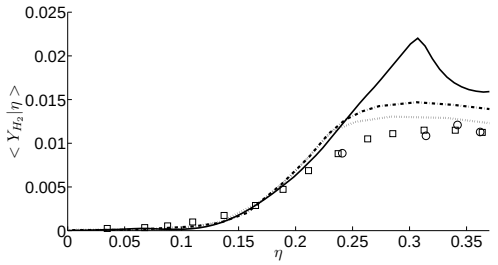

(f) Conditional mass fraction of H_2

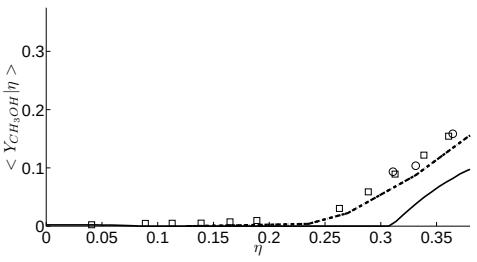

(g) Conditional mass fraction of CH_3OH

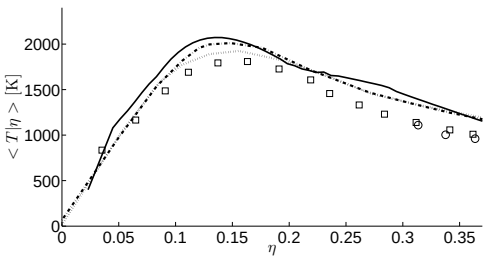

(h) Conditional temperature

Figure 6.9: Conditional species mass fraction and temperature predicted by CSE (-) compared with experimental data ($\circ$ at r $= 0.5D_j$ and $\square$ at r $= 3D_j$) [90, 97] and previous simulation with CMC approach (-·- at r $= 0.5D_j$ and $\cdots$ at r $= 3D_j$) [98] at $x/D_B = 1.3$

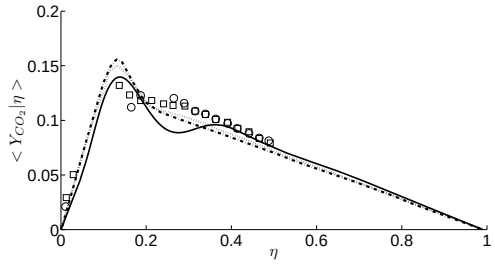

(a) Conditional mass fraction of CO_2

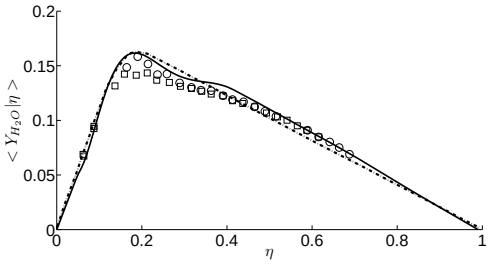

(b) Conditional mass fraction of H_2O

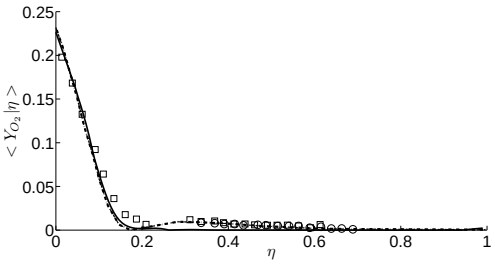

(c) Conditional mass fraction of O_2

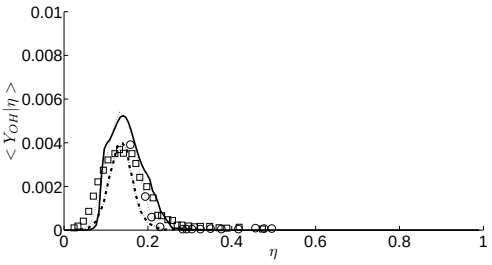

(d) Conditional mass fraction of OH

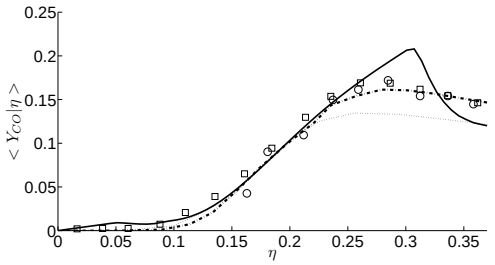

(e) Conditional mass fraction of CO

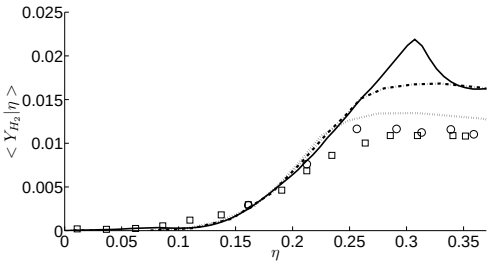

(f) Conditional mass fraction of H_2

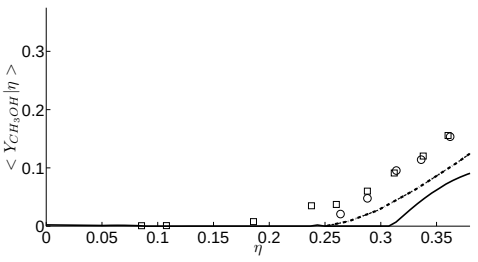

(g) Conditional mass fraction of CH_3OH

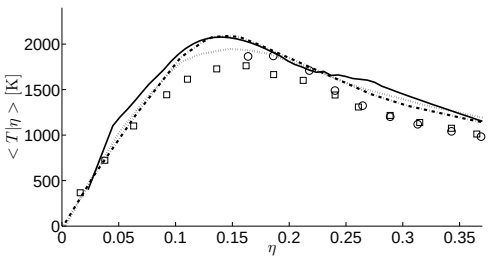

(h) Conditional temperature

Figure 6.10: Conditional species mass fraction and temperature predicted by CSE (-) compared with experimental data ($\circ$ at r = $0.5D_j$ and $\square$ at r = $3D_j$) [90, 97] and previous simulation with CMC approach (-·- at r = $0.5D_j$ and $\cdots$ at r = $3D_j$) [98] at $x/D_B = 1.8$

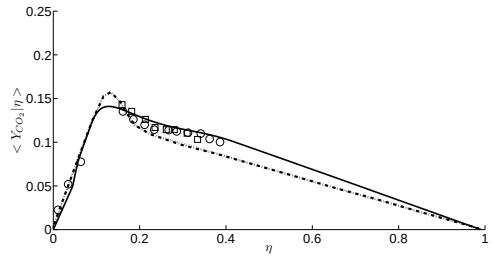

(a) Conditional mass fraction of CO_2

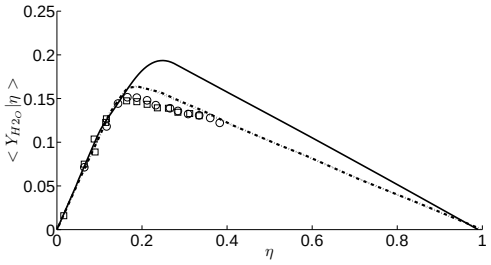

(b) Conditional mass fraction of H_2O

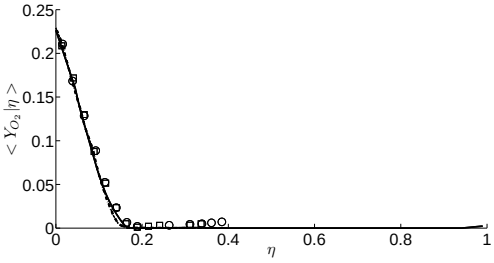

(c) Conditional mass fraction of O_2

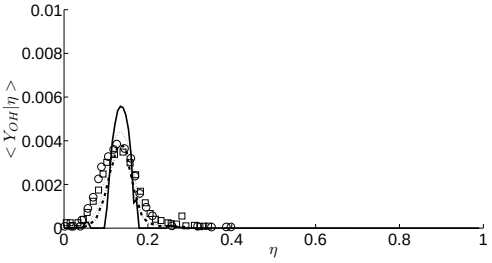

(d) Conditional mass fraction of OH

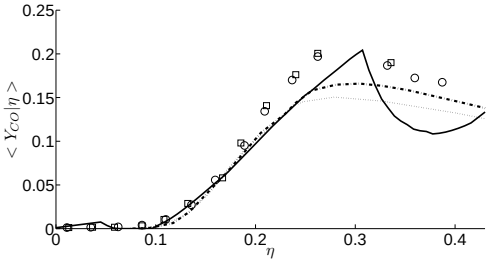

(e) Conditional mass fraction of CO

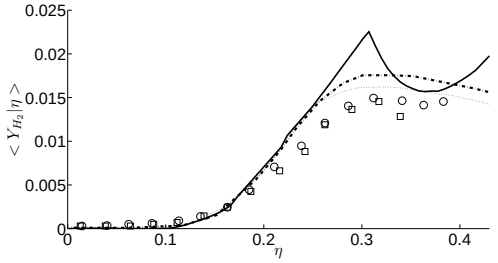

(f) Conditional mass fraction of H_2

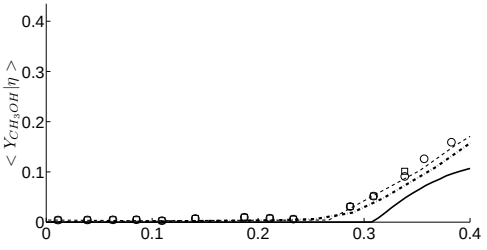

(g) Conditional mass fraction of CH_3OH

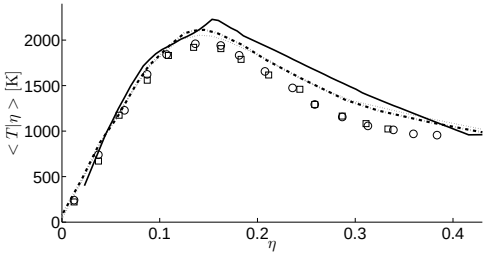

(h) Conditional temperature

Figure 6.11: Conditional species mass fraction and temperature predicted by CSE (-) compared with experimental data ($\circ$ at r $= 0.5D_j$ and $\square$ at r $= 3D_j$) [90, 97] and previous simulation with CMC approach (-·- at r $= 0.5D_j$ and $\cdots$ at r $= 3D_j$) [98] at $x/D_B = 4.5$

The comparison between the experimental data and the results from CSE for the conditional quantities show that CSE is able to predict the experimental data for conditional mass fractions of species and temperature reasonably well with some larger discrepancies on the fuel rich side. Further, the predictions of the conditional species mass fraction and temperature are close to those of CMC results with some small differences. These differences can be explained by several reasons. First, the different turbulence modelling used in the previous CMC study [98] and the present CSE study result in some differences in mixing field predictions, as shown in Figs. 6.4 - 6.7. In the CMC work by Kim and coworkers [98], the modified $k-\epsilon$ model [99] is implemented, whereas the current CSE study considers SST $k-\omega$ [15] model to solve for the turbulent flow field. The differences in the mean (Favre averaged) and fluctuation of the mixing field can result in different predictions for the conditional mass fractions of species and temperature.

The fact that different chemistry mechanisms are considered in CMC and CSE investigations is believed to be another source of discrepancy. In the present work, GRI-Mech 2.11 [65] is selected for the chemistry mechanism, while Kim et al. consider the mechanism developed by Peters [100] with 33 reactions and 15 species. As a test, the CSE calculations are run with the same kinetics as those in [98]. It is found that the predicted conditional mass fractions of CO_2, H_2O and O_2 in CSE are similar to the CMC results as well as their unconditional counter parts, reported in [98]. The CSE predictions using GRI-Mech 2.11 are shown to be closer to the experimental data for most species when compared to the predictions using Peters mechanism. Finally, the different methodology to obtain the conditional species mass fractions and temperature in CMC and CSE is likely to introduce some differences that are difficult to estimate without having CMC and CSE implemented in the same CFD code.

Some discrepancies in the turbulent mixing are noted in Section 6.3 in comparison with the experimental data. These are suspected to the main source of discrepancies between the CSE predictions and the experimental values as the mixture fraction PDF, function of mean mixture fraction and its variance, is a key variable in the inversion process to determine the conditional averages. Most discrepancies in the turbulent predicted mixing field are associated with the rms of mixture fraction. As for the piloted flame examined in Section 5, differential diffusion seems to be non-negligible, in particular for the mass fraction of H_2 and will need to be included in the future for improved predictions of some of the species concentrations

6.5 Unconditional Species Mass Fractions and Temperature

Figures 6.12 to 6.15 show the Favre averaged species mass fractions and temperature predicted by CSE compared with the experimental data and the CMC results at the same four axial locations. At $x/D_B = 0.9$, the Favre averaged mass fractions of CO_2 and H_2O predicted by CSE are in better agreement with the experimental data than those of CMC. For these two species, CMC underpredicts the experimental values in the region between $r = 13mm$ and $r = 23\ mm$. The underpredictions by CMC for these two species are not observed in the CSE results, as shown in Fig. 6.12 (a) and 6.12 (b). The Favre averaged mass fractions of O_2 and OH at $x/D_B = 0.9$ location are shown in Fig. 6.12 (c) and (d), respectively. For O_2 and OH, CSE also reproduces the experimental data more accurately than what is seen in CMC. CMC overpredicts the mass fraction of O_2 in the region between $r \simeq 10\ mm$ and $r \simeq 24\ mm$, where this overprediction is significantly reduced in CSE. For the mass fraction of OH, CSE predictions are closer to the experimental data compared to CMC, in particular in the region between $r \simeq 13\ mm$ and $r \simeq 22\ mm$. The underprediction seen in CMC is significantly improved in CSE in this region. Figure 6.12 (e) shows the Favre averaged mass fraction of CO at $x/D_B = 0.9$. An undeprediction can be seen in the CMC results, whereas CSE accurately reproduces the experimental profile for $r \geq 9\ mm$. However, for the unconditional mass fraction of H_2, CSE does not give good predictions compared to the experimental data and CMC results agree with experimental values better. A significant overprediction is observed between $r \simeq 2\ mm$ and $r \simeq 15\ mm$. As presented in Fig. 6.12 (g), the CSE predicted methanol mass fractions are in good agreement with the experimental values with a small overprediction of the centreline. For the temperature, as shown in Fig. 6.12 (h), CSE overcomes the significant underprediction by CMC in the region between $r \simeq 12\ mm$ to $r \simeq 23\ mm$. In fact, this is the region where the predictions of the mass fraction of CO_2 and H_2O by CSE are much closer to the experimental data than those of CMC. Overall, the CSE predictions are in better agreement with the experimental data than the CMC results except for H_2, which is consistent with the overprediction in the conditional counterpart. The main reason of improved predictions in CSE would be due to better prediction in mean and fluctuation of the mixing field at this location than the CMC results.

Figure 6.13 displays the Favre averaged species mass fractions and temperature at $x/D_B = 1.3$. At this location, the prediction of the unconditional mass fractions of CO_2, H_2O, O_2, and OH are similar to the those obtained from CMC, and they both reproduce the experimental data very well, as shown in Fig. 6.13. For the mass fraction of CO, CMC underpredicts the experimental data from $r = 0$ to $r \simeq 10\ mm$, while an opposite

trend is seen in the CSE predictions by having an overprediction within this range. The overprediction of the mass fraction of CO in the fuel rich side is believed to responsible for the overprediction of the Favre averaged counterpart within $r = 0$ to $r \simeq 10\ mm$. Similar to the observation made at $x/D_B = 0.9$, the mass fraction of H_2 is also overpredicted at $x/D_B = 1.3$, as shown in Fig. 6.13 (f), which is consistent to what is observed in the conditional profile. The methanol mass fractions are smaller than the experimental values, still in reasonable agreement and CMC seems to produce values closer to the experimental values, as presented in Fig. 6.13 (g). The Favre averaged temperature obtained from CSE falls within the experimental measurements, as shown in Fig. 6.13 (h). The radial profiles of unconditional mass fractions of species and temperature from CSE predictions compared with the experimental data and CMC results at $x/D_B = 1.8$ are presented in Fig. 6.14. At this location, the CSE predicted values are similar to the observations made in the other two axial locations. In general, CSE yields good agreement with the experimental data, except the model overpredicts the mass fraction of H_2 significantly.

For the Favre averaged mass fraction of species and temperature at $x/D_B = 4.5$, CSE yields good agreement with the experimental data. The mass fraction of CO_2 is better predicted by the current simulations compared to the previous CMC results, in particular from $r \simeq 3\ mm$, as shown in Fig. 6.15 (a). However, the predicted Favre averaged mass fraction of H_2O are larger than the the CMC values between $r = 0$ and $r \simeq 6\ mm$, consistent with the overprediction of conditional counterpart. The Favre averaged mass fraction of O_2 predicted by CSE is very close to the experimental data, while significant underprediction is observed in the CMC results. CSE undepredicts the mass fractions of CO and H_2 in the region where an overprediction of H_2O is observed. Good agreement for methanol concentration is observed. Good prediction of the temperature is obtained in the present CSE calculations, as shown in Fig. 6.15 (h).

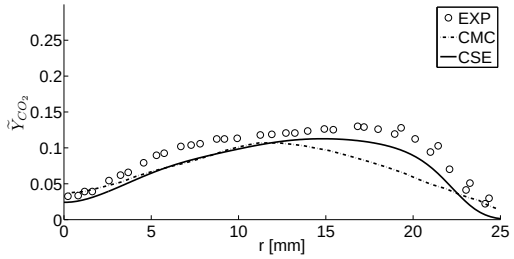

(a) Favre averaged mass fraction of CO_2

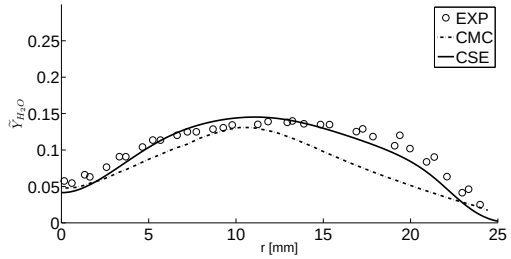

(b) Favre averaged mass fraction of H_2O

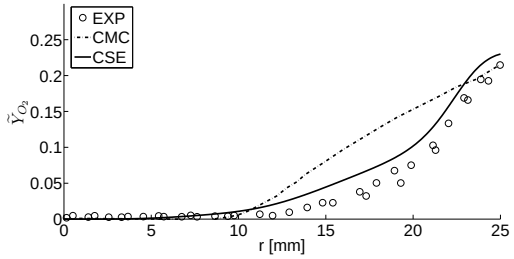

(c) Favre averaged mass fraction of O_2

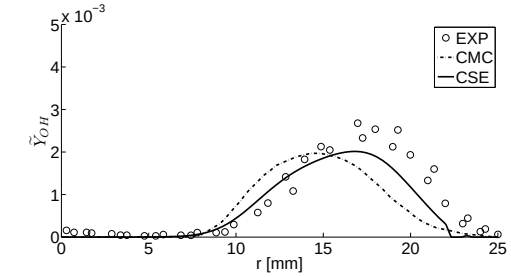

(d) Favre averaged mass fraction of OH

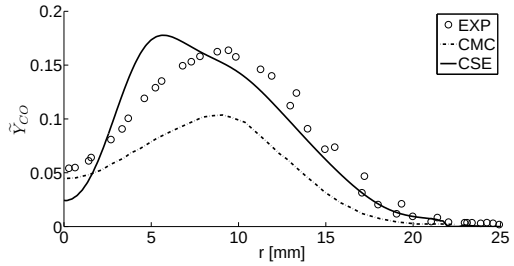

(e) Favre averaged mass fraction of CO

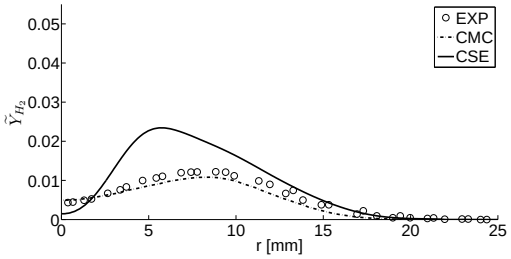

(f) Favre averaged mass fraction of H_2

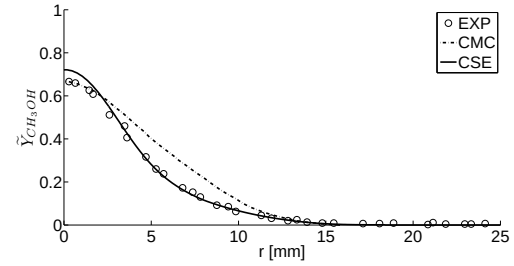

(g) Favre averaged mass fraction of CH_3OH

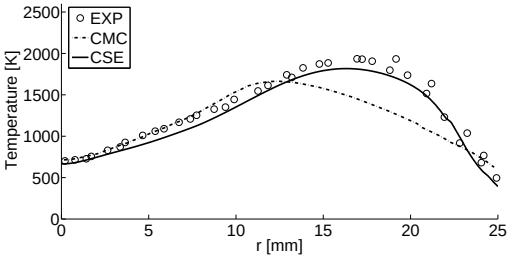

(h) Favre averaged temperature

Figure 6.12: Radial profiles of the Favre averaged mass fraction of species and temperature predicted by CSE compared with experimental data [90, 97] and previous simulation with CMC approach [98] at $x/D_B = 0.9$

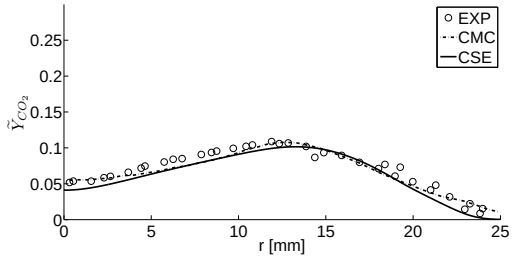

(a) Favre averaged mass fraction of CO_2

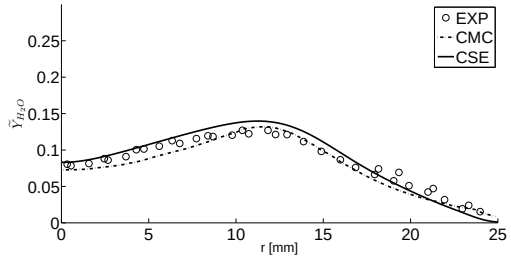

(b) Favre averaged mass fraction of H_2O

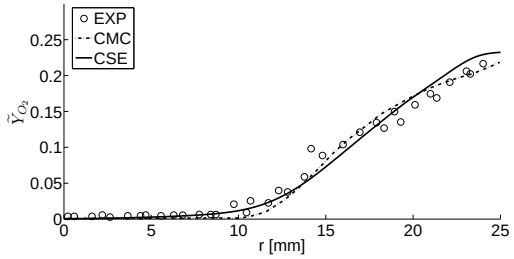

(c) Favre averaged mass fraction of O_2

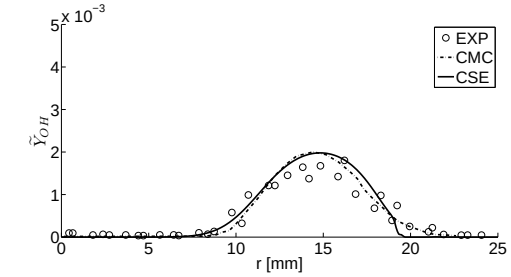

(d) Favre averaged mass fraction of OH

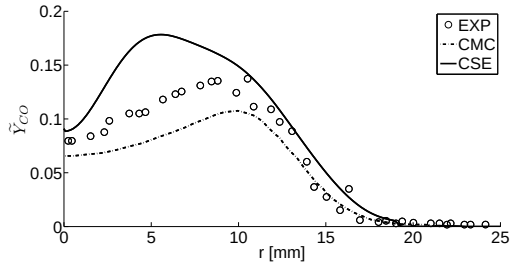

(e) Favre averaged mass fraction of CO

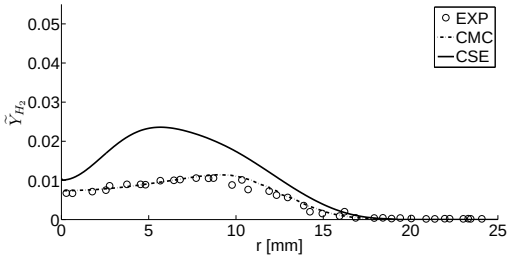

(f) Favre averaged mass fraction of H_2

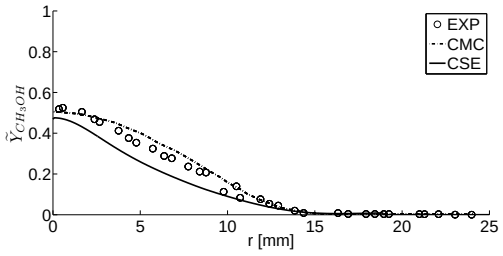

(g) Favre averaged mass fraction of CH_3OH

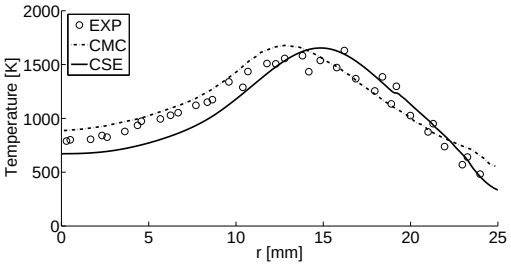

(h) Favre averaged temperature

Figure 6.13: Radial profiles of the Favre averaged species mass fraction and temperature predicted by CSE compared with experimental data [90, 97] and previous simulation with CMC approach [98] at $x/D_B = 1.3$

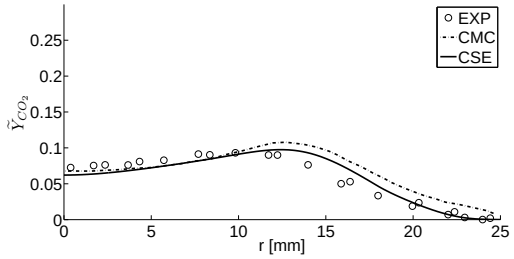

(a) Favre averaged mass fraction of CO_2

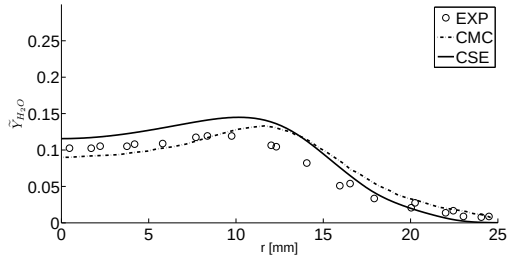

(b) Favre averaged mass fraction of H_2O

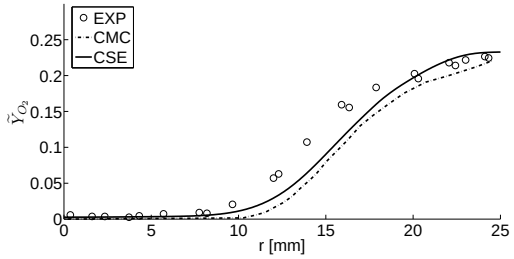

(c) Favre averaged mass fraction of O_2

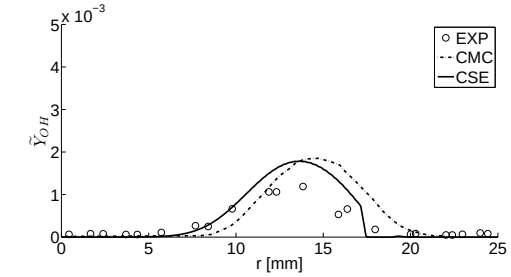

(d) Favre averaged mass fraction of OH

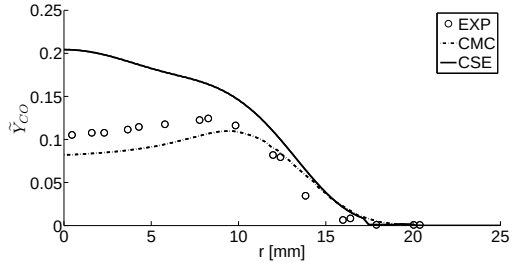

(e) Favre averaged mass fraction of CO

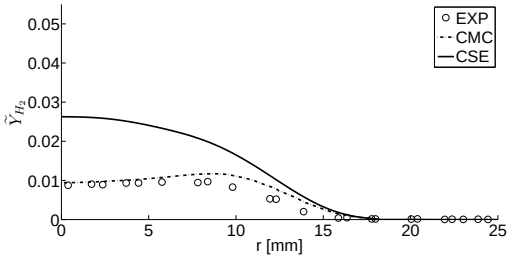

(f) Favre averaged mass fraction of H_2

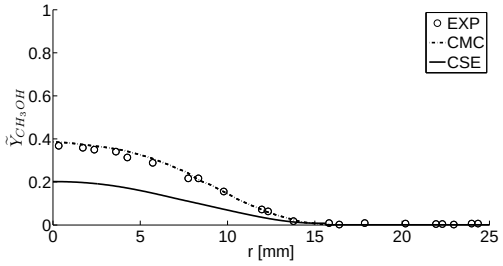

(g) Favre averaged mass fraction of CH_3OH

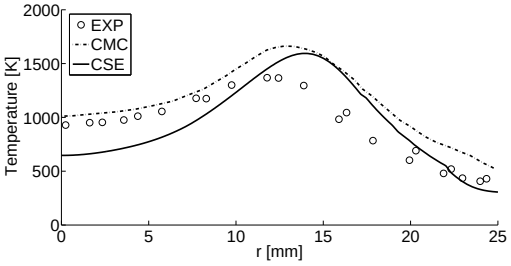

(h) Favre averaged temperature

Figure 6.14: Radial profiles of the Favre averaged species mass fraction and temperature predicted by CSE compared with experimental data [90, 97] and previous simulation with CMC approach [98] at $x/D_B = 1.8$

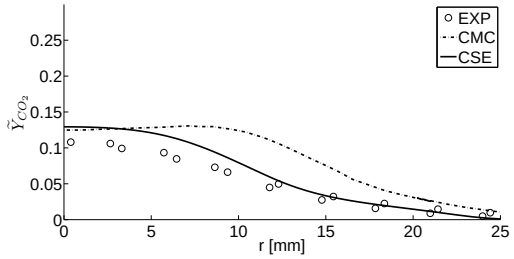

(a) Favre averaged mass fraction of CO_2

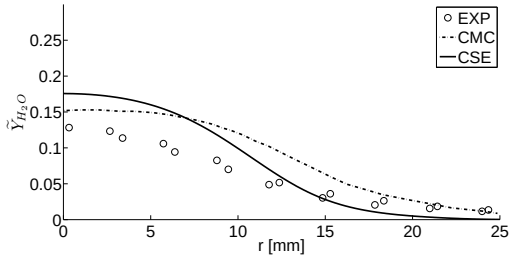

(b) Favre averaged mass fraction of H_2O

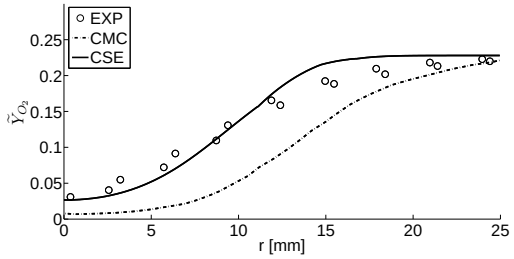

(c) Favre averaged mass fraction of O_2

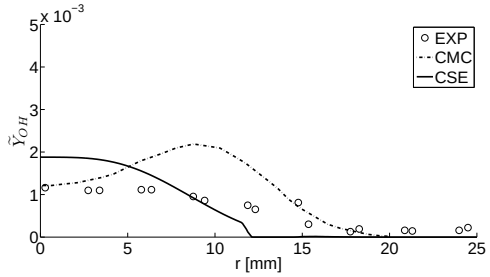

(d) Favre averaged mass fraction of OH

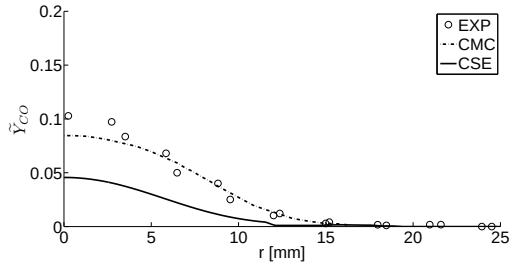

(e) Favre averaged mass fraction of CO

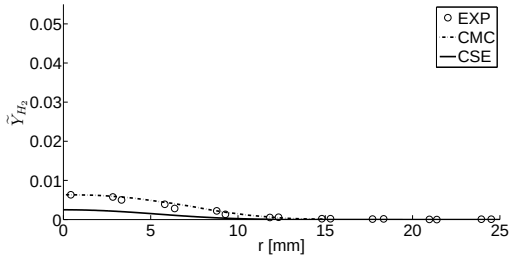

(f) Favre averaged mass fraction of H_2

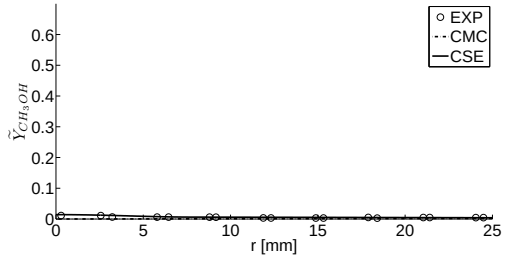

(g) Favre averaged mass fraction of CH_3OH

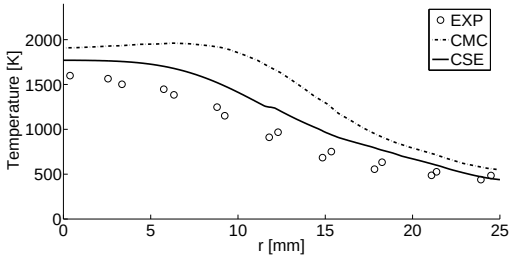

(h) Favre averaged temperature

Figure 6.15: Radial profiles of the Favre averaged species mass fraction and temperature predicted by CSE compared with experimental data [90, 97] and previous simulation with CMC approach [98] at $x/D_B = 4.5$

6.6 Summary

In this chapter, the numerical investigation of a turbulent non-premixed methanol bluff-body flame using CSE is presented. Good predictions are obtained for the mixing field as well as the conditional and unconditional species mass fractions and temperature. Comparison with the more available data than the piloted case in Chapter 5 shows that CSE can reproduce methanol flame very accurately. However, the prediction of species mass fraction of H_2 is also quite poor, which is suspected to be mainly due to the exclusion of differential diffusion effect within the simulation.

Chapter 7

Conclusions

The focus of the present study is to investigate the applicability of CSE to reproduce turbulent non-premixed methanol flames. For the first time, CSE is applied to simulate turbulent flames that burn methanol, which has a more complex chemical structure than methane. CSE combined with TGLDM for the chemistry tabulation is shown to reproduce turbulent non-premixed methanol piloted and bluff-body flames successfully. The combustion model is able to capture accurate chemistry within the wide range of the flammability limits of methanol. The presumed β shaped PDF of the mixture fraction [48] and zeroth order Tikhonov regularization [38] are included in the current CSE study. The two equation RANS models are used to solve for turbulent flow field for both the piloted and bluff-body cases, and GRI-Mech 2.11 is used for chemistry kinetics. The numerical implementation of the CSE model in CFD, used in the present study, is described: the conditional chemical source terms for species CO_2 and H_2O are retrieved from the TGLDM table and integrated over the sampling mixture fraction range, whereas the mass fractions of the remaining species including CH_3OH, O_2, CO, H_2, and OH are calculated directly from the table. For each investigated flame, the spatial grid refinement and the effect of the size of CSE ensembles are examined. The performance of CSE for the two flames is evaluated by comparing the CSE results of species mass fractions and temperature to the available experimental data and previously simulated results using the CMC method.

7.1 Methanol Flame Results

7.1.1 Piloted Flame Results

The piloted flame experimentally investigated by Masri et al. [88] is reproduced using the CSE method. For the turbulent flow field, the RANS standard $k-\epsilon$ equation is used. Several values of the empirical constant, $C_{\epsilon 1}$, are tested to obtain the best value that reproduces the experimental mixing field, and the case with $C_{\epsilon 1} = 1.7$ provides the most accurate predictions on the mean mixture fraction from the experiment.

The conditional mass fractions of CO_2, H_2O, O_2, OH, CO, H_2, and CH_3OH and temperatures at two axial locations, $x/D = 20$ and $x/D = 40$, are examined. The conditional results are compared with the experimental data by Masri et al. [88, 90] and previous numerical results using the CMC method by Roomina and Bilger [93]. The CSE results agree well with the experimental data except for H_2, where significant overprediction of the species is observed in the fuel rich side. A similar trend is also observed in the CMC results.

The unconditional or Favre averaged mass fractions of the reactive species and temperature are examined at only the $x/D = 20$ location. Overall, the CSE results on the Favre averaged quantities agree well with the experimental data except for H_2. A significant overprediction of the species is observed near the centreline, where the corresponding mean mixture fraction is greater than 0.2.

Several possible sources may be identified to explain the discrepancies between the CSE predictions and the experimental data. The most significant is the exclusion of the differential diffusion effect within the simulation, which is suspected to be the main cause of the overprediction of H_2 mass fractions. Another possible source of discrepancy is the chemistry mechanism used in the tabulation. In their CMC work, Roomina and Bilger [93] report that one of the reactions in GRI Mech 2.11, $CH_3OH + H => CH_2OH + H_2$, has significantly larger reaction constants than the chemistry mechanism developed by Chen [94], which provides good agreement with the experimental data on H_2.

7.1.2 Bluff-body Flame Results

The second flame of interest, the turbulent non-premixed methanol flame experimentally investigated by Dally et al. [97], is reproduced using CSE. The RANS SST $k-\omega$ model with $\gamma_2 = 0.66$ provides accurate predictions of the turbulent mixing field. The results of the mean and variance of the mixture fraction are compared to the experimental data at four locations: $x/D_B = 0.9$, $x/D_B = 1.3$, $x/D_B = 1.8$, and $x/D_B = 4.5$.

At all the four locations, the conditional temperature and species mass fractions of CO_2, H_2O, O_2, OH, CO, H_2, and CH_3OH are compared with the experimental data and previous numerical results using the CMC method by Kim et al. [98]. CSE is able to provide accurate predictions for most of the conditional quantities except for H_2, where significant overprediction is observed in the fuel rich side. Again, the main cause of the overprediction is suspected to be the negligence of the differential diffusion effect in the chemistry tabulation process.

The unconditional species mass fractions and temperature are compared with the experimental data and the CMC results at the four locations. At the $x/D_B = 0.9$ location, the Favre averaged results from the CSE simulation represent the experimental data significantly better than the CMC results especially for $\widetilde{Y}_{CO_2}$, $\widetilde{Y}_{H_2O}$ and temperature. It is believed that the better predictions by CSE are due to more accurate predictions of the mixing field shown in the mean and variance of the mixture fractions, implying that capturing an accurate prediction of the mixing field is the key parameter for successful simulation in CSE. For the other three axial locations, the level of agreement with the experimental data between the CSE and CMC is similar except for H_2.

As a test, CSE calculations with the same chemistry mechanism used in the CMC work by Kim et al. [98] are run to see whether the CSE provides similar predictions to the CMC results. The TGLDM tables using the chemistry mechanism by Peters [100] is applied to simulate the same flame. Subsequently, it is found that the mass fractions of CO_2, H_2O, and O_2 in CSE are similar to those of CMC. The overprediction of H_2 mass fractions, however, is still observed.

7.2 Summary of Accomplishments

The previous studies on CSE have focused on the flames that burn methane and methane-based mixtures as fuels, even though the applicability of the model is not limited to a particular fuel in theory. In the present work, the performance of CSE for reproducing flames that burn fuels with more complex chemical structure than that of methane is assessed. The main key finding from the present investigation of methanol flames is that CSE yields accurate predictions of the species mass fractions and temperature compared to the available experimental data, which suggests that CSE is applicable to simulate flames of any fuels. The present study can be the starting point of possible future investigations of CSE for combustion of fuels with even more complex chemical structure in industry.

7.3 Recommendations and Future Work

In the current study, the tabulated chemistry via the TGLDM method is used for chemistry calculation. The current implementation of TLGDM, however, does not consider the differential diffusion effect. Since the overprediction of H_2 is suspected to be caused mainly by the neglect of the differential diffusion, it is highly recommended to reconfigure the chemistry table using other chemistry tabulation techniques, which can adapt the differential diffusion of reactive species.

Improvements in mixing field predictions using LES are also suggested for future work. It is seen from the bluff-body case that the better predi ctions in mean and variance of mixture fraction lead to more accurate predictions of the species mass fractions and temperature.

Finally, it is suggested to include CSE simulation of burning fuels with more complex chemical structure than methanol. Ethanol is a good candidate to start because its use in the automobile industry has been increased over the last few decades. Investigating CSE on more complex fuels will allow wider applications of the model in the future.

References

[1] "Energy efficiency trends in canada." http://publications.gc.ca/site/eng/9.505928/publication.html. Accessed: 2015-10-30.

[2] Y. Wei, S. Liu, H. Li, R. Yang, J. Lium, and Y. Wang, "Effects of methanol/gasoline blends on a spark ignition engine performance and emissions," *Energ. Fuel.*, vol. 22, pp. 1254–1259, 2008.

[3] S. B. Pope, *Turbulent Flows*. Cambridge University Press, 2000.

[4] A. Y. Klimenko and R. W. Bilger, "Conditional moment closure for turbulent combustion," *Prog. Energy Combust. Sci.*, vol. 25 (6), pp. 595–687, 1999.

[5] R. W. Johnson, *The Handbook of Fluid Dynamics*. CRC Press LLC, 1998.

[6] T. Poinsot, S. Candel, and A. Trouvé, "Applications of direct numerical simulation to premixed turbulent combustion," *Prog. Energy Combust. Sci.*, vol. 21, pp. 531–576, 1995.

[7] T. Poinsot, "Using direct numerical simulations to understand premixed turbulent combustion," *International Symposium on combustion*, vol. 26, pp. 219–232, 1996.

[8] T. Baritaud, T. Poinsot, and M. Baum, *Direct numerical simulation for turbulent reacting flows*. Editions TECHNIP, 1996.

[9] L. Vervisch and T. Poinsot, "Direct numerical simulation of non-premixed turbulent flames," *Annual Rev. of Fluid Mech.*, vol. 30, pp. 655–691, 1996.

[10] J. Chen, "Petscale direct numerical simulation of turbulent combustion-fundamental insights towards predictive models," *Proc. Combust. Inst.*, vol. 33, pp. 99–123, 2011.

[11] H. K. Versteeg and W. Malalasekraa, *An Introduction to Computational Fluid Dynamics, The Finite Volume Method*. Pearson Education Limited, 2007.

[12] B. E. Launder and D. B. Spalding, "The numerical computation of turbulent flows," *Computer Methods in Applied Mechanics and Engineering*, vol. 3, pp. 269–289, 1974.

[13] P. Bradshaw, T. Cebeci, and J. H. Whitelaw, *Engineering Calculation Methods for Turbulent Flow*. Academic Press London, 1981.

[14] D. C. Wilcox, "Re-assessment of the scale-determining equation for advanced turbulence models," *AIAA J.*, vol. 26, pp. 1299–1310, 1988.

[15] F. R. Menter, "Two-equation eddy-viscosity turbulence models for engineering applications," *AIAA J.*, vol. 32, pp. 1598–1605, 1994.

[16] M. Lesieur, "New trends in large-eddy simulations of turbulence," *Annu. Rev. Fluid Mech.*, vol. 28, pp. 45–82, 1996.

[17] U. Piomelli and J. R. Chasnov, "Large-Eddy Simulations: Theory and Applications," in *Turbulence and Transition Modelling* (H. Hallbäck, D. S. Henningson, A. V. Johansson, and P. H. Alfredsson, eds.), vol. 2 of *ERCOFTAC Series*, pp. 269–336, Springer Netherlands, 1996.

[18] P. A. Libby and F. A. Williams, *Turbulent Reacting Flows*. Berlin: Springer-Verlag, 1981.

[19] D. Veynante and L. Vervisch, "Turbulent combustion modelling," *Prog. Energy Combust. Sci.*, vol. 28(3), pp. 193–266, 2002.

[20] B. F. Magnussen and B. H. Hjertager, "On mathematical modeling of turbulent combustion with special emphasis on soot formation and combustion," *Proc. Combust. Inst.*, vol. 16, pp. 719–729, 1977.

[21] N. Peters, "Laminar diffusion flamelet models in non-premixed turbulent combustion," *Prog. Energy Conbust.*, vol. 10, pp. 319–339, 1984.

[22] S. B. Pope, "Lagrangian PDF methods for turbulent flows," *Annu. Rev. Fluid Mech.*, vol. 26, pp. 23–63, 1994.

[23] S. B. Pope and W. K. Cheng, "The stochastic flamelet model of turbulent premixed combustion," *Proc. Combust. Inst.*, vol. 22, pp. 781–789, 1989.

[24] S. B. Pope, "A Monte Carlo method for the PDF equation of turbulent reacting flow," *Combust. Sci. Technol.*, vol. 25, pp. 159–174, 1981.

[25] S. B. Pope, "PDF methods for turbulent reactive flows," *Prog. in Energ. Combust. Sci.*, vol. 11, pp. 119–192, 1985.

[26] D. C. Haworth, "Progress in probability density function methods for turbulent reacting flows," *Prog. Energy Combust. Sci.*, vol. 36, pp. 168–259, 2010.

[27] A. Y. Klimenko, "Multicomponent diffusion of various admixtures in turbulent flow," *Fluid Dynamics*, vol. 25, pp. 327–334, 1990.

[28] R. W. Bilger, "Conditional moment closure for turbulent reacting flow," *Phys. Fluid A*, vol. 5, pp. 336–444, 1993.

[29] A. Kronenbourg and E. Mastorakos, "The conditional moment closure model, New Trends and Perspectives," in *Turbulent Combustion Modelling Advances* (T. Echekki and E. Mastorakos, eds.), Springer, 2011.

[30] E. Mastorakos and R. W. Bilger, "Second-order conditional moment closure for the autoignition of turbulent flows," *Phys. Fluids*, vol. 10, pp. 1246–1248, 1998.

[31] S. H. Kim, K. Y. Huh, and R. A. Fraser, "Modeling autoignition of a turbulent methane jet by the conditional moment closure model," *Proc. Combust. Inst.*, vol. 28, pp. 185–191, 2000.

[32] S. H. Kim, K. Y. Huh, and R. W. Bilger, "Second-order conditional moment closure modeling of local extinction and reignition in turbulent non-premixed hydrocarbon flames," *Proc. Combust. Inst.*, vol. 29, pp. 2131–2137, 2002.

[33] A. Y. Klimenko and S. B. Pope, "The modeling of turbulent reactive flows based on multiple mapping conditioning.," *Phys. Fluids*, vol. 15, pp. 1907–1925, 2003.

[34] M. J. Cleary, A. Y. Klimenko, J. Janicka, and M. Pfitzner, "A sparse-lagrangian multiple mapping conditioning model for turbulent diffusion flames," *Proc. Combust. Inst.*, vol. 32, no. 1, pp. 1499–1507, 2009.

[35] K. Vogiatzaki, A. Kronenburg, M. J.Cleary, and J. H. Kent, "Multiple mapping conditioning of turbulent jet diffusion flames," *Proc. Combust. Inst.*, vol. 32, no. 2, pp. 1679–1685, 2009.

[36] W. K. Bushe and H. Steiner, "Conditional moment closure for large eddy simulation of nonpremixed turbulent reacting flows," *Phys. Fluids*, vol. 11, pp. 1896–1906, 1999.

[37] M. Wang and J. Huang, "Simulation of a turbulent non-premixed flame using conditional source-term estimation with trajectory generated low-dimensional manifold," *Phys. Fluids*, vol. 31, pp. 1701–1709, 2007.

[38] A. Tikhonov and V. Arsenin., "Solution of incorrectly formulated problems and the regularization method," *Phys. Fluids*, vol. 4, pp. 1035–1038, 1963.

[39] P. C. Hansen, "The truncated SVD as a method for regularization," *BIT*, vol. 27, pp. 534–553, 1987.

[40] J. W. Labahn, C. B. Devaud, T. Sipkens, and K. J. Daun, "Inverse analysis and regularisation in conditional source-term estimation modelling," *Combust. Theory Model.*, vol. 18, pp. 474–499, 2014.

[41] R. W. Grout, W. K. Bushe, and C. Blair, "Predicting the ignition delay of turbulent methane jets using conditional source-term estimation," *Combust. Theor. Model.*, vol. 11, pp. 1009–1028, 2007.

[42] J. W. Labahn and C. B. Devaud, "Investigation of conditional source-term estimation applied to a non-premixed turbulent flame," *Combust. Theor. Model.*, vol. 17, pp. 960–982, 2013.

[43] D. Dovizio, M. M. Salehi, and C. Devaud, "RANS simulation of a turbulent premixed bluff body flame using conditional source-term estimation," *Combust. Theor. Model.*, vol. 17, pp. 935–959, 2013.

[44] D. Dovizio, J. W. Labahn, and C. B. Devaud, "Doubly Conditional Source-term Estimation (DCSE) applied to a series of lifted turbulent jet flames in cold air," *Combust. Theor. Model.*, vol. 162(5), pp. 1976–1986, 2015.

[45] S. B. Pope and U. Maas, "Simplifying chemical kinetics: Trajectory low-dimensional manifolds in composition space," tech. rep., FDA 93-11.

[46] J. Huang and W. K. Bushe, "Simulation of transient turbulent methane jet ignition and combustion under engine-relevant conditions using conditional source-term estimation with detailed chemistry," *Combust. Theor. Model.*, vol. 162(5), pp. 977–1008, 2007.

[47] F. Williams, *Combustion theory*. Benjamin Cummings, Menlo Park, CA, 1985.

[48] S. S. Girimaji, "Assumed beta-PDF model for turbulent mixing : validation and extension to mutiple scalar mixing," *Combust. Sci. Tech.*, vol. 78 (4-6), pp. 177–196, 1991.

[49] T. Poinsot and D. Veynante, *Theoretical and numerical combustion*. Edwards, 2005.

[50] V. Eswaran and S. B. Pope, "Direct numerical simulation of the turbulent mixing of a passive scalar," *Combust. Sci. Tech.*, vol. 31, pp. 506–520, 1988.

[51] N. Swaminathan and S. Mahalingam, "Assessment of conditional moment closure for single and multistep chemistry," *Combust. Sci. Tech.*, vol. 112, pp. 301–326, 1996.

[52] A. E. Sayed, "Ignition delay of non-premixed methane-air mixtures using Conditional Moment Closure (CMC)," Master's thesis, University of Waterloo, Waterloo, Ontario, Canada, 2007.

[53] A. Milford, "Investigation of an inhomogeneous mixing model for conditional moment closure applied to autoignition," Master's thesis, University of Waterloo, Waterloo, Ontario, Canada, 2010.

[54] M. C. Ma, "Investigation of differential diffusion effects in turbulent hydrogen jet flame using conditional moment closure method," Master's thesis, University of Waterloo, Waterloo, Ontario, Canada, 2014.

[55] OpenFOAM, "The open source CFD toolbox." Software available at http://www.openfoam.org.

[56] M. Wang, J. Huang, and W. K. Bushe, "Simulation of a turbulent non-premixed flame using conditional source-term estimation with trajectory generated low-dimensional manifold," *Combust. Theory Model.*, vol. 31, pp. 1701–1709, 2007.

[57] S. J. Brookes and J. B. Moss, "Measurements of soot production and thermal radiation from confined turbulent jet diffusion flames of methane," *Combust. Flame*, vol. 116, pp. 49–61, 1999.

[58] A. Kronenburg, R. W. Bilger, and J. H. Kent, "Modeling soot formation in turbulent methaneair jet diffusion flames," *Combust. Flame*, vol. 121, pp. 24–40, 2000.

[59] R. M. Woolley, M. Fairweather, and Yunardi, "Conditional moment closure modelling of soot formation in turbulent non-premixed methane and propane flames," *Fuel*, vol. 88, pp. 393–407, 2009.

[60] S. J. Brookes and J. B. Moss, "Predictions of soot and thermal radiation properties in confined turbulent jet diffusion flames," *Combust. Flame*, vol. 116, pp. 486–503, 1999.

[61] J. W. Labahn, D. Dovizio, and C. B. Devaud, "Numerical simulation of the Delft-Jet-in-Hot-Coflow (DJHC) flame using conditional source-term estimation," *P. Combust. Inst.*, vol. 35, pp. 3547–3555, 2015.

[62] E. Oldenhof, M. J. Tummers, and E. H. van Veenand D. J. E. M. Roekaerts, "Role of entrainment in the stabilisation of jet-in-hot-coflow flames," *Combust. Flame*, vol. 158, pp. 1553–1563, 2011.

[63] E. Oldenhof, M. J. Tummers, and E. H. van Veenand D. J. E. M. Roekaerts, "ignition kernel formation and lift-off behaviour of jet-in-hot-coflow flames," *Combust. Flame*, vol. 157, pp. 1167–1178, 2010.

[64] J. W. Labahn and C. B. Devaud, "Large eddy simulations (LES) including conditional source-term estimation (CSE) applied to two Delft-Jet-in-Hot-Coflow (DJHC) flames," *Combust. Flame*, vol. 17, pp. 960–982, 2015 Accepted for publication.

[65] C. T. Bowman, D. F. Hanson, D. F. Davidson, W. C. J. Gardiner, V. Lissianski, G. P. Smith, D. M. Golden, M. Frenklach, and M. Goldenberg, "GRI-Mech 2.11," 1995.

[66] G. S. D. M. Golden, M. Frenklach, B. Eiteener, M. Goldenberg, C. T. Bowman, R. K. Hanson, W. C. Gardiner, V. V. Lissianski, and Z. W. Qin, "Gri-mech 3.0," 2000.

[67] "FlameD." http://www.ca.sandia.gov/TNF/DataArch/FlameD.html. Accessed: 2015-10-30.

[68] J. Huang and W. K. Bushe, "Simulation of transient turbulent methane jet ignition and combustion under engine-relevant conditions using conditional source-term estimation with detailed chemistry," *Combust. Theory Model*, vol. 11, pp. 977–1008, 2007.

[69] R. A. Fraser, D. L. Siebers, and C. F. Edwards, "Autoignition of methane and natural gas in a simulated diesel environment," tech. rep., SAE, 1991.

[70] T. I. et al., "Characteristics of spontaneous ignition and combustion in unsteady high-speed gaseous fuel jets," 2003. Paper presented at the 2003 JSAE/SAE International Spring Fuels & Libricants Meeting, Yokohama, Japan, 1922, May. JSAE 20030225/SAE 2003-01-1922.

[71] G. D. Sullivan, J. Huang, T. Wang, W. K. Bushe, and S. Rogak, "Emissions variability in gaseous fuel direct injection compression ignition combustion," 2005. Emissions variability in gaseous fuel direct injection compression ignition combustion. Paper presented at the SAE World Congress, Detroit, MI, 2005; SAE 2005-01-0917. Also in SAE 2005 Transactions. Journal of Engines, pp. 780789, 2006.

[72] B. Jin, R. Grout, and W. K. Bushe, "Conditional source-term estimation as a method for chemical closure in premixed turbulent reacting flow," *Flow Turb. Combust.*, vol. 81, pp. 563–582, 2008.

[73] R. Grout, "An age extended progress variable for conditioning reaction rates," *Phys. Fluids*, vol. 19, pp. 105–107, 2007.

[74] K. N. C. Bray, M. Champion, P. A. Libby, and N. Swaminathan, "Finite rate chemistry and presumed pdf models for premixed turbulent combustion," *Combust. Flame*, vol. 146(7), pp. 665–673, 2006.

[75] M. M. Salehi, W. K. Bushe, and K. J. Daun, "Application of the conditional source-term estimation model for turbulence chemistry interactions in a premixed flame," *Combust. Theory Model.*, vol. 16, pp. 301–320, 2012.

[76] Y. C. Chen, N. Peters, G. A. Schneemann, N. Wruck, U. Renz, and M. S. Mansour, "Finite rate chemistry and presumed pdf models for premixed turbulent combustion," *Combust. Flame*, vol. 107, pp. 223–244, 1996.

[77] D. Dovizio, M. M. Salehi, and C. B. Devaud, "RANS simulation of a turbulent premixed bluff body flame using conditional source-term estimation," *Combust. Theory Model.*, vol. 5, pp. 935–959, 2013.

[78] J. Kariuki, J. Dawson, and E. Mastorakos, "Measurements in turbulent premixed bluff body flames close to blow-off," *Combust. Flame*, vol. 107, pp. 2589–2607, 2012.

[79] N. Shahbazian, M. M. Salehi, C. P. T. Groth, Ö. L. Gülder, and W. K. Bushe, "Performance of conditional source-term estimation model for les of turbulent premixed flames in thin reaction zones regime," *Proc. Combust. Inst.*, vol. 35, pp. 1367–1375, 2015.

[80] P. Domingo, L. Vervisch, S. Payet, and R. Hauguel, "DNS of a premixed turbulent v flame and LES of a ducted flame using a FSD-PDF subgrid scale closure with FPI-tabulated chemistry," *Combust. Flame*, vol. 143, pp. 566–586, 2005.

[81] B. Fiorina, O. Gicquel, L. Vervisch, S. Carpentier, and N. Darabiha, "Approximating the chemical structure of partially premixed and diffusion counterflow flames using FPI flamelet tabulation," *Combust. Flame*, vol. 140, pp. 147–160, 2005.

[82] B. Fiorina, O. Gicquel, L. Vervisch, S. Carpentier, and N. Darabiha, "Premixed turbulent combustion modeling using tabulated detailed chemistry and PDF," *Proc. Combust. Inst.*, vol. 30, pp. 867–874, 2005.

[83] F. T. C. Yuen and Ö. L. Gülder, "Premixed turbulent flame front structure investigation by rayleigh scattering in the thin reaction zone regime," *Proc. Combust. Inst.*, vol. 32, pp. 1747–1754, 2009.

[84] D. Dovizio, J. W. Labahn, and C. B. Devaud, "Doubly Conditional Source-term Estimation (DCSE) applied to a series of lifted turbulent jet flames in cold air," *Combust. Flame*, vol. 162(5), pp. 1976–1986, 2015.

[85] R. W. Schefer and P. J. Goix, "Mechanism of flame stabilization in turbulent, lifted-jet flames," *Combust. Flame*, vol. 112(4), pp. 559–574, 1988.

[86] R. W. Schefer, M. Namazian, and J. Kelly, "Stabilization of lifted turbulent-jet flames," *Combust. Flame*, vol. 99(1), pp. 75–86, 1994.

[87] S. S. Verma, "To study the direct transformation of methane into methanol in the lower temperature range," *Energ. Convers. Manage.*, vol. 43, pp. 1999–2008, 2002.

[88] A. Masri, R. Dibble, and R. Barlow, "The structure of turbulent nonpremixed flames of methanol over a range of mixing rates," *Combust. Flame*, vol. 89, pp. 167–185, 1992.

[89] D. Markus, H. P. Schildberg, W. Wildner, G. Krdzalic, and U. Maas, "Flammability limits of premixed methane/methanol/air flames," *Combust. Sci. and Tech.*, vol. 175, pp. 2095–2112, 2003.

[90] "The university of sydney aerospace, mechanical and mechatronics engineering - database." http://web.aeromech.usyd.edu.au/thermofluids/database.php. Accessed: 2015-8-30.

[91] R. W. Bilger, S. H. Stårner, and R. J. Kee, "On reduced mechanisms for methane-air combustion in nonpremixed flames," *Combust. Flame*, vol. 80, pp. 135–149, 1990.

[92] A. Masri, R. Dibble, and R. Barlow, "The structure of turbulent nonpremixed flames revealed by raman-rayleigh-lif measurements," *Prog. Energy Combust. Sci.*, vol. 22, pp. 307–362, 1996.

[93] M. Roomnia and R. Bilger, "Conditional moment closure modelling of turbulent methanol jet flames," *Combust. Theory Model.*, vol. 3, pp. 689–708, 1999.

[94] J. Y. Chen, "Reduced reaction mechanisms for methanol-air diffusion flames," *Combust. Sci. Technol.*, vol. 78, pp. 127–145, 1991.

[95] R. P. Lindstedt and S. A. Louloudi, "Joint scalar transported probability density function modeling of turbulent methanol jet diffusion flames," *Proc. Combust. Inst.*, vol. 29, pp. 2147–2154, 2002.

[96] M. P. Meyer, *The Application of Detailed and Systematically Reduced Chemistry to Transient Laminar Flames*. PhD thesis, University of London, London, England, 2001.

[97] B. B. Dally, A. R. Masri, R. S. Barlow, and G. J. Fiechtner, "Instantaneous and mean compositional structure of bluff body stabilized nonpremixed flames," *Combust. Flame*, vol. 114, pp. 119–148, 1998.

[98] S. H. Kim, K. Y. Huh, and L. Tao, "Application of the elliptic conditional moment closure model to a two-dimensional nonpremixed methanol bluff-body flame," *Combust. Theory Model.*, vol. 120, pp. 75–90, 2000.

[99] A. Morse. PhD thesis, London University, London, 1977.

[100] N. Peters and B. Rogg, *Reduced chemical mechanisms for application in combustion system*. Springer-Verlag, Heidelberg, 1993.

[101] M. C. Ma and C. B. Devaud, "A conditional moment closure formulation including differential diffusion applied to a non-premixed hydrogen-air flame," *Combust. Flame*, vol. 162, pp. 144–158, 2014.